
A. M. ALHAMAD
PH.D.

This is to certify that the

dissertation entitled

Ultimate Strength of Arch Structures Under
Two- And Three-Dimensional Loading

presented by

Abdulaziz Mahmood AlHamad

has been accepted towards fulfillment
of the requirements for

Ph.D. degree in Civil Engineering

Robert K. Wen

Major professor
Robert K. Wen

Date February 28, 1992

O-12771

ULTIMATE STRENGTH OF ARCH STRUCTURES UNDER TWO- AND THREE-DIMENSIONAL LOADING

By

Abdulaziz Mahmood AlHamad

A DISSERTATION

Submitted to
Michigan State University
in partial fulfillment of the requirements
for the degree of

DOCTOR OF PHILOSOPHY

Department of Civil and Environmental Engineering

1992

ABSTRACT

ULTIMATE STRENGTH OF ARCH STRUCTURES
UNDER TWO- AND THREE-DIMENSIONAL LOADING

By

Abdulaziz Mahmood AlHamad

The ultimate load of parabolic two-hinged and fixed arches under vertical, longitudinal (in-plane horizontal) and lateral (normal to the plane of the arch) loads was studied. Plastic, elastic-nonlinear, and combined (including both plastic and geometric nonlinearities) ultimate loads were obtained under vertical and longitudinal loads (VH-load) and vertical and lateral loads (VS-load). Also, three-dimensional ultimate load surface was considered.

In the developed computer program, nonlinear straight beam finite elements along with a plastic hinge model were used to model the arch behavior. The element plastic resistance is traced through the three possible stages of its end joints being both elastic, one plastic, and both plastic. Of four yield functions implemented, the inverse parabolic function best fitted experimental results. Nonlinear equations were solved using accelerated modified Newton-Raphson method.

For a given ratio of longitudinal to total load, h, and in-plane slenderness ratio, L/r_y, the calculated arch ultimate VH-load, $P_l(h)$, and other responses vary significantly with the type of analysis (i.e., the presumed

nonlinearity) and with the ratio of ultimate loads under longitudinal-only and vertical-only loads, P_{ho}/P_{vo}. The ratio of total to vertical-only plastic ultimate load, $P_{t,p}(h)/P_{vo,p}$, generally decreases with h and L/r_y. For elastic analysis the corresponding ratio, $P_{t,e}(h)/P_{vo,e}$, increases with h for low L/r_y but decreases for higher values. Plastic interaction curves between vertical and longitudinal components of the ultimate load are convex, while elastic ones are concave.

Behavior under combined analysis is similar to plastic analysis for low L/r_y, and to elastic analysis for high L/r_y. For L/r_y = 125 to 325, fixing arch supports increases plastic ultimate load by 0-50%, elastic one by 100-560%, and combined one by 0-120%. Thrust action in the arch decreases and bending increases with h.

Behavior under VH-load is similar to that under vertical unsymmetric load. In particular, the decrease of the "vertical symmetric" component of the arch ultimate with h is similar to its decrease with the unsymmetry ratio.

The ultimate VS-load is insensitive to restraining the in-plane support rotation, but is affected by the type of analysis and it generally decreases with the ratio of lateral to total load and L/r_y. Also, it is influenced by the governing mode of failure (i.e., in-plane or lateral-torsional). This is also true for three-dimensional ultimate load surface.

To My Father, Mahmood, . . .

the Memory of my Mother, Bakriyah, . . .

and to my Family, all of its members:

my wife, Sana,

and my children: Eiman, Osama, Amal, Arwa, and Mahmood.

ACKNOWLEDGEMENTS

I would like to thank professor Robert K. Wen, my thesis advisor, for his intellectual inspiration, encouragement, and patience. The completion of this work is deeply indebted to his support. My thanks are also to members of the guidance committee: Dr. Parvis Soroushian, Dr. Nicholas Altiero, and Dr. David Yen, and to Dr. William Saul, chairman of the Civil and Environmental Engineering Department.

The financial support of King Faisal University, Dammam, Saudi Arabia, for my graduate study is sincerely appreciated. The computing resources provided by the College of Engineering A. H. Case Center for Computer-Aided Engineering and the Center for Academic Computing at Michigan State University are also acknowledged.

My personal appreciation go to three friends: my brother AbdulRazzaq AlHamad, Khaled Al-Hamoudi and Khaled Medallah. Their personal touch was invaluable. And last but not least, the support and endurance of my family here and at home throughout my study is priceless.

TABLE OF CONTENTS

LIST OF TABLES

TABLE PAGE

LIST OF FIGURES

LIST OF SYMBOLS

A	=	Area of the arch or the element cross section.
A_F	=	Amplification factor by which the applied load (live + impact) used in linear analysis is increased to account for nonlinear effects.
B, D	=	Total width and total depth, respectively, of the box-type cross-section of the arch.
c_I, [c]	=	A constant and a 2x2 constant matrix, used in elasto-plastic stiffness matrix calculation when one joint (I) yields, and both joint yield, respectively.
D_i^j	=	Total structure (global) displacement vector at the end of iteration i of nonlinear solution for jth load increment.
D^{LCA}	=	Total structure displacement vector at the end of load-controlled analysis (LCA), to be used in the displacement-controlled analysis procedure.
$D^{',LCA}(\Gamma)$	=	Average value of displacement at d.o.f. Γ, per unit load vector, P^{lv}, at the end of load-controlled analysis (LCA), to be used in the displacement-controlled analysis procedure.
$D^{lv,j}$	=	Displacement vector corresponding to unit load vector, P^{lv}, solved for at the beginning of increment j, for use in the displacement-controlled analysis procedure.
D_o^j	=	Total structure (global) displacement vector at the beginning of load increment j, obtained from the previous increment.

$D_{(1)}$, $D_{(2)}$ = The portions (or subvectors) of displacement vector D that correpond to translation and rotation degrees of freedom, respectively, needed in calculations for convergence tests. D is a generic term that may be replaced by any specific displacement vector, e.g., D^{ref} or dD_i^u.

dD_i^j = Incermental (or iterative) structure displacement vector during iteration i of nonlinear solution for jth load increment.

dD_i^{Iv} = The incremental displacement vector corresponding to the incremental load vector, dP_i^{Iv}, added to the structure displacement vector during iteration i of load increment j of the displacement-controlled analysis procedure so that $dD_i = dD_i^u + dD_i^{Iv}$.

dD_i^u = The incremental displacement vector coeesponding to the unbalanced load vector, dP_i^u, added to the structure displacement vector during iteration i of load increment j of the displacement-controlled analysis procedure so that $dD_i = dD_i^u + dD_i^{Iv}$.

dD_i^{*j} = Incermental structure displacement vector during iteration i of nonlinear solution for jth load increment, obtained using the modified Newton-Raphson method before applying the acceleration procedure.

$dD_{1,c}^j$ = Incremental structure diaplacement vector during the first iteration of solution for jth load increment, recalculated for the purpose of verifying the solution accuracy.

df_i^j = Incremental load parameter obtained during iteration i of load increment j of the displacement-controlled analysis procedure.

dP_i^{Iv} = The incremental external load vector, defined in terms of the unit load vector, P^{Iv}, applied to the structure during iteration i of load increment j of the displacement-controlled analysis procedure.

$dP_i^{u,j}$ = Unbalanced (or residual) structure force vector at the end of iteration i (i.e., at the beginning of iteration i+1) of solution for jth load increment.

$dP_{o,c}^{j}$ = Incremental structure force vector at the beginning of the first iteration of solution for jth load increment, recalculated for the purpose of verifying the solution accuracy.

$dP^{r,j}$ = Residual structure force vector still unbalanced after convergence at the end of solution for jth load increment.

dQ = Force increment vector at the element joints during a load increment.

dQ^{i} = Force increment during a load increment at joint i of the element.

dQ^{s} = Element joint force increment corresponding to stage number s of elasto-plastic resistance computation during a load incrment, s = 1, 2, or 3.

$dQ^{i*,s}$, $Q^{i**,s}$, $Q^{i*p,s}$ = Tentative values of the force increment vector, $dQ^{i,s}$, -at joint i of an element- used during stage s of elasto-plastic resistance calculation to obtain the final value of dQ^{s}.

dq = Total end joint displacement increment vector of the element during a load incrment.

dq^{1} (=dq^{ee}), dq^{2} (=dq^{ep}), and dq^{3} (=dq^{pp}) = Portions of the element displacement increment during a load increment that corresponds to the first, second, and third stages of elasto-plastic resistance, with both joints being elastic, one joint plastic, and both joints plastic, respectively.

dq_{e}^{i}, dq_{p}^{i} = Elastic and plastic components of the total displacement increment at joint i of an element during a load incrment, repectively.

$dq^{i,s}$, $dq_{e}^{i,s}$, $dq_{p}^{i,s}$ = Total displacement at joint i of an elemenet, and its elastic and plastic components, respectively, corresponding to stage s of an element elasto-plastic resistance computation during a load incrment.

dq^s, dq_e^s, dq_p^s = Total element displacement increment vector and its elastic and plastics components corresponding to stage s of the element elasto-plastic resistance computation during a load incrment.

$dq^{u,s}$ = The portion of element displacement increment, dq, that is still not accounted for (i.e. its resistance not calculated) yet at the beginning of stage s of elasto-plastic resistance calculation.

E = Elasticity modulus of the material.

$E_i^{u,j}$, $E_i^{ref,j}$ = The residual and total energy (i.e., work done by the forces through their corresponding displacements) at the end of iteration i of load increment j.

f = Span rise of the arch measured as the vertical distance from the arch support to its crown.

$f_{1,i}$, $f_{2,i}$, $f_{3,i}$, $f_{4,i}$, $f_{5,i}$ = Constants calculated during iteration i for use in the acceleration procedure used in conjunction with the modified Newton-Raphson procedure.

$F_{h,c}(h)$, $F_{h,e}(h)$, $F_{h,p}(h)$ = Combined, elastic, and plastic longitudinal load component of fixed arch under longitudinal and vertical loading, respectively, for a given ratio of h.

F_{ho}, F_{so}, F_{vo} = Ultimate loads that the fixed arch can carry under longitudinal-only, lateral-only, and symmetric vertical-only loads, respectively.

$F_{ho,c}$, $F_{ho,e}$, $F_{ho,p}$ = Combined, elastic, and plastic ultimate loads of fixed arch under longitudinal-only load, respectively.

$F_{s,c}(s)$, $F_{s,e}(s)$, $F_{s,p}(s)$ = Combined, elastic, and plastic lateral load component of fixed arch under lateral and vertical loading, respectively, for a given ratio of s.

$F_{so,c}$, $F_{so,e}$, $F_{so,p}$
= Combined, elastic, and plastic ultimate loads of fixed arch under lateral-only load, respectively.

$F_{t,c}(h)$, $F_{t,e}(h)$, $F_{t,p}(h)$
= Combined, elastic, and plastic total load of fixed arch under longitudinal and vertical loading, respectively, for a given ratio of h.

$F_{t,c}(r)$, $F_{t,e}(r)$, $F_{t,p}(r)$
= Combined, elastic, and plastic total loads of fixed arch under vertical unsymmetric loading, respectively, for a given ratio of r.

$F_{t,c}(s)$, $F_{t,e}(s)$, $F_{t,p}(s)$
= Combined, elastic, and plastic total loads of fixed arch under lateral and vertical loading, respectively, for a given ratio of s.

$F_{v,c}(h)$, $F_{v,e}(h)$, $F_{v,p}(h)$
= Combined, elastic, and plastic vertical load components of fixed arch under longitudinal and vertical loading, respectively, for a given ratio of h.

$F_{v,c}(r)$, $F_{v,e}(r)$, $F_{v,p}(r)$
= Combined, elastic, and plastic symmetric vertical load components of fixed arch under vertical unsymmetric loading, respectively, for a given ratio of r.

$F_{v,c}(s)$, $F_{v,e}(s)$, $F_{v,p}(s)$
= Combined, elastic, and plastic vertical load component of fixed arch under longitudinal and vertical loading, respectively, for a given ratio of s.

$F_{vo,c}$, $F_{vo,e}$, $F_{vo,p}$
= Combined, elastic, and plastic ultimate loads of fixed arch under symmetric vertical-only load, respectively.

f_o = The ultimate load parameter corresponding to the ultimate load of the arch.

H_{cr} = Critical horizontal reaction at arch support.

h, h'	=	Ratio of longitudinal load to total load applied to the arch during vertical and longitudinal loading, and three-dimensional loading, respectively.
I_y, I_z	=	Moments of Inertia of the element cross section about the y-axis and z-axis, respectively.
$I_{y,arch}$, $I_{y,deck}$	=	Moment of inertia of the arch section and the deck section, respectively, of a stiffened arch about their respective local y-axis.
$I_{y,comb}$	=	Combined moment of inertia of a stiffened arch about y-axis.
K	=	A general term that refers to the structure global stiffness matrix.
$K_{eg,o}^{j}$	=	Structure global elastic-gemoetric stiffness matrix at the beginning of increment j, formulated without including plastic effects.
K_o	=	Structure elastic-linear stiffness matrix.
K_t	=	A general term that refers to the structure tangential stiffness matrix.
$K_{t,o}^{j}$, $K_{t,i}^{j}$	=	Structure tangential stiffness matrix at the beginning of increment j, and at the end of iteration i (i.e., at the beginning of iteration i+1) during solution for load increment j.
k_{cr}	=	Coeffecient used in formula for buckling of arch.
k	=	General term for the element stiffness matrix.
k_e	=	Generic term for the elastic stiffness matrix of the element that may be replaced by either the elastic-linear or elastic-nonlinear one.
k_e^{IJ}	=	The submatrix of the elastic stiffness matrix, k_e, that relates the force vector at joint I to the displacement vector at joint J.

$k_e(i,j)$ = The term of elastic stiffness matrix, k_e, that relates ith component of the force vector to jth component of the displacement vector.

$k_{eg,av}$ = Average value of the elastic-nonlinear stiffness matrix of the element during a load increment.

k_{ep} = The elasto-plastic stiffness matrix of an element.

k_g, k_p = The geometric and plastic incremental (also called reduction) matrices of the element elasto-plastic stiffness matrix, k_{ep}, that represent the geometric and plastic effects, respectively.

k_{n1}, k_{n2} = First and second order nonlinear-elastic incremental stiffness matrices of the element, respectively.

k_{eg}, $k_{eg,n}$ = Element elastic-nonlinear (also called elastic-geometric) stiffness matrix.

k_o = Element elastic-linear stiffness matrix.

k_t = Element tangential stiffness matrix (that may include either or both geometric and plastic nonlinearity effects, whichever is present).

k_t^s = Elemenet tangential stiffness matrix at beginning of stage s of elasto-plastic resistance calculation.

L' = Length of the arch measured along its axis.

L = General term that refers to arch or element length: length of the horizontal projection of the arch, or the finite element or frame span length.

L/r_y = In-plane slenderness ratio of the arch.

L/r_z = Out-of-plane slenderness ratio of the arch.

N = A general term for axial force in a structural member.

$\{N, V_x, V_y, M_x, M_y, M_z\}$ = Force vector at a joint of the element.

N_{QP}, $N_{QP,e}$ = The axial force and critical (buckling) axial force, respectively, at the quarter point of the arch span due to applied load.

N_p, $M_{y,p}$, $M_{z,p}$ = Plastic (also called ultimate or limit) forces at a joint of the element.

$P^j(D)$ = The load applied to the structure, expressed in its general form as a function of the structure displaced position, D.

P^{lv} = Unit load vector applied to the structure. The actual load, P, applied to the structure is measured in terms of P^{lv} and a load parameter so that, $\Delta P = \Delta f \cdot P^{lv}$.

$P_{(1)}$, $P_{(2)}$ = The portions (or subvectors) of force vector P that correpond to translation and rotation degrees of freedom, respectively, needed in calculations for convergence tests. P is a generic term that may be replaced by any specific force vector, e.g., P^{ref} or dP_i^u.

P_o^j = Total load vector applied to the structure at the end of increment j (i.e., at the beginning of increment j+1).

$P_{h,c}(h)$, $P_{h,c}(h)$, $P_{h,p}(h)$ = Combined, elastic, and plastic longitudinal load components of two-hinged arch under longitudinal and vertical loading, respectively, for a given ratio of h.

P_{ho}, P_{so}, P_{vo} = Ultimate loads that the two-hinged arch can carry under longitudinal-only, lateral-only, and vertical-only (symmetric) loads, respectively.

$P_{ho,c}$, $P_{ho,e}$, $P_{ho,p}$ = Combined, elastic, and plastic ultimate loads of two-hinged arch under longitudinal-only load, respectively.

P_{hu}, P_{su}, P_{vu} = Longitudinal, lateral, and vertical (symmetric) unit total loads, respectively, applied to the arch due to a unit uniformly distributed load along the horizontal projection of the arch in the corresponding direction.

$P_{s,c}(s)$, $P_{s,e}(s)$, $P_{s,p}(s)$
= Combined, elastic, and plastic lateral load component of two-hinged arch under lateral and vertical loading, respectively, for a given ratio of s.

$P_{so,c}$, $P_{so,e}$, $P_{so,p}$
= Combined, elastic, and plastic ultimate loads of two-hinged arch under lateral-only load, respectively.

$P_{t,c}(h)$, $P_{t,e}(h)$, $P_{t,p}(h)$
= Combined, elastic, and plastic total loads of two-hinged arch under longitudinal and vertical loading, respectively, for a given ratio of s.

$P_{t,c}(r)$, $P_{t,e}(r)$, $P_{t,p}(r)$
= Combined, elastic, and plastic total loads of two-hinged arch under vertical unsymmetric loading, respectively, for a given ratio of r.

$P_{t,c}(s)$, $P_{t,e}(s)$, $P_{t,p}(s)$
= Combined, elastic, and plastic total load of two-hinged arch under lateral and vertical loading, respectively, for a given ratio of s.

$P_{tu}(h)$, $P_{tu}(s)$ = Unit total loads applied to the arch as a combination of vertical and longitudinal, and vertical and lateral loads, respectively.

$P_{v,c}(h)$, $P_{v,e}(h)$, $P_{v,p}(h)$
= Combined, elastic, and plastic vertical load component of two-hinged arch under longitudinal and vertical loading, respectively, for a given ratio of h.

$P_{v,c}(r)$, $P_{v,e}(r)$, $P_{v,p}(r)$
= Combined, elastic, and plastic symmetric vertical load components of two-hinged arch under vertical unsymmetric loading, respectively, for a given ratio of r.

$P_{v,c}(s)$, $P_{v,e}(s)$, $P_{v,p}(s)$
= Combined, elastic, and plastic vertical load component of two-hinged arch under lateral and vertical loading, respectively, for a given ratio of s.

$P_{vo,c}$, $P_{vo,c}$, $P_{vo,p}$ = Combined, elastic, and plastic ultimate loads of two-hinged arch under symmetric vertical-only load, respectively.

p_{DL} = Symmetric (dead) load intensity applied to the arch full span along its horizontal projection.

p_{bu}, p_{su}, p_{vu} = Longitudinal, lateral, and vertical (symmetric) unit uniformly distributed loads applied to the arch along the horizontal projection of the arch in the corresponding direction.

p_{LL} = Unsymmetric (live) load intensity applied to half of the arch span along its horizontal projection.

p_o = Ultimate load intensity (or uniformly distributed load) applied along the arch horizontal projection that causes failure, calculated using elastic stability or nonlinear analysis.

p_p = The load intensity (or uniformly distributed load) applied along the arch horizontal projection that causes yielding in the arch at its supports, calculated using linear analysis.

p_t = Total load intensity of the different load intensities (e.g., live, dead, and longotudinal) applied to the arch half of full length span of its horizontal projection.

Q = Element force vector at its joints.

Q^i = The force vector at the joint i of an element.

Q_o^s, Q_n^s = Old and new (calculated) force vectors (or points) at the beginning and end of stage s of elasto-plastic resistance calculation.

$Q_n^{*,s}$, $Q_n^{**,s}$, $Q_n^{*p,s}$ = Tentative values of the new force vector, Q_n^s, used during stage s of elasto-plastic resistance calculation to obtain the final value of Q_n^s.

Q_p^i = The plastic (ultimate) force of the ith component of the force vector at an element joint.

q	=	General term for the element end (or joint) displacement vector.
q_e, q_p	=	Elastic and plastic components of element joint displacement vector, dq.
q^j, q_e^j, q_p^j	=	The total, elastic, and plastic displacement vector at joint j of an element.
q_o, q_{mp}, q_n	=	The old, mid-point, and new joint displacement vector of the element at the beginning, mid-point, and end of a load increment, respectively.
$R(D)$	=	Structure resistance vector corresponding to the structure displaced position, D.
R_o^j	=	Structure resistance at the beginning of increment j.
r	=	Ratio of symmetrical (e.g., dead) load intensity to the total (symmetrical and unsymmetrical, e.g., dead and live) load intensity applied to the arch.
r_{eq}	=	Equivalent unsymmetry ratio when applying both vertical unsymmetrical and longitudinal loads to the arch along with vertical symmetrical load.
r_y, r_z	=	Radius of gyration of the arch section about the y-axis and z-axis, respectively.
S1 and S2	=	symbols (or names) for the two section proportions of the arch that were used in the parametric study.
s, s'	=	Ratio of lateral load to total load applied to the arch during vertical and lateral loading, and three-dimensional loading, respectively.
sf_m	=	scaling factor applied to the specified load parameter, Δf_o, to obtain a smaller load increment in the procedure for adjusting the load increment size.
t_f, t_w	=	Flange and web thicknesses, respectively, of the box-type cross-section of the arch.

U = Total strain energy in the element produced by internal forces.

U_1, U_2, U_3 = Portions of the element total strain energy, U, corresponding to the quadratic, cubic, and quartic terms of U.

V = Gradient vector of the element, $= \begin{Bmatrix} \{v^1\} & \{0\} \\ \{0\} & \{v^2\} \end{Bmatrix}$

$V^i(Q^i)$ = Gradient vector of the force vector, Q^i, at joint i of an element.

V_o^i, V_n^i = Gradient vectors calculated at the beginning and end of a displacement stage at joint i during the process of elasto-plastic resistance calcultion of an element.

$V^{i(j)}$ = Estimated gradient vector at joint i of an element during iteration j of the iteration process to return the force point to the yield surface.

v, v' = Ratio of vertical load to total load applied to the arch during vertical and longitudinal or vertical and lateral loading, and three-dimensional loading, respectively.

α_{cr} = Coeffecient used in formula for buckling of arch.

α_e^i = Scaling factor that scales the force increment vector, dQ^i, at joint i of an element to the yield surface during a load increment.

$\alpha_e^{i,s}$ = Scaling factor that scales the force increment vector, $dQ^{i,s}$, at joint i of an element to the yield surface during stage s of elasto-plastic resistance computation of a load increment.

β, γ = Constants in formulas for arch ultimate load.

ΔD_i^j = Total displacement increment during increment j, accumulated through the end of iteration i for nonlinear solution.

$\Delta D_{sp}(\Gamma)$ = Specified value of the displacement at the controlling d.o.f., Γ, used in the displacement-controlled analysis procedure.

Δf = Load parameter increment that defines the applied load for the increment in terms of the unit load vector, $\Delta P = \Delta f \cdot P^{iv}$.

Δf_i^j = Total increment load parameter at the end of iteration i of load increment j that define the applied external load for the increment in the displacement-controlled analysis procedure, $\Delta f_i = \Delta f_{i-1} + df_{i-1}$.

Δf_o = The initial value of the load parameter increment, Δf, specified in the data input.

Δf_{sp} = Specified load parameter value used in determining the value of displacement at the specified d.o.f., $\Delta D_{sp}(\Gamma)$ in the displacement-controlled analysis procedure.

Δf_{total} = Total magnitude of the load parameter to be applied to the structure using the specified load vector.

ΔL = Length of the horizontal projection of each arch segment represented by a straight beam finite element, = L/n, where n = number of elements.

ΔP_{hu}, ΔP_{su}, ΔP_{vu} = Unit longitudinal, lateral, and vertical concentrated loads that represent the uniformly distributed load applied to an arch node, in their respective directions.

ΔP^j = Load increment applied to the structure during load increment j.

ΔR_i^j = Structure incremental resistance during increment j, calculated at the end of iteration i.

δP_i^u = The difference between the unbalanced load vectors at the beginning of iterations i-1 and i, $\delta P_i^u = dP_i^u - dP_{i-1}$, used in the acceleration procedure used in conjunction with the modified Newton-Raphson method.

Γ	=	The d.o.f. that is specified to be used as the controlling d.o.f. in the displacement-controlled analysis procedure.
$\epsilon(x,y,z)$	=	Normal strain at point (x,y,z) of the element.
ϵ_Φ	=	Tolerance limit for yield surface definition of a force function at an element's joint.
$\epsilon_P, \epsilon_D, \epsilon_E$	=	Tolerance limits for force, displacement, and energy convergence tests, respectively.
Φ	=	Force function (or plastic potential function) of the force vector at an element's joint.
Φ_{ll}, Φ_{ul}	=	Lower and upper limits of the yield surface definition.
$\Phi^i(Q^i)$	=	Force function of force vector Q^i at joint i of an element.
Φ_o^i, Φ_n^i	=	Force functions of force vectors Q_o^i and Q_n^i, at the beginning and end of load (or a displacement stage) increment, respectively, at joint i of an element.
ϕ_i, θ_i, ψ_i	=	Rotation displacements about x-, y-, and z-axes at joint i of an element.
λ_i	=	Proportionality constant that relates the plastic displacement vector to the gradient vector at the yielded joint i of an element.
μ_i, ν_i, ω_i	=	Translational displacements in the direction of x-, y-, and z-zxis, respectively, at joint i of an element.
$\sigma(y,z)$	=	Normal stress at point (y,z) of the element section.
σ_o	=	Allowable (or ultimate) stress permitted to occur in the arch due to applied loads.
σ_y	=	Yield stress of the material.
σ_n, σ_m	=	Normal stress at a section due to normal force and bending moment, respectively.

$\tau_{1,E}$, $\tau_{2,E}$ = Limits for energy terms divergence tests used for check of iteration process divergence during nonlinear solution for a load increment.

$\tau_{1,P}$, $\tau_{2,P}$ = Limits for force norms divergence tests used for check of iteration process divergence during nonlinear solution for a load increment.

CHAPTER I

INTRODUCTION

1.1 GENERAL

The objective of this thesis is to study the ultimate load carrying capacity of arches. The prevailing trend in structural engineering is toward the ultimate strength design, mainly because it is based on a more rational approach to the design process that would place the structural material where it is needed. In addition, it helps to provide accurate estimation of the structure reliability under different loading conditions as exemplified by the recently adopted load-resistance factor design (LRFD) method. In this regard, this study represents a continuation of the efforts to study the ultimate strength of structures under different load combinations.

The main advantage of arch structures is their ability to carry loads through axial thrust (with little or no bending moments) when the funicular curve of the applied load is close to or coincides with the longitudinal axis of the arch. For parabolic arches, this load is the symmetrical uniform in-plane load applied to the horizontal projection of the arch. While this property allows the construction of long-span bridges with relatively small section depth to

carry dead loads, the disadvantage of possible sudden failure due to buckling under high axial load requires consideration its of stability.

In addition, when the arch is subjected to loads other than the vertical symmetrical load -for example, vertical unsymmetrical load- its load carrying capacity is significantly reduced. In this study, the effects of other types of loading is considered, in particular the combination of vertical load with longitudinal (horizontal in-plane) and lateral (transverse) loads are considered. These loads usually occur due to earthquake or wind effects.

1.2 OVERVIEW

1.2.1 Arch Behavior under Different Loads

In general, the behavior of arch structures under different combinations of loading conditions and the interaction between possible different components of the structure itself (for example, the arch ribs, the deck, and different bracing systems) is quite complicated. Simplifying assumptions that eliminate some of these variables -such as neglecting possible deck and/or bracing systems- are usually deemed necessary to first study the behavior of the main structural member, i.e., the arch.

The nonlinear behavior of arches under vertical in-plane loading was extensively studied where both elastic and plastic nonlinearities were included. It is well documented (for example Austin (2), and Kuranishi (16)) that the arch total ultimate load decreases as the vertical load unsymmetry increases, and

that unsymmetric failure mode governs for both the symmetric and unsymmetric loads. This was found to be true also for stiffened arches where the deck serves as a stiffener to the arch in bending.

Another mode of failure that was investigated in the literature is the out-of-plane elastic behavior of arches, specially the lateral-torsional failure of arches under vertical loading, where it was found that a single-rib arch often prematurely fails in this mode before it reaches its in-plane ultimate strength. To overcome this problem, enough lateral stiffness may be provided by using double-rib arches connected with lateral bracing system. Inelastic behavior of braced double-arch systems was studied under wind loading, where the lateral load was assumed to be a small proportion of the vertical load, and the bracing requirements were the main objective.

The arch may be subjected to three types of loading. First, a vertical in-plane loading due to dead and live loads is the primary type of loading. Longitudinal (horizontal in-plane) loading may result from wind load or more likely from earthquake load. Lateral (transverse) loading also usually results from wind or earthquake.

While the in-plane and out-of-plane arch behavior had been extensively studied under different combinations of vertical and lateral loads, the interaction between the vertical and longitudinal loads had not been investigated probably bacause of the assumption that the arch elastic stiffness is much higher in the longitudinal direction. However, this assumption may not be true

when material nonlinearity is included. This is considered in this study. In addition, limited studies in the past on the interaction between symmetric and unsymmetric vertical and lateral loads were limited to two-dimensional studies. In this study, a case involving the three loads is considered.

1.2.2 Plasticity Model

Early studies of arch behavior concentrated on elastic buckling of arches and neglected plastic effects. Recent studies included both elastic and plastic nonlinearities mainly using a "fiber model" to represent the arch. In this model, the arch is divided into multiple segments along its longitudinal axis with each segment being divided into small fibers that extend along the segment length (i.e., the cross section of each segment is divided into small areas). The stresses and strains in each one of these fibers are assumed to be uniform throughout the fiber. By assuming a nonlinear stress-strain relation (e.g., elasto-plastic relation) for each fiber of the segment and assuming that "plane sections" remain plane after deformation, the compatibility and equilibrium conditions at the interfaces of each two adjoining segments are enforced. As a result, the forces and stresses in the arch can be solved as a set of nonlinear equations, and the spread of yielding in the arch may be traced with the progress of loading.

Although the fiber model was successful and produced accurate results, its use for complicated structures is cumbersome and may be prohibitively time consuming. In this research, the classic plastic hinge approach was used to

model plastic effects with special treatment of discontinuities of the yield surface. Comparison with experimental results produced good agreement, and this model was used in obtaining the data for the parametric studies.

1.3 SUMMARY OF PRESENT STUDY

In chapter two, a detailed, three-stage procedure to implement the plastic hinge model is described. Four different functions, namely spherical, octahederal, parabolic, and inverse parabolic, were used to model the yield surface at a plastic hinge. The gradient singularity at regions of discontinuity in the yield surface was treated by using special patch functions. In chapter three, the scope and implementation aspects of the computer program for nonlinear solution are described, and numerical results are presented for comparison with experimental and theoretical solutions reported in the literature. The inverse parabolic function was shown to produce the best agreement.

In chapter four, the elastic, plastic, and combined (that includes both nonlinearities) ultimate loads of single-rib parabolic arch with different support conditions, under different combinations of symmetrical vertical load and longitudinal load (uniformly distributed along the arch horizontal projection) are studied. Comparison with the arch behavior under unsymmetrical vertical loading revealed similarity between the two cases, specially for the combined analysis. In addition, the interaction between the vertical and horizontal load components, the failure modes and response curves, the formation of plastic hinges and the force path at the arch quarter point were also examined.

In chapter five, the arch plastic, elastic and combined ultimate loads under different combinations of vertical load and lateral load (also uniformly distributed along the arch horizontal projection) were obtained, and the interaction curves, failure modes, and response curves were also examined. In addition, the three-dimensional combined ultimate load surface of the arch was constructed to demonstrate the interaction between the three types of loading.

1.4 LITERATURE REVIEW

Literature review of the in-plane and out-of-plane behavior of arches is presented in the following sections. For each section, the review is divided into studies that deal with elastic behavior and those that include plastic effects.

1.4.1 In-Plane Behavior of Arches

A) Elastic Behavior

In 1971, Austin (2), summarized the research done in the area of arch behavior to that date. He reviewed the studies of linear buckling of arches under symmetrical loading. These studies proposed a formula for calculating the arch strength in terms of the axial thrust at the quarter point of the arch span, N_{QP}, that is analogous to the formula for buckling load of axially loaded column,

$$N_{QP,e} = 4\alpha_{cr}\, EI_y/L'^2 = 4\pi^2\, EI_y/(k_{cr}L')^2$$

where $N_{QP,e}$ is the critical axial load at the span quarter point that causes the arch to buckle, α_{cr} and k_{cr} are coefficients that depend on rise-to-span ratio,

f/L, and type of arch support (2-hinged, 3-hinged, or fixed), L' is the arch length along its longitudinal axis, L is the arch span length (the horizontal projection of L'), I_y is the moment of inertia about the out-of-plane axis, and E is the elasticity modulus. The arch critical load under unsymmetrical vertical loading was reviewed, where the studies suggested an amplification factors, A_F, similar to that of beam-column to correct linear moments and deflections for nonlinear effects, $A_F = 1/(1-N_{QP}/N_{QP,e})$, where N_{QP} is the actual thrust resulting from the applied load. However, when the ratio of $N_{QP}/N_{QP,e}$ is high, the author recommended a deflection (i.e., nonlinear) analysis.

Studies suggested the above formulas may be applied to non-uniform arches using an equivalent arch with properties equal to the average properties of the actual arch, and to stiffened arches by using an equivalent moment of inertia, $I_{y,eq} = I_{y,arch} + I_{y,deck}$.

In 1976, Austin and Ross (3), studied the symmetrical and unsymmetrical buckling modes of symmetrically loaded arches, using both classical (linear eigenvalue) and nonlinear analysis. They found that the unsymmetrical buckling load was always lower than symmetrical buckling load for both two-hinged and fixed arches, and that the classical theory produces large errors in predicting buckling loads for symmetrical modes, and in predicting moments for all modes. They also found that a parabolic arch carries larger load than circular or catenary arches.

In 1980, Maeda and Hayashi (24), reported on the elastic nonlinear nalysis and design aspects of long span arches and compared the obtained esults with the limits specified by the Japanese specifications. Based on their bservations they suggested more precise formulas that take the load nsymmetry into account.

In 1982, Harrison (12), reported a study of the elastic response of arabolic arches under unsymmetrical loading that extends from one edge to a raction of the length (varied from 0.3 to 1.0). He concluded that the ultimate oad intensity (i.e., uniformly distributed load) was minimum when about 70% f the span was loaded, with reduction of 10% for 2-hinged arches and 13% for ixed arches compared with symmetric loading.

In 1984, Medallah (25), reported on the nonlinear response of deck-tiffened arch subjected to constant vertical load and loaded till failure by ongitudinal loading. He found the amplification factor method mentioned bove adequate to predict the elastic nonlinear response from linear analysis.

In 1989, Dusseau and Wen (11), reported the results of linear dynamic nalysis of deck-stiffened arches under unequal seismic support earthquake otion in vertical, longitudinal and lateral directions. The study found that ngitudinal motion creates high stresses in the arch itself and in the longitudi-l bracing system between the arch and deck; they found that the sum of resses due to both vertical and longitudinal motions could exceed the yield ress of the material under a credible earthquake.

3) Plastic Behavior

The behavior of arches when both geometric and plastic nonlinearities are included was a subject of study since 1972. In the majority of these studies, the fiber approach described earlier was used. A survey paper by Yabuki and Vinnakota (46), 1984, covers different aspects of research on arch behavior up to that date.

In 1972, Kuranishi and Lu (16), reported a study of the ultimate load of 2-hinged steel arches under vertical loading. Using rectangular and sandwich sections, they studied the variation of the ultimate load ratio, p_o/p_p (defined as the ratio of the computed ultimate load intensity, p_o, to that which first causes yield in the arch using linear analysis, p_p), with main parameters such as in-plane slenderness ratio L/r_y, unsymmetry ratio, r ($= p_{DL}/(p_{DL}+p_{LL})$, where p_{DL} is the dead load applied over the full arch span, and p_{LL} is the live load applied over half the arch span), and span-to-depth ratio, f/L (see Figures (4-1) and (4-2)). They found that p_o/p_p decreases with the increase of r and L/r_y. In addition, p_o/p_p becomes significantly less than one as r increases, which indicates that unsafe design would result from using the linear elastic analysis.

In 1973 and based on the above study, Kuranishi (17), proposed two formulas for conventional structural design based on elastic linear and nonlinear analysis, that are based essentially on the sum of stresses due to bending and axial loads.

Shinke, Zui, and Namita (35), 1975, studied arches under symmetrical and unsymmetrical vertical loads, and the relation of p_o/p_p with other main parameters, and arrived at conclusions similar to Kuranishi and Lu. In another study (36), 1977, they compared analytical results with experimental results, and found good agreement.

Kuranishi (18), 1977, studied the ultimate load of fixed arches and found that their behavior is similar to that of two-hinged arches with same properties but they have larger load carrying capacity. Also, he noted that for stiff arches with low slenderness ratio), as the force path (i.e. the axial force-bending moment relation) at the arch span quarter point approaches the yield surface, it takes a path parallel to the yield surface with direction toward the axial force axis so that the axial force increases while the bending moment decreases; for slender arches, the force path moves toward the moment axis.

Komatsu and Shinke (14), 1977, proposed a design formula for the in-plane instability criteria of a symmetrically loaded arch analogous to the beam-column formula used in current specifications, where the ratio of allowable stress, σ_o, to yield stress, σ_y, is related to the slenderness ratio of the arch. In this formula two relationships in two distinct regions were defined, one controlled by plastic behavior and the other by elastic behavior. In addition, they extended this formula for the case of unsymmetrical loading by introducing a correction factor for the above formula.

Kuranishi and Yabuki (19), 1979, compared an analytical method to experimental data and found good agreement. They also found that residual stresses may reduce the ultimate load of the arch by up to 20%, while section proportioning has much smaller effect (up to $\pm 5\%$). To avoid plastic local buckling of the arch section components, they suggested that maximum strain at the arch springing should not exceed 4 times the yield strain.

In 1984, the same authors proposed a design formula based on research of plastic behavior of two-hinged arches (22), and in 1987 they (along with Lu) extended it to fixed arches (48). The formula uses two regions based on the level of axial load at the quarter point of the arch, similar to the suggestion of Austin (2), and correlates axial load and bending moment obtained using linear analysis.

Yabuki, Vinnakota, and Kuranishi (47), 1986, reported a study of the behavior of fixed arches. They found that the elastic theories (linear and nonlinear) overestimate the ultimate load of the arch.

.4.2 Out-of-Plane Behavior of Arches

The out-of-plane behavior of arches under vertical loading, or lateral-torsional buckling, was extensively studied. However, arch behavior under large lateral loading received less attention. Studies on elastic and elasto-plastic arch behavior are reviewed here.

A) Elastic Behavior

In 1968, I. Ojalvo and Newman, (26), described a theoretical formulation of the linear elastic stability of curved twisted members that was used in several studies of arch behavior, (27,38,39,40). M. Ojalvo, Demuts, and Tokarz (27), 1969, studied the linear elastic stability of circular ring segments under thrust or pull force applied to the ring chord (the line that connects the two ends of the ring). They found that torsional rigidity has a slight effect on thrust buckling, but it has a more pronounced effect on pull buckling.

Shukla and Ojalvo (38), 1971, studied the elastic stability of parabolic arches under vertical and tilting loads. Tokarz (39), 1971, reported on experimental tests of lateral-torsional buckling of circular and parabolic arches with different crown and end support conditions under vertical and tilted loads. In 1972, Tokarz and Sandhu, (40), presented an analytical study of the elastic buckling of parabolic arches to predict the obtained experimental results above, and found fair to good agreement.

These studies found that the load direction profoundly affected the arch buckling load. It is highest when the load tilts with the arch (called hanger-type load) and lowest when the load tilts opposite to it (called column-type load), with vertical load (with no tilting) in between. The differences between highest and lowest loads reach up to 400%. Also, the studied arches were found to fail in symmetric out-of-plane mode due to bending, with insignificant influence of

the ratio of torsional rigidity to lateral bending rigidity on the buckling load for small rise-to-span ratio ($f/L \leq 0.3$).

Sakimoto and Namita (31), 1971, studied the out-of-plane elastic buckling of double-rib arches with bar transverse bracing under radial in-plane loads, and found good agreement with experimental verification. Yabuki and Kuranishi (44), 1973, studied the effect of warping on the elastic buckling of double-rib circular arches under lateral loading, and found that the effect of warping on the arch behavior increases as torsional rigidity and slenderness ratio increase.

B) Plastic Behavior

Using the fiber model and incremental nonlinear analysis, Komatsu and Sakimoto (15), 1977, studied the elasto-plastic lateral-torsional ultimate load of two-hinged single parabolic arches under vertical and hanger-tilted loads. When plastic effects were included, they found the hanger-type ultimate load to be 100% larger than that of vertical load. This is relatively small when compared with elastic analysis, where the difference is 200%. They also found that f/L ratio does not affect the ultimate load.

Sakimoto and Komatsu (32), 1979, studied the effect of truss-type transverse bracing on the ultimate load of double-rib arches under combination of vertical and lateral loading. They found the system fails due to bracing buckling for slender arches ($L/r_y > 180$), while the ribs failure controls for stiff arches; a simple formula to predict the arch ultimate strength based on

linear analysis was suggested. Another study by the same authors (33), 1982, on the behavior of parabolic double-rib arches with different bracing systems under vertical loading found that failure is dominated by lateral bending mode rather than torsional one in both deformation and moments.

Based on the above studies, Sakimoto and Komatsu (34), 1983, proposed a formula to predict the arch ultimate strength due to lateral instability, similar to that of beam-column formula, that takes into consideration the type of end support (two-hinged or fixed), lateral rigidity, and extent of bracing along the arch length.

Kuranishi and Yabuki (21), 1981, studied the ultimate load of double-rib parabolic arches with lateral bracing under vertical and lateral loading, and found the in-plane ultimate load begins to decrease significantly when the applied lateral load exceeds 50% of the actual ultimate lateral load -calculated from nonlinear elasto-plastic analysis-. Under "practical" lateral load due to wind loading -defined below-, they found the in-plane load carrying capacity decreases slightly (less than 10%) and exhibits in-plane failure mode when sufficient lateral stiffness is provided; the "practical" wind load was assumed to be 10% of the arch ultimate lateral load calculated from simple plastic analysis (using linear analysis).

Extension of this study by Yabuki, Vinnakota, and Kuranishi (45), 1983, found the in-plane vertical load in presence of practical lateral load decreases with the increase of in-plane slenderness ratio, L/r_y, and rise-to-span ratio, f/L;

the decrease reaches a maximum of 15% for $L/r_y = 300$ and $f/L = 0.3$. Design criteria to account for the effect of lateral load on the in-plane ultimate load and to specify the required out-of-plane stiffness to prevent lateral failure mode were suggested by Kuranishi and Yabuki (23), 1984.

CHAPTER II

THEORETICAL MODELS FOR NONLINEAR ELEMENTS

2.1 INTRODUCTION

The nonlinear finite element program prepared for this study uses straight beam elements to model the arch. Both geometric and material nonlinearity effects were incorporated into the finite element model, where either or both nonlinearities may be included in the analysis.

The tangential stiffness matrix of the straight beam element consists of the elastic linear stiffness matrix plus the contribution of the geometric (elastic-nonlinear) and plastic nonlinearities in the form of incremental matrices (30,28). For elastic-nonlinear analysis and simple-plastic analysis only the corresponding incremental matrix is included. For combined nonlinear analysis where both geometric and plastic effects are present both incremental matrices are included.

The details of formulation of the element stiffness matrices and calculation of its resistance for different cases of nonlinearity are detailed in the

following sections. The computer implementation of the nonlinear solution procedure of the structure equilibrium is presented in the next chapter.

2.2 ELASTIC-NONLINEAR RESISTANCE OF STRAIGHT BEAM ELEMENT

For elastic-nonlinear analysis, the structure resistance during a load increment is assumed to be linear, and is evaluated as the average of resistance during that increment,

$$\Delta Q = k_{eg,av} \Delta q, \tag{2.1}$$

where ΔQ is the element incremental resistance (i.e., force) during the load increment, $k_{eg,av}$ is its "average" elastic-geometric stiffness matrix that represents the element stiffness during the increment, and Δq is its incremental displacement vector at its end joints, obtained from the structure global displacement vector (through transformation from the structure global axes to the element local axes).

In the following two sections, the model used to calculate the element stiffness matrix is presented first, and then the procedure to evaluate the average stiffness matrix during a load increment is considered next.

2.2.1 Element Elastic-Geometric Stiffness Matrix

The model for elastic-geometric stiffness matrix used here is that developed by Wen and Rahimzadeh (42), and derived using Lagrange coordinates for small rotations (abbreviated as Lagrange-SR), where the global coordinates are fixed (not updated) and the rotation of the element chord is

small (less than 15 degrees). It is based on the "average axial strain" model, where the contribution of the transverse displacement to normal strain, $\epsilon(x,y,z)$, (the second term in the equation below) is averaged over the element length,

$$\epsilon(x,y,z) = \frac{d\mu}{dx} + \frac{1}{L}\int_0^L \frac{1}{2}\left[\left(\frac{dv}{dx}\right)^2 + \left(\frac{d\omega}{dx}\right)^2\right] dx + y\frac{d^2v}{dx^2} + z\frac{d^2\omega}{dx^2},$$

and the interpolation functions are linear for longitudinal and torsional displacements and cubic for lateral ones,

$$\mu = \mu_1 + (\mu_2 - \mu_1)\,x/L,$$
$$\phi = \phi_1 + (\phi_2 - \phi_1)\,x/L,$$
$$v = v_1 + \theta_1 x + (-2\theta_1 - \theta_2 + 3\theta_o)\,x^2/L + (\theta_1 + \theta_2 - 2\theta_o)\,x^3/L^2,$$
$$\omega = \omega_1 - \psi_1 x + (2\psi_1 + \psi_2 - 3\psi_o)\,x^2/L + (-\psi_1 - \psi_2 + 2\psi_o)\,x^3/L^2.$$

In these equations, $\{\mu_1, v_1, \omega_1, \phi_1, \theta_1, \psi_1, \mu_2, \ldots, \psi_2\}$ are the element joint displacement vector, q, Figure (2-1), $\theta_o = (v_2 - v_1)/L$ and $\psi_o = (\omega_1 - \omega_2)/L$ are the chord rotations, and L is the element original length. The x-axis is the local longitudinal axis of the straight beam element while y- and z-axes are the principal axes of its section. The normal strain expression is used to compute the element strain energy, U, over its volume, dV,

$$U = \int_{\text{volume}} \frac{1}{2} E \epsilon^2 dV$$
$$= U_2 + U_3 + U_4$$

where E is the elasticity modulus and U_2, U_3, and U_4 are the quadratic, cubic and quartic terms of strain energy, U, respectively. The elements of the tangent stiffness matrix are derived from the energy expression,

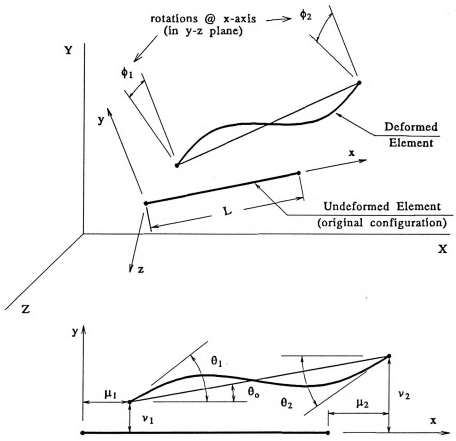

Element projection on local x-y plane

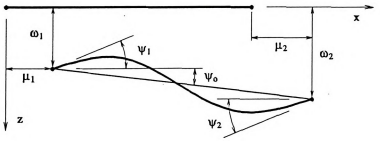

Element projection on local x-z plane

Figure 2-1 End joint displacements of straight beam element in three dimensional space.

$$k_e(i,j) = \frac{\partial^2 U}{\partial q_i \partial q_j}$$
$$= \frac{\partial^2 U_2}{\partial q_i \partial q_j} + \frac{\partial^2 U_3}{\partial q_i \partial q_j} + \frac{\partial^2 U_4}{\partial q_i \partial q_j}$$
$$= k_o(i,j) + k_{n1}(i,j) + k_{n2}(i,j).$$

The resulting elastic-geometric stiffness matrix is composed of three matrices,

$$[k_{eg}] = [k_o] + [k_{n1}] + [k_{n2}], \qquad (2.2)$$

where k_o is the linear elastic stiffness matrix, and k_{n1} and k_{n2} are the first order and second order incremental stiffness matrices. The last two matrices constitute the incremental geometric matrix,

$$[k_g] = [k_{n1}] + [k_{n2}] \qquad (2.3)$$

The detailed derivation and stiffness matrix elaments can be found in reference (42).

2.2.2 Calculation of Element Elastic Resistance

The element elastic-geometric stiffness matrix at a given displaced position is evaluated as a function of its elastic linear stiffness matrix, k_o, and its joint displacement vector at that position, q,

$$k_{eg} = f(k_o, q). \qquad (2.4)$$

The element new displacement vector at the end of a load increment, q_n, may be determined, $q_n = q_o + \Delta q$, where q_o is the displacement vector at the beginning of the increment. Also, the increment mid-point displacement can be

found, $q_{mp} = q_o + \Delta q/2$. The element average stiffness matrix during the increment may be evaluated at the midpoint displacement position of the increment,

$$k_{eg,av} = f(k_o, q_{mp}),$$

or alternatively may be taken as the average of the stiffness matrices evaluated at beginning of the increment, $k_{eg,o}$, and at the end of the increment, $k_{eg,n}$,

$$k_{eg,av} = \frac{1}{2}(k_{eg,o} + k_{eg,n}).$$

The obtained numerical results show that both methods give very similar results, but the first method is less calculation intensive and is the one used here.

When plastic effects are present, only the elastic component of the element total displacement vector contributes to the elastic-geometric stiffness; i.e., the plastic component is neglected. Hence, the above equations are applied with the element total displacement vector replaced by its elastic component as explained later in this chapter.

2.3 ELASTIC-PLASTIC RESISTANCE OF STRAIGHT BEAM ELEMENT

For plastic analysis, the element stiffness, and hence its resistance, change when a joint yields, and in theory the element resistance needs to be evaluated separately for every stage of stiffness change (elastic, one, or two joints yielded) during the increment.

While the stiffness matrix formulation for an elastic-perfectly plastic (or elasto-plastic) straight beam element with yielded joint(s) is well established (28, 30, 41), the approximations involved in its implementation differ widely, (28). The differences arise mainly from the handling of the basic assumption that for an elasto-plastic material the incremental force vector at a yielded joint is tangent to the yield surface, which in general causes the new force point to drift from the yield surface, hence violating the assumption that the force function, Φ, has to stay on the yield surface. To keep the force point on the yield surface, several procedures were proposed, some involving iteration procedure while others involve one-step approximate force correction; both have been applied with the use of either the elastic or elastic-plastic stiffness matrix of the element (28). All these procedures treat the yielding of each joint separately when determining the elastic and plastic portions of the applied displacement, neglecting the interaction effect of one joint yielding before the other on the response of the element.

In the following section, a procedure is introduced that combines two features. First, following an iterative process, the element new force point would be made to stay on the yield surface in a manner more strictly in conformance with the theory of plasticity. Second, the incremental displacement can be large enough so that the element may undergo the process of changing from a state of total elasticity to having one yielding joint and then to having both joints yielding (43).

The basic derivation of the elastic-plastic stiffness matrix and the assumptions associated with it, (30, 28), are summarized in next section for reference.

2.3.1 Element Elastic-Plastic Stiffness Matrix

When an element yields as it goes through a displacement increment, dq, the displacement increment may be expressed as the sum of its elastic and plastic components,

$$\{dq\} = \{dq_e\} + \{dq_p\}$$

$$\begin{Bmatrix}\{dq^1\}\\ \{dq^2\}\end{Bmatrix} = \begin{Bmatrix}\{dq_e^1\}\\ \{dq_e^2\}\end{Bmatrix} + \begin{Bmatrix}\{dq_p^1\}\\ \{dq_p^2\}\end{Bmatrix} \qquad (2.5)$$

where dq_e and dq_p are the elastic and plastic displacement components, respectively, and dq_e^i and dq_p^i are their respective components at joint i. From the assumption of elasto-plastic material, the plastic displacement increment does not generate forces in the element and the element incremental nodal force vector is related only to the elastic displacement increment and the elastic stiffness matrix, k_e,

$$\{dQ\} = [k_e]\{dq_e\}$$

$$\begin{Bmatrix}\{dQ^1\}\\ \{dQ^2\}\end{Bmatrix} = \begin{bmatrix}[k_e^{11}] & [k_e^{12}]\\ [k_e^{21}] & [k_e^{22}]\end{bmatrix}\begin{Bmatrix}\{dq_e^1\}\\ \{dq_e^2\}\end{Bmatrix} \qquad (2.6)$$

where k_e is a generic term, replaced by either k_{eg} or k_o (depending on whether geometric effects are included or not), that is composed of four submatrices, k_e^{ij}, that relates the joint forces at joint i, dQ^i, to the joint displacements at joint

j, dq^j. The yielding condition at joint i is defined by the force function, Φ^i, that defines the yield surface when,

$$\Phi^i(\{Q^i\},\{Q_p^i\}) = 1.0, \tag{2.7}$$

where $\{Q^i\}$ and $\{Q_p^i\}$ are the applied force vector and the limit (plastic) force vector at joint i, respectively. When the force function satisfies this condition, the joint is considered to have reached plastic or yield state. Moreover, for elasto-plastic material the force function cannot exceed unity.

For a yielded joint, i, the normality rule states that the plastic deformation vector is normal to the yield surface and orthogonal to the element force increment,

$$\{dq_p^i\}^T \{dQ^i\} = 0 \tag{2.8}$$

For associated material, the force function is assumed to be the same as the plastic potential function, and consequently the plastic displacement increment at joint i is determined as follows,

$$\{dq_p^i\} = \lambda_i \{V^i\} \tag{2.9}$$

where λ_i is the proportionality constant for joint i and V^i is the gradient vector of the force point, Q^i, on the yield surface,

$$\begin{aligned} \{V^i\} &= \left\{ \frac{\partial \Phi^i}{\partial Q_m^i} \right\}, \quad m = 1, n \\ &= \left\{ \frac{\partial \Phi^i}{\partial Q_1^i} \; \frac{\partial \Phi^i}{\partial Q_2^i} \; \cdots \; \frac{\partial \Phi^i}{\partial Q_n^i} \right\}^T, \end{aligned} \tag{2.10}$$

where n is the number of force components that compose the yield function. From (2.5) and (2.9),

$$\{dq_e^i\} = \{\{dq^i\} - \lambda_i\{V^i\}\} \qquad \textbf{(2.11)}$$

Figure (2-4.a) shows the yield surface of a yielded joint with vectors $\{dQ\}$, $\{dq\}$, and $\{V\}$ in a two-component space. The derivation of the elastic-plastic stiffness matrix depends on whether one or both joints have yielded, as discussed below.

2.3.1.1 Case of One Joint Yielding

For this case, the plastic deformations are present only at the yielded joint (denoted as joint A), while the other joint (labeled joint B) is elastic with $\{dq_p^B\} = 0$, and $\lambda_B = 0$. The normality rule applies only at the yielded joint.

Substituting the expression for $\{dq_e\}$ using (2.11) into (2.6), then expressions for $\{dQ^A\}$ from (2.6) and $\{dq_p^A\}$ from (2.9) into (2.8), and observing that λ_A has arbitrary value, it can be determined that,

$$\lambda_A = \frac{1}{c_A}\{V^A\}^t [k_e^{A1}\ k_e^{A2}]\{dq\}$$

where,

$$c_A = \{V^A\}^T [k_e^{AA}]\{V^A\}$$

and k_e^{Aj} are the submatrices of the elastic stiffness matrix defined before.

The elastic-plastic stiffness matrix is found by substituting expressions for λ_A into (2.11), then expression for $\{dq_e\}$ from (2.11) into (2.6),

$$[k_{ep}] = \begin{bmatrix} k_e^{AA} & k_e^{AB} \\ k_e^{BA} & k_e^{BB} \end{bmatrix} \left[[I] - \left[\begin{bmatrix} \frac{1}{c_A} \{V^A\} \{V^A\}^T [k_e^{A1} k_e^{A2}] \end{bmatrix} \right] \right] \qquad (2.12)$$

$$[0]$$

where [I] is an identity matrix. The negative term consists of an N·2N non-zero matrix that corresponds to the yielded joint, complemented with the N·2N zero matrix that corresponds to the elastic joint, where N is the number of degrees of freedom per joint.

2.3.1.2 Case of Two Joints Yielding

When two joints yield simultaneously, equations (2.8) and (2.9) may be written in general matrix form,

$$\begin{Bmatrix} \{dq_p^1\}^T & \{0\}^T \\ \{0\}^T & \{dq_p^2\}^T \end{Bmatrix} \begin{Bmatrix} \{dQ^1\} \\ \{dQ^2\} \end{Bmatrix} = \begin{Bmatrix} 0 \\ 0 \end{Bmatrix}, \qquad (2.13)$$

and,

$$\{dq_p\} = \{V\}\{\lambda\}$$

$$\begin{Bmatrix} \{dq_p^1\} \\ \{dq_p^2\} \end{Bmatrix} = \begin{Bmatrix} \{V^1\} & \{0\} \\ \{0\} & \{V^2\} \end{Bmatrix} \begin{Bmatrix} \lambda_1 \\ \lambda_2 \end{Bmatrix} \qquad (2.14)$$

In a similar procedure, substituting expressions for dq_e^1 and dq_e^2 from (2.11) into (2.6), then expressions for dQ^i from (2.6) and dq_p^i from (2.9) into (2.13), a set of two simultaneous equations is obtained that can be solved for $\{\lambda\}$,

$$\{\lambda\} = [c]^{-1} \{V\}^T [k_e] \{dq\}$$

where,

$$[c] = \{V\}^T [k_e] \{V\}$$

The elastic-plastic stiffness matrix is obtained by substituting expressions for λ_1 and λ_2 into (2.11) for both joints, and back into (2.6),

$$[k_{ep}] = [k_e] \left[[I] - \{V\}[c]^{-1} \{V\}^T [k_e] \right] \quad (2.15)$$

The expressions for elastic-plastic stiffness matrix and plastic deformation are used in the calculation of the resistance and deformation of the straight beam element as described later in this chapter.

2.3.2 Yield Surface Functions: Types and Implementation

In this section the different types of yield surface functions used in this study to represent the plastic behavior of straight beams and their definition are discussed first, followed by discussion of the procedure of implementing these definitions into a computer program.

2.3.2.1 Types of Yield Surface functions

The type of yield surface defining an element plastic behavior is obviously an important factor in calculating the plastic load carrying capacity of a structure. The closer it is to the actual behavior of the element the better the predicted results, but the more difficult to implement the calculation procedure or to generalize its application. On the other hand, simply constructed models may affect the accuracy of the obtained results, (1,28), but are easier to implement into a computer program and can be used to represent a wide range of structural sections.

An example of the first type is a multi-faceted yield surface that is described by several facets in each single region of the surface (defined by principal axes), (28), creating difficulty in computer implementation. Another example is a single continuous (usually complex) equation depicting the yield surface for a limited range of a certain structural section (e.g. an I-beam section), (28). While this approach is preferable for computer implementation, it is not always possible since it is difficult to generalize for wide range of sections and sizes. These disadvantages are specially true when more than two force components contribute to the yield surface (1, 8).

In this research, four types of yield surface functions are implemented and compared for the problem in hand. These types are: 1) octahedral, 2) spherical, 3) inverse parabolic, and 4) parabolic, as shown in Figure (2-2) for two-dimensional space. The octahedral and spherical functions are considered as the lower and upper limits for the plastic behavior of the element, respectively, while the parabolic and inverse parabolic functions lie in between. The inverse parabolic function more closely represents the interaction between axial force and bending moment for steel sections, (e.g. ref. 7). In these functions, torsion and shear forces are not included since they do not have significant effect on the plastic behavior of the studied problem.

Except for the spherical function, all these functions have some discontinuity of the gradient vector either along a line where two surfaces meet, called a ridge, or at a point along one of the principal axes when more than two

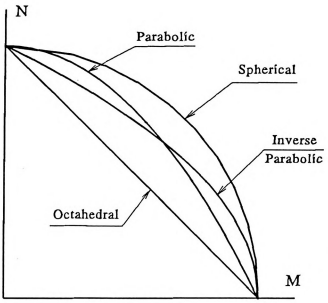

Figure 2-2 Different types of yield surface in two-dimensional space.

surfaces meet or when the function has a conical shape, called a corner. As a result, the gradient vector cannot be properly evaluated if the force point lies in a discontinuity region.

To overcome this problem, the original function is patched in the regions of discontinuity with special functions that provide definite value and continuous change of the gradient vector in each region of discontinuity, avoiding singularity of the gradient and allowing proper evaluation of the direction of the force increment tangent to the yield surface. If the force point lies in a discontinuity region, the gradient is evaluated using the special function. The force function itself, however, is always evaluated using the original function.

The patch functions used here do not provide an entirely smooth change of the gradient from one facet of the yield surface to the other, since there is

still some discontinuity between the batch function and the original yield surface. However, the main purpose of the patch function is to provide an intermediate or average value of the gradients of the original intersecting surfaces in the direction perpendicular to the ridge, for example, while still providing the same value of the gradient as the original surfaces in the direction along the ridge.

Using the gradient of the patch function, the "initial" direction of the force increment -tangent to the surface of the patch function- is determined, for example toward one of the original facets of the yield surface or in a direction parallel to the ridge. The location of the new force point is found, either in the region of the original yield surface or in the region of the patch function. If as a result the new force point drifts from the yield surface, it is returned back to it by repeating the calculation of the force increment using a new, improved value of the gradient that is equal to the average of the gradients at the beginning and end of the force increment, as described later in this chapter.

For a corner region the special function is always taken as the spherical function, while for a ridge it is specific to each of the original functions. The mathematical representation of the original yield surface functions and their special patch functions are described below.

The spherical function, Figure (2-3.a), which has no discontinuity of the gradient vector, is quadratic and is defined by the equation,

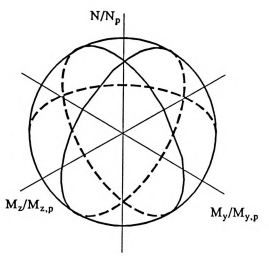

(a) spherical yield surface.

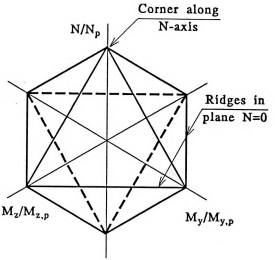

(b) Octahedral yield surface.

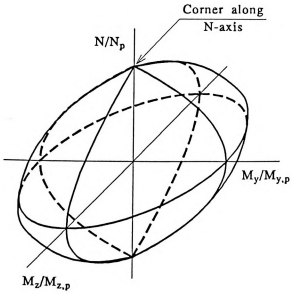

(c) Inverse parabolic yield surface.

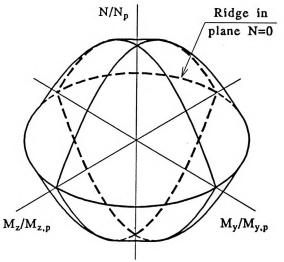

(d) Parabolic yield surface.

Figure 2-3 Different types of yield surface in three-dimensional space and locations of ridge and corner regions.

$$\Phi = \left(\frac{N}{N_p}\right)^2 + \left(\frac{M_y}{M_{y,p}}\right)^2 + \left(\frac{M_z}{M_{z,p}}\right)^2. \qquad (2.16)$$

The octahedral function, Figure (2-3.b), is defined by the equation,

$$\Phi = \left|\frac{N}{N_p}\right| + \left|\frac{M_y}{M_{y,p}}\right| + \left|\frac{M_z}{M_{z,p}}\right|. \qquad (2.17)$$

The function is composed of plane facets, each passing through -and defined by- three points of limit force. Each pair of the limit forces of the section ($\pm N_p$, $\pm M_{y,p}$, and $\pm M_{z,p}$) is located on -and defines- one of the three principal axes. Each adjacent two of these facets intersect along a straight line ridge that extends between the two limit force points common to the two facets. The ridge lies in the plane defined by the principal axes of these two limit force points. For three-component function, this plane is mathematically defined by the equation,

$$Q_r = 0,$$

where r denotes the third principal axis.

It is seen from the figure that four ridges intersect at each limit force point, forming a corner at that point. Therefore, the corner is mathematically defined by the equation,

$$Q_c = Q_{c,p}.$$

where $Q_{c,p}$ is the limit force point along the c-axis (the axis which the corner lies on).

The special function used to evaluate the gradient vector in a ridge region for three-component octahedral function is,

$$\Phi_r = \left(\frac{Q_r}{Q_{r,p}}\right)^2 + \sum_{\substack{i=1,\\ i\neq r}}^{n} \left|\frac{Q_i}{Q_{i,p}}\right|, \tag{2.18}$$

where n = 3, is the number of force components. As mentioned before, the spherical function was used to represent all corners.

The inverse parabolic function, Figure (2-3.c), is defined by the equation,

$$\Phi = \left(\frac{N}{N_p}\right)^2 + \left\{\left(\frac{M_y}{M_{y,p}}\right)^2 + \left(\frac{M_z}{M_{z,p}}\right)^2\right\}^{1/2}. \tag{2.19}$$

For this function, there are only two discontinuity regions, both along the N-axis, where the function has a conical form resulting in singularity of the gradient at the two limit points, $N = \pm N_p$. This is avoided by defining a corner region along the N-axis, with the spherical function being used as the special function.

The parabolic function, Figure (2-3.d), is defined by the equation,

$$\Phi = \left|\frac{N}{N_p}\right| + \left(\frac{M_y}{M_{y,p}}\right)^2 + \left(\frac{M_z}{M_{z,p}}\right)^2 \tag{2.20}$$

which also has only one discontinuity region in the form of a ridge in the plane N = 0, resulting in a circular ridge (elliptical when the equation is not in normalized form) in that plane. The special function used here is the spherical function.

2.3.2.2 Computer Implementation of Yield Behavior

The new yield status of an element joint, i, (whether it is elastic or plastic) for a given force vector, Q^i, at the end of a load increment is determined using the force function (i.e., the location of the force point in the force function space), $\Phi^i(Q^i)$, where three cases are possible, Figure (2-4.a). First, if the force point is inside the yield surface ($\Phi^i < 1$), then it is elastic with no plastic deformation. Second, the joint reaches the plasticity condition when the force point lies on the yield surface ($\Phi^i = 1$), but the joint does not necessarily go through plastic deformation. Finally, if the force point lies outside the yield surface ($\Phi^i > 1$), then it has advanced outside the yield surface and has gone through plastic deformation; this condition, however, violates the elasto-plastic condition, and the force point needs to be returned back to the yield surface so that $\Phi^i = 1$.

To determine the yield status of the joint for computer implementation, the yield surface is represented by a range that is defined as follows,

$$\Phi_{ul} = 1+\epsilon_\Phi > \Phi^i(Q^i, Q_p^i) \geq 1-\epsilon_\Phi = \Phi_{ll}, \qquad (2.21)$$

where Φ_{ll} and Φ_{ul} are the lower and upper limits that define the yield surface range, respectively, and ϵ_Φ is the tolerance limit. For this study, a value of $\epsilon_\Phi = 0.001$ was used.

The yield surface range divides the force function space into three distinct regions that are analogous to the three possible cases above, Figure (2-4.b): if $\Phi^i < \Phi_{ul}$ then the force point lies in the elastic range and the yield

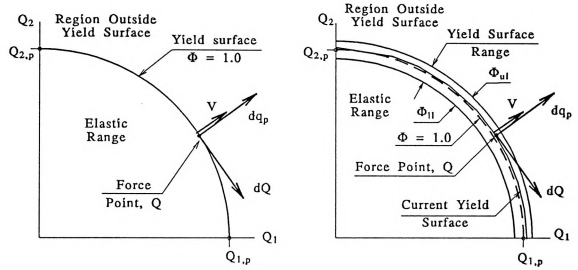

(a) Theoretical definition. (b) Computer implementation.

Figure 2-4 Definition of the yield surface and the force and plastic displacement increment vectors for a two-component joint.

status of the joint is elastic. When Φ^i lies in the yield surface range (i.e., on the yield surface), then the joint has reached plasticity and its yield status is dependent on the previous yield status of the joint at the beginning of the load increment (i.e., the plastic history of the joint). If $\Phi^i > \Phi_{ll}$, then it lies outside the yield surface and the joint yield status is plastic.

The ridges and corners of the yield surface are defined for computer implementation in a manner similar to the definition of the yield surface range, as shown in Figure (2-5) for an octahedral yield surface. The force point is considered to lie in a corner region of the yield surface along the k-axis (where k may be any one of the principal axes) if the absolute value of the force component along that axis, Q_k, normalized to its plastic force, $Q_{k,p}$, is larger than a certain limit, taken here as $1\text{-}2\epsilon_\phi$,

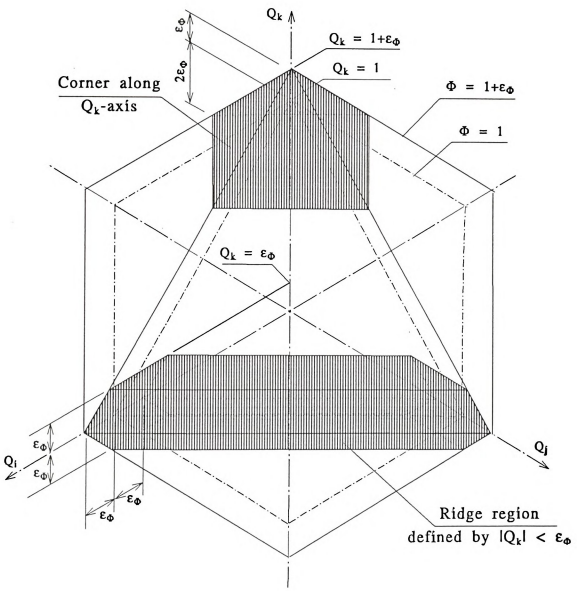

Figure 2-5 Definition of the discontinuities along ridge and corner regions of octahedral yield surface.

$$\left|\frac{Q_k}{Q_{kp}}\right| > 1 - 2\epsilon_\Phi . \tag{2.22}$$

Otherwise, the force point is considered to lie in a ridge region -defined by the k-axis- if the absolute value of the normalized force component is smaller than ϵ_Φ, Figure (2-5),

$$\left|\frac{Q_k}{Q_{kp}}\right| < \epsilon_\Phi , \tag{2.23}$$

where Q_k is the force component defining the ridge plane. Notice here that the above two equations (specially the latter one) are applied when the force function is in the yield surface range, $\Phi_{ul} > \Phi(Q^i) \geq \Phi_{ll}$. Also, the presence of a corner along each of the principal axes is checked first (before the ridge) and its tolerance is taken twice as large to avoid the situation of a force point lying in two ridge regions simultaneously.

2.3.3 Calculation of Straight Beam Elastic-Plastic Resistance

During a load increment the element displacement increment, Δq, is assumed to be linear, and in general may be divided into three segments as follows,

$$\begin{aligned} \Delta q &= dq^{ee} + dq^{ep} + dq^{pp} \\ &= dq^1 + dq^2 + dq^3 \end{aligned} \tag{2.24}$$

where dq^{ee} is the segment of Δq with both joints elastic, and dq^{ep} and dq^{pp} are those with one and two joints yielding, respectively. The element resistance is calculated in three stages each corresponding to one of the three displacement

segments, which are also numbered sequentially to correspond to their respective stage numbers. For a load increment, any one or two of the three segments may be null; however those present would take place in the order as given above.

For each stage of resistance calculation, the process is essentially the same and involves some or all of the following three steps. First, the initial tangential stiffness matrix at the beginning of the stage is used to find the initial force increment vector corresponding to the unprocessed (or unaccounted for) displacement at that stage, which is the total displacement increment, Δq, minus the displacement segments that belong to stages prior to the current one. Second, the length of the displacement segment corresponding to current stage is determined by locating the intersection point of the force vector with the yield surface for each yielding joint, and taking the joint that yields first as the governing one. Third, check for drift of the new force point from yield surface is performed for yielded joints. If present, a better estimate of the gradient vector is obtained using an iterative procedure, and the last three steps are repeated to return the force point to the yield surface until the elasto-plastic condition is satisfied.

These three steps are not present in all stages. The first displacement stage involves only the first two steps, the third stage involves only last two steps, while the second stage involves all three.

In the following sections, the procedure for locating the intersection point of the force increment vector with the yield surface at a joint, also called "the penetration point", and the method of returning the force point to the yield surface are discussed in detail, followed by detailed steps of resistance calculation.

2.3.3.1 Locating Force Penetration Point

The intersection point between the force increment vector and the yield surface needs to be found during resistance computation. This mainly arises in the resistance calculation process when determining the size of different displacement segments.

At joint i, when the old and tentative new force points, Q_o^s and $Q_n^{*,s}$, at the beginning and end of a displacement stage, s, lie in the elastic range and outside the yield surface, respectively, the force increment vector needs to be scaled back so that the new force point lies in the yield surface range. If either the old or new force point lies in the yield surface range there is no need for scaling and the scaling factor is equal to 0 or 1.

The tentative force increment vector, $dQ^{*,s}$, and new force point, $Q_n^{*,s}$, during stage s are calculated, $dQ^{*,s} = k_t^s dq^{u,s}$, and $Q_n^{*,s} = Q_o^s + dQ^{*,s}$, where $k_t^s = f(k_e, V)$ is the tangent stiffness matrix at the beginning of the stage, k_e is the elastic stiffness matrix, V is the gradient vector at the yielding joint(s), and $dq^{u,s}$ is the unprocessed displacement vector (not yet accounted for at the beginning of that stage),

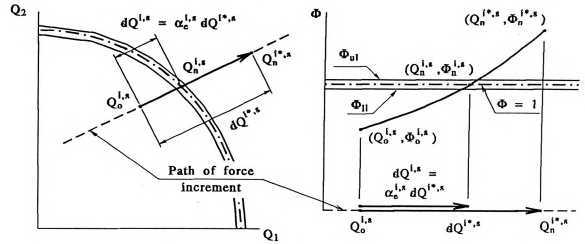

Figure 2-6 Locating the force increment penetration point of the yield surface.

$$dq^{u,s} = \Delta q - \sum_{ss=1}^{s-1} dq^{ss} \tag{2.25}$$

The penetration point at joint i during displacement stage s is defined by the scalar factor $\alpha_e^{i,s}$ that scales the tentative force increment vector, $dQ^{*,s}$, to the yield surface, Figure (2-6), so that its function satisfies the equation,

$$\Phi^i(Q_o^s + \alpha_e^{i,s}\, dQ^{*,s}) = 1. \tag{2.26}$$

The resulting scaled force and displacement vectors are $dQ^s = \alpha_e^{i,s} dQ^{*,s}$, and $dq^s = \alpha_e^{i,s} dq^{u,s}$, respectively.

The solution of equation (2.26) depends on the type of yield surface used to represent the element behavior. For spherical yield function the equation is a quadratic one and its solution is the positive one of its two roots. For other types of yield surface, the equation may be solved using an iteration method, such as the modified bisection (Regula-Falsi) method used here, where the

solution is satisfied when the target value lies in the yield surface range instead of being exactly equal to unity.

2.3.3.2 Keeping Force Point on Yield Surface

When a joint has yielded at the beginning of a displacement stage, s, the tentative force increment vector at that joint during that stage, $dQ^{i*,s}$, is tangent to the yield surface, and because the yield surface is convex in general, the new force point, $Q_n^{i*,s}$ is necessarily not in the elastic range; it lies either on or outside the yield surface. The last case violates the elasto-plastic condition, which stipulates that the force point should stay on the yield surface, and therefore the force point needs to be returned to the yield surface.

The procedure used here for force point return is an iterative procedure that involves evaluating the tangent stiffness matrix, $k_t^s = f(k_e, V_o)$, where V_o is the gradient vector at the old force point. The initial estimation of gradient vector is that of the old force point at the beginning of the stage, $V_o^{i(0)} = V^i(Q_o^s)$. If the resulting new force point, $Q_n^{i*,s} = Q_o^{i,s} + dQ^{i*,s}$, lies outside the yield surface, then its projection to the yield surface along a radial line passing through the origin, $Q_n^{i*p,s}$, is found, and the gradient used to recalculate k_t^s for the first iteration is taken as the average of the gradient at the old force point and that at the projected point, $V_o^{(1)} = \{V_o^i + V_n^{i*p}\}/2$. When the gradient is calculated in normalized form, $V_n^{i*p} = V_n^{i*}$, and the process of projecting the force to the yield surface is not needed.

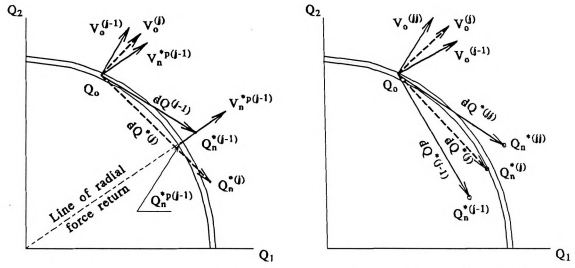

(a) New force point outside yield surface.

(b) New force point inside elastic range.

Figure 2-7 Iteration process to keep force point at yield surface.

If the new force point is still not converged (i.e., not on the yield surface) and lies outside the yield surface, the estimated value of $V_o^{i(j)}$ for iteration j is calculated as follows,

$$V_o^{i(j)} = (V_o^{i(j-1)} + V_n^{i(j-1)})/2$$

where $V_o^{i(j-1)}$ and $V_n^{i(j-1)}$ are the gradients corresponding to old and new force points during the previous iteration, Figure (2-7.a).

On the other hand, if the new force point is not converged and lies in the elastic range, then the last obtained value of V_o^i is overestimated, and a new value is calculated using the old vector used in the previous iteration, $V_o^{i(j-1)}$, and the old vector of the iteration jj that last resulted in a force point outside the yield surface, $V_o^{i(jj)}$, Figure (2-7.b),

$$V_o^{i(j)} = (V_o^{i(ij)} + V_o^{i(j-1)})/2.$$

If convergence is not achieved within a certain number of iterations (5 used here), the iteration process is stopped and the new force point at the end of the last iteration is scaled back to the yield surface (i.e., projected on it) along a radial line passing through the origin. The projected force point is taken as the final new force point, $Q_n^s = Q_n^{*p,s}$, and the force increment for the stage, $dQ^s = Q_n^s - Q_o^s$. From experience, when convergence is not achieved within a few iterations the reason is most likely related to the global structure stability, such as the current load increment being too large and exceeds the ultimate load of the structure.

When both joints of the element yield simultaneously, the iteration process is performed independently at each joint, with the resulting gradient vectors at each joint used to evaluate the tangent stiffness matrix. Similarly, the process of scaling the new force point to the yield surface is performed (when needed) only at non-convergent joint(s).

The process of projecting the tentative force point, $Q_n^{*,s}$, to the yield surface along a radial line passing through the origin is done using the procedure described by equation (2.26) in the previous section, with Q_o^s replaced by a null vector -representing the origin point- and $dQ^{*,s}$ replaced by $Q_n^{*,s}$, so that $\Phi^i(Q_n^{*p}) = \Phi^i(\alpha_c^i \cdot Q_n^{*,s}) = 1$. However, when this equation is solved by the iteration procedure the assumption that $Q_n^{*,s}$ lies outside the yield surface may not be true, since it may also lie in the elastic range. To avoid this

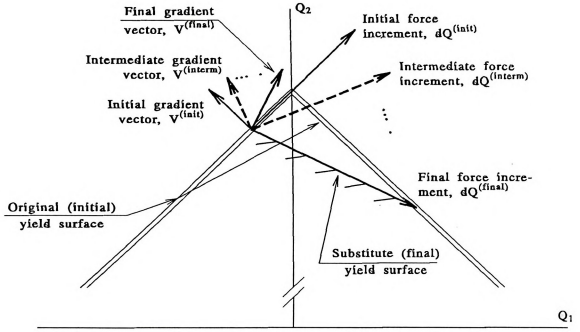

Figure 2-8 Treatment of force increment extending across surface discontinuity.

situation, the length of the tentative new force vector is doubled, $Q_n^{*,s} = 2 \cdot Q_n^{*,s}$, until its function lie outside the yield surface, ($\Phi^i(Q_n^{*,s}) > 1+\epsilon_\phi$). The solution then proceeds normally and the obtained scaling factor, α_c^i, is adjusted for the additional multiplying factor, with the final value of α_c^i being larger than unity. This technique guarantees stability of the iteration process.

For a yield surface function with discontinuous gradient, such as the octahedral function, the force increment may jump from one facet (or region) on the yield surface to another. In this case, the process of exactly following the force increment path as it moves across different facets is tedious and elaborate, since it involves finding the intersection between the force increment vector and different facets of the yield surface, and each displacement stage

may have to be further subdivided into two (or more) substages that trace the force path through each facet.

An approximation to this situation that simplifies the calculation procedure is to approximate the actual force path by a single straight line path that extends from the old force point to the new force point and passes through the elastic range, Figure (2-8). The new force point is found so that it satisfies the elasto-plastic condition using the same iterative procedure of returning the force point on the yield surface described in this section. This in effect replaces the original discontinuous yield surface by an imaginary substitute yield surface that is defined by the final gradient vector, $V_o^{i,f}$, (i.e. the final gradient vector is perpendicular to this surface) and the final force increment vector, dQ^f, which forms a part of the surface.

2.3.3.3 Steps of Resistance Computation

The initial step in calculating the element resistance is to determine the initial new yield status of the element joints (at the end of a load increment) which in turn determines the stages of resistance that need to be considered, and calculate the resistance for only those stages. After the resistance of those stages are calculated, the total element resistance during the increment, ΔQ, is calculated as the sum of those of the stages. In general, $\Delta Q = dQ^1 + dQ^2 + dQ^3$, where dQ^1, dQ^2, and dQ^3 are the element resistance for the first, second, and third stages, respectively, and the final new force point of the element, $Q_n = Q_o + \Delta Q$, where Q_o is the old force vector (at the beginning of the load

increment). In addition, plastic displacements are calculated using the applicable equations given above.

The detailed process of determining the initial yield status and different stages of resistance computations are discussed in the following sections.

A. Determining Element Initial Yield Status

The first step to determine the new yield status at each joint is to assume that the element behaves elastically and calculate the tentative element force increment, $\Delta Q^* = k_e \cdot \Delta q$, where Δq is the element displacement increment vector obtained from the structure global incremental displacement vector. The tentative new force point is found, $Q_n^* = Q_o + \Delta Q^*$. The old and new force functions at each joint, i, are calculated, $\Phi_o^i = \Phi^i(Q_o)$ and $\Phi_n^{i*} = \Phi^i(Q_n^*)$, respectively. The initial new yield status at each joint is determined as follows:

1. If $\Phi_n^{i*} > \Phi_{ul}$, the initial new yield status of the joint is plastic regardless of the old yield status, Figure (2-9.a), and $0 \leq \alpha_e^i < 1$.

2. If $\Phi_n^{i*} < \Phi_{ll}$, then the joint is in the elastic range, Figure (2-9.b), and $\alpha_e^i = 1$. Here, if the old yield status was plastic, the joint is considered to have unloaded.

3. If Φ_n^{i*} lies within the yield range, then Φ_o^i has to be checked to determine the new yield status:

3.a. If $\Phi_o^i < \Phi_{ll}$, then the new position is elastic, Figure (2-9.c), and $\alpha_e^i = 1$.

3.b. Otherwise, both old and new positions lie in the yield range (since old position is not allowed to lie in the plastic range at the end of previous

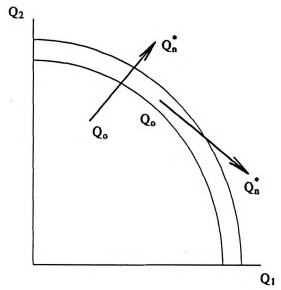

(a) New force outside yield surface.

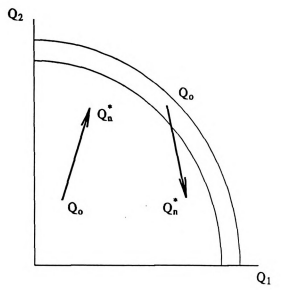

(b) New force in elastic range.

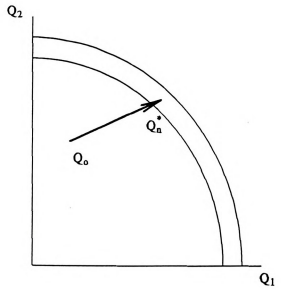

(c) Old force in elastic range, new force in yield surface range.

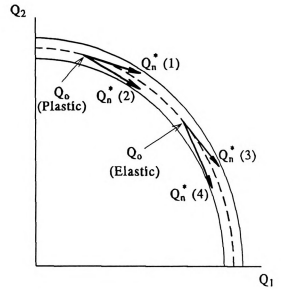

(d) Both new and old forces in yield surface range.

Figure 2-9 Determination of the initial yield status of a joint at the beginning of load increment.

increment), with the following possibilities:

- If $\Phi_n^{i*} > \Phi_o^i$ and the old yield status is plastic, then new yield status is plastic, shown as point (1) in Figure (2-9.d), and $\alpha_e^i = 0$.
- If $\Phi_n^{i*} \leq \Phi_o^i$ with the old yield status being plastic or if the old yield status is elastic, then the new yield status is elastic and $\alpha_e^i = 1$, as represented by the other three points on the same figure.

With the yield status at the beginning and at the end of the increment being found, it is possible to determine which stages of element resistance need to be considered, and proceed to calculate the resistance for the ones that are not null, as follows.

B. First Elasto-Plastic Stage

For the first displacement stage, the initial force increment is the tentative force increment found before, $dQ^{*,1} = \Delta Q^*$, and the unprocessed displacement is the total increment displacement, $dq^{u,1} = \Delta q$. Also, the old and new force points at the beginning and end of the stage are $Q_o^1 = Q_o$ and $Q_n^{*,1} = Q_n^*$, and the yield status at those points are those obtained before.

The scaling factors at each joint, α_e^1 and α_e^2, are calculated, and the smaller of these scaling factors, $\alpha_e^A = \text{minimum}(\alpha_e^1, \alpha_e^2)$, determines the joint that yields first (joint A), Figure (2-10). The force and displacement increments corresponding to this stage are calculated, $dQ^1 = \alpha_e^A \cdot dQ^{*,1}$, and $dq^1 = \alpha_e^A \cdot dq^{u,1}$, respectively. The new force point at the end of this stage is $Q_n^1 = Q_o + dQ^1$.

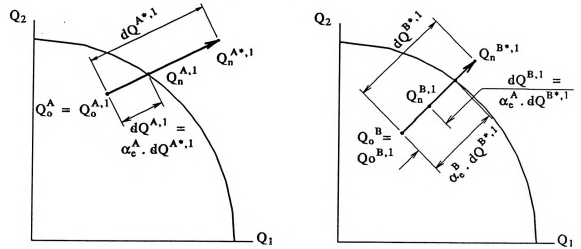

Figure 2-10 Calculation of the first stage elasto-plastic resistance of straight beam during load increment.

If $\alpha_e^A = 0$, the first stage is null (not present), and $dQ^1 = 0$, $dq^1 = 0$. In addition, if this is true for both joints (i.e. $\alpha_e^A = \alpha_e^B = 0$), the second stage is also null, and $dQ^2 = 0$ and $dq^2 = 0$. On the other hand, if the new yield status of both joints is elastic (i.e. $\alpha_e^i = 1$, i=1,2), the member behaves elastically through the whole load increment and the second and third stages are null. In this case, the final force increment and new force vectors at the end of the load increment are equal to the tentative ones, $\Delta Q = dQ^1 = \Delta Q^*$, and $Q_n = Q_n^1 = Q_n^*$, respectively, and the process of resistance calculation ends here.

When $0 < \alpha_e^A < 1$, the new force function at joint B is calculated, $\Phi_n^{B,1} = \Phi^B(Q_n^1)$, ($< \Phi_{ul}$), and used to check for the presence of second stage. If $\Phi_n^{B,1} > \Phi_{ll}$, then the new force point at joint B is in the yield range and joint B has also reached the yield status simultaneously with joint A. Therefore, the second stage is null, i.e. $dQ^2 = 0$ and $dq^2 = 0$, and the calculation proceeds to

the third stage. Otherwise $\Phi_n^{B,1} \leq \Phi_{ll}$, i.e., joint B is elastic, and the second stage is not null.

C. Second Elasto-Plastic Stage

At the beginning of this stage, the force point at joint A is on the yield surface, joint B is elastic, and $dq^{u,2}$ is not null. The unprocessed displacement and the old force vectors are calculated, $dq^{u,2} = \Delta q - dq^1$, and $Q_o^2 = Q_n^1$, and the resistance calculation proceeds as follows:

1. The tangential stiffness matrix, k_t^2, is formulated with joint A plastic and joint B elastic. The initial gradient at joint A is calculated as that of the old force point, $V_o^{A,2} = V^A(Q_o^2)$.

2. The tentative new force point and its function at joint B are calculated, $Q_n^{*,2} = Q_o^2 + dQ^{*,2}$, and $\Phi_n^{B*,2} = \Phi^B(Q_n^{*,2})$, where $dQ^{*,2} = k_t^2 \cdot dq^{u,2}$.

2.a. If $\Phi_n^{B*,2} > \Phi_{ul}$, then the new yield status of joint B is plastic, and the force increment vector, $dQ^{*,2}$, needs to be scaled back to the yield surface at joint B, $Q_n^{**,2} = Q_o^2 + dQ^{**,2} = Q_o^2 + \alpha_e^B \cdot dQ^{*,2}$, where α_e^B is the scaling factor, Figure (2-11).

2.b. If, however, $\Phi_n^{B*,2} \leq \Phi_{ul}$ then joint B is still elastic and $\alpha_e^B = 1$ (i.e. $dQ^{**,2} = dQ^{*,2}$), and the scaling process is not needed.

3. The new force function at joint A is calculated, $\Phi_n^{A**,2} = \Phi^A(Q_n^{**,2})$, and checked for drift from the yield surface:

3.a. If $\Phi_{ll} < \Phi_n^{A**,2} \leq \Phi^{ul}$, then the new force point is still on the yield surface and satisfies the elasto-plastic condition and no iteration is needed.

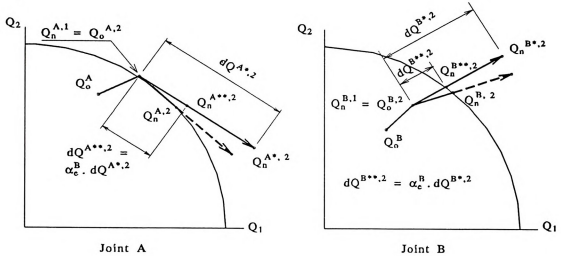

Figure 2-11 Calculation of the second stage elasto-plastic resistance of straight beam during load increment.

3.b. On the other hand, if the new force point is not on the yield surface, $\Phi_n^{A**,2} > \Phi_{ul}$ (or $\Phi_n^{A**,2} < \Phi_{ll}$ during subsequent iterations), then it has to be returned back to the yield surface. Following the iteration procedure described before, a new estimate of $V_o^{A,2}$ is obtained and used to recalculate the stiffness matrix, $k_t^{s,2}$. Steps (2) and (3) are repeated until the new force point is returned to the yield surface, as represented by the dashed line in the figure.

At the end of this stage, the final incremental and new force vectors for the second stage are $dQ^2 = dQ^{**,2}$ and $Q_n^2 = Q_n^{**,2}$, respectively, and the displacement vector, $dq^2 = \alpha_e^B dq^{u,2}$.

If $\alpha_e^B < 1$, then third stage is not null, and the old force and unprocessed displacement vectors at the beginning of that stage are found, $Q_o^3 = Q_n^2$ and $dq^3 = dq^{u,3} = dq^{u,2} - dq^2$, respectively. Otherwise, if $\alpha_e^B = 1$, then third stage is null and resistance calculation ends here.

D. Third Elasto-Plastic Stage

With the old force points at both joints on the yield surface and the third displacement segment, $dq^3 = dq^{u,3}$ not null, the third is present, Figure (2-12), and its resistance is calculated as follows:

1. The gradient vectors corresponding to the old force points at both joints, $V_o^{1,3} = V^1(Q_o^3)$ and $V_o^{2,3} = V^2(Q_o^3)$, are calculated and used as the initial gradients to evaluate the tangent stiffness matrix, k_t^3.

2. The tangential stiffness matrix, k_t^3, is formulated with both joints being plastic and the tentative incremental and new force vectors are calculated, $dQ^{*,3} = k_t^3 dq^3$, and $Q_n^{*,3} = Q_o^3 + dQ^{*,3}$, respectively.

3. The new force functions at both joints are calculated, $\Phi_n^{i*,3} = \Phi^i(Q_n^{*,3})$, i = 1,2, and each joint is checked separately for drift from the yield surface:

3.a. If at joint i, $\Phi_{ul} \geq \Phi_n^{i*,3} > \Phi_{ll}$, the new force point at that joint is on the yield surface and satisfies the elasto-plastic condition, and no iteration is needed at that joint.

3.b. On the other hand, if the force point lies outside the yield surface range (i.e., $\Phi_n^{i*,3} > \Phi_{ul}$ or $\Phi_n^{i*,3} < \Phi_{ll}$ during subsequent iterations), then the elasto-plastic condition is violated, and the force point needs to be returned back to yield surface. A new estimate of the gradient vector is calculated (as described before) only at the joint(s) that do not satisfy the elasto-plastic condition, and steps (2) and (3) are repeated until convergence is obtained.

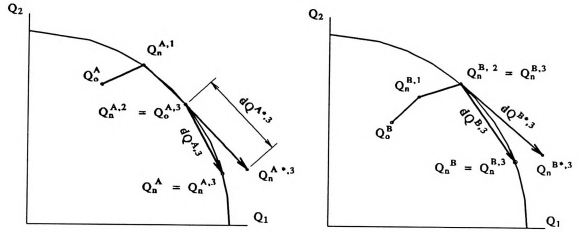

Figure 2-12 Calculation of the third stage elasto-plastic resistance of straight beam during load increment.

After convergence, the final incremental and new force vectors for this stage are calculated, $dQ^3 = dQ^{*,3}$, and $Q_n^3 = Q_n^{*,3}$, respectively. As stated before, the element resistance for the load increment is $\Delta Q = dQ^1 + dQ^2 + dQ^3$, and its new force vector, $Q_n = Q_o + \Delta Q$.

2.4 COMBINED ELASTIC AND PLASTIC NONLINEARITY

The procedure of combining both elastic and plastic nonlinearity effects is basically the combination of both separate procedures discussed above. The elastic-plastic (or tangential) stiffness matrix, equations (2.12) and (2.15), is evaluated using the elastic stiffness matrix, k_e. When geometric effects are not present, k_e is taken as the elastic-linear stiffness matrix, $k_e = k_o$. When geometric effects are present, k_e is taken as the elastic-geometric stiffness

matrix, $k_e = k_{eg}$. In this case, the elastic-plastic stiffness matrix may be written as follows,

$$\begin{aligned} [k_{ep}] &= [k_o] + [k_g] + [k_p], \quad \text{where,} \\ [k_p] &= -[k_{eg}]\left[\{V\}[c]^{-1}\{V\}^T[k_{eg}]\right] \end{aligned} \tag{2.27}$$

where k_g and k_p are the geometric and plastic incremental (or reduction) matrices, respectively.

The elastic-geometric stiffness matrix is evaluated using the elastic portion of the midpoint displacement of the current increment -as discussed before-,

$$k_{eg} = f(k_o, q_{e,mp}) \tag{2.28}$$

where $\Delta q_{e,mp} = q_{e,o} + \Delta q_e/2$, and $\Delta q_e = \Delta q - \Delta q_p$. However, Δq_e is not known beforehand since the plastic components of the increment displacement vector, Δq_p, is found only during the plastic resistance calculation, which in turn requires prior knowledge of k_{eg}.

This leads to a predictor-corrector iterative procedure where the element resistance has to be evaluated twice during every iteration, i, of the nonlinear solution for the structure equilibrium. Initially, the elastic-geometric stiffness matrix, k_{eg}, is evaluated assuming the incremental plastic displacement to be null, $\Delta q_{p(init)} = 0$ (i.e. $\Delta q_{e(init)} = \Delta q$). Using this assumption, the element elasto-plastic resistance, ΔQ, is calculated. If this initial calculation produces plastic displacements, $\Delta q_{p(corr)} \neq 0$, then the above assumption is not correct and k_{eg} needs to be reevaluated using only the improved or corrected value of the

elastic displacement increment, $\Delta q_{e(corr)} = \Delta q - \Delta q_{p(corr)}$, and ΔQ is calculated again for the same iteration.

The requirement that the element plastic resistance be calculated twice every single iteration adds considerably to calculations, while on the other hand, assuming the displacement increment to be all elastic (the first step in the above procedure) produces an error that may add to a significant difference when accumulated over many increments.

A procedure to avoid excessive calculations while minimizing error is used here where the element plastic resistance is calculated only once during every iteration for nonlinear solution of the current load increment). In this procedure, the estimate of the plastic displacement at the beginning of an iteration, i, is taken as that calculated during the previous iteration so that $\Delta q_e^{(i)} = \Delta q^{(i)} - \Delta q_p^{(i-1)}$. The elastic-geometric stiffness matrix is evaluated, $k_{eg}^{(i)} = f(k_o, (q_o + \Delta q_e^{(i)}/2))$, and the elasto-plastic resistance and plastic displacement vectors, $\Delta Q^{(i)}$ and $\Delta q_p^{(i)}$, are calculated. For the first iteration, the plastic incremental displacement is assumed to be zero, $\Delta q_e^{(1)} = \Delta q^{(1)}$.

The basis for this procedure is that when the iterative solution for the increment is near convergence, the element displacements and forces do not change significantly from one iteration to the next, and hence the element plastic displacements produced during an iteration are close to those obtained from the previous one. When the iteration for nonlinear solution of equilibrium converges during a given iteration, this implies that the error -on the element

level- due to this procedure during that iteration produces errors small enough -smaller that the allowable tolerance- to allow for convergence of the nonlinear solution. In other words, the iteration for elasto-plastic resistance on the element level is shifted to the iteration for convergence on the global structure equilibrium level.

CHAPTER III

COMPUTER PROGRAM:

SCOPE, IMPLEMENTATION, AND VALIDATION

3.1 INTRODUCTION

The computer program performs static nonlinear analysis of three-dimensional structures with the flexibility of including either or both geometric and material nonlinearities. For nonlinear solution, both direct Newton-Raphson (abbreviated N-R) method and modified Newton-Raphson method with acceleration scheme based on a modified Aitken's method were implemented with the latter being used to obtain numerical results throughout the study.

The structure ultimate load is defined more precisely using an automatic load step adjustment procedure, and the response curve may be traced beyond the ultimate load using a displacement-controlled analysis procedure that is implemented in analogy with the modified Newton-Raphson method.

The convergence criteria for nonlinear solution involves checking the norms of the residual force and displacement vectors with separate checks for translation and rotation degrees of freedom, as well as the residual structure internal energy. In addition, the solution process is checked to avoid diver-

gence and to optimize solution speed, and adjusted if necessary by means of modifying the global stiffness matrix used to obtain the solution, adjusting the load increment size, or switching the nonlinear solution method (from load-controlled to displacement-controlled analysis). The accuracy of the member resistance calculation is also verified by comparing the work of external (nodal) forces and internal energy.

The structure and loading data input includes data input modules for global analysis parameters, nodal points, structure members, basic load vectors, and incremental loading parameters. The analysis output is obtained for specified parts or all of the structure load and displacement vectors and members joint forces and displacements. This output may be obtained for every load increment or only at the ultimate load point. In addition, the load-displacement response curves for selected degrees of freedom of the structure may be separately obtained for plotting.

Detailed description and implementation of the above topics is covered in this chapter.

3.2 PROGRAM SCOPE AND IMPLEMENTATION

3.2.1 Scope and Types of Analysis

In this section, the different types of analysis are described, and their assumptions and constraints are discussed in detail.

3.2.1.1 Types of Analysis

Three types of arch ultimate loads were calculated for the parametric study. Elastic-nonlinear ultimate load involves geometric effects only, while plastic ultimate load involves plastic (or material) effects only. Combined ultimate load includes both geometric and material nonlinearities.

Geometric nonlinearity is that resulting from the change of the geometrical configuration (deflection) of the structure under loading, that affects the equilibrium of the structure. This type of analysis is called here "elastic-nonlinear" or "elastic-geometric" analysis. The elastic-nonlinear ultimate load of a structure is essentially equivalent to its buckling load under the same loading conditions.

Plastic nonlinearity is that resulting from the permanent change, or yielding, of the material response under high stress level. "Plastic" or "simple-plastic" analysis as defined here includes only the material effects.

When the analysis includes both geometric and material nonlinearities, it is called here "combined analysis". Combined analysis is the lower bound of elastic-nonlinear and plastic ultimate loads, and is more representative of the structure actual behavior. When combined analysis is dominated by one of the two nonlinear effects, it produces results that are close to or the same as those produced when only that effect is included. Nonetheless, plastic and elastic-nonlinear ultimate loads are needed for comparison with known solutions in the literature and specifications criteria based on these types of analysis.

3.2.1.2 Assumptions of Nonlinear Analysis

The nonlinear solution procedure is implemented using the assumption of fixed coordinates, where reference is made to the original configuration of the structure. Loads are applied at the nodal points.

The elements stiffness matrices are derived using the Lagrange-small rotations (Lagrange-SR) coordinates, where the member generalized deflection coordinates are measured from the original global coordinates. This derivation is valid for small member chord rotations from the original structure configuration, where θ_o and ψ_o are less than about 15 degrees (see Figure (2-1)). In addition, the member end rotations relative to the deformed member chord are assumed to be small, and the effect of torsional rotations on axial and shear strains are neglected.

When plastic effects are included (in plastic and combined types of analysis), the material nonlinearity considered here is based on the elastic-perfectly plastic material behavior, neglecting strain hardening effects, residual stresses, and the gradual spread of yielding across the member section. The member yielding is represented using the plastic hinge model, as described in chapter two, where the plastic deformations are assumed to be concentrated at its ends by formation of plastic zones of zero length while the remainder of the member behaves elastically.

3.2.2 Procedure of Incremental Analysis

In this section, the procedure of applying the incremental load and optimization of the solution speed are considered, and then the detailed steps of nonlinear solution during a load increment are described.

3.2.2.1 Incremental Analysis: Definition of the Ultimate Load and Optimization of Solution

The structure ultimate load is defined as the maximum load it can carry before failure. For the purpose of this study, failure is assumed when the structure can no longer carry any additional applied loads. The structure behavior beyond the point of ultimate load or when the structure goes into large deflection -of the magnitude of the structure dimensions- is not of practical importance, and is not considered here.

The structure ultimate load is obtained by incrementally loading the structure up to its ultimate load. The ultimate load is reached when either the solution for equilibrium becomes unstable due to divergence of the iteration process when applying a new loading increment, or when the load parameter decreases if displacement-controlled analysis is used.

Defining the ultimate load point

To define the ultimate load point more precisely, a procedure for automatic adjustment of the load increment size, similar to that suggested by Bathe and Cimento (4), was implemented.

In this procedure, the applied load for increment j, ΔP^j, is determined using the initial load parameter, $\Delta f = \Delta f_o$, where Δf_o is the load parameter specified in the data input so that,

$$\Delta P^j = \Delta f \cdot P^{lv},$$

where P^{lv} is the unit load vector applied to the structure. If the nonlinear solution process diverges during iteration, a smaller load is applied by scaling down the load parameter so that $\Delta f = sf_1 \cdot \Delta f_o$, where sf_1 is a scaling factor, and the solution for the increment is repeated using the new load parameter. If the solution is still diverging, the scaling process is successively repeated -for a total of three times- using a smaller load parameter each time,

$$\Delta f = sf_m \cdot \Delta f_o,$$

where sf_m is the scaling factor for the mth attempt. Scaling factors of 1.0 (for the initial attempt), 0.50, 0.20, and 0.05 are used for m = 0, 1, 2, and 3, respectively.

If the smallest load parameter still results in solution divergence, the structure is assumed to have reached its ultimate load at the end of the last converging load increment. On the other hand, if convergence is obtained for a load parameter, it is used in the next load increment, as explained later.

Displacement-controlled analysis was implemented to trace the load response curve beyond the limit of load-controlled analysis, and to define the ultimate load point even more precisely. However, the added accuracy in

defining the ultimate load point was found negligible, with the improvement in the value of ultimate load being typically less than 0.2%.

Optimization of Solution Speed

In addition to handling calculation divergence, the same scaling procedure described above is used to handle slow convergence rate of the solution. To avoid endless calculations for convergence during a load increment, the maximum number of iterations allowed during a load increment is limited to 40 iterations. If this limit is reached, a smaller load increment is used (by using the next smaller scaling factor) and the solution is repeated.

In addition, if the number of iterations needed for convergence during a converging load increment exceeds a certain limit (taken here as 25 iterations), then a smaller load increment is used for the following increment. By reducing the nonlinearity handled in a single increment, the calculation time spent on every increment is decreased and the total solution effort may be minimized. This process may be repeated until the smallest factor is used.

To optimize the solution speed and avoid repeatedly encountering the same likely divergence situations, the first scaled load parameter that results in solution convergence is used for at least the next four load increments to guarantee that at least the total magnitude of the last diverging load increment is successfully applied to the structure. This process avoids likely divergence situations due to, for example, unnecessarily large load increment near the ultimate load, or due to steep change in the structure stiffness.

After four consecutive fast converging increments (i.e., each requiring less than 25 iterations for convergence), a larger load parameter is used -by using the next larger scaling factor- to avoid excessively small load increments. This process may be repeated if necessary until the initial load parameter is reached again.

3.2.2.2 Steps of Analysis During a Loading Increment

The steps of nonlinear solution procedure during a load increment are described in this section for the modified Newton-Raphson method, which was used for obtaining results of this study. Direct Newton-Raphson method was implemented for comparison of convergence rate and check of the accuracy of nonlinear solution. When the implementation of direct Newton-Raphson method is different for a given step, the difference is mentioned as relevant.

The principles and implementation of the three nonlinear solution methods of analysis is explained in detail in appendix A. A summary is described here for completeness of discussion.

Theoretical Basis of Nonlinear Solution

The nonlinear equilibrium equation of the structure at the end of load increment j requires that,

$$f(D) = P^j(D) - R^j(D) = 0,$$

where $P^j(D)$ is the applied load through load increment j, $R^j(D)$ is the structure resistance at the end of that increment, and D is the (unknown) structure displa-

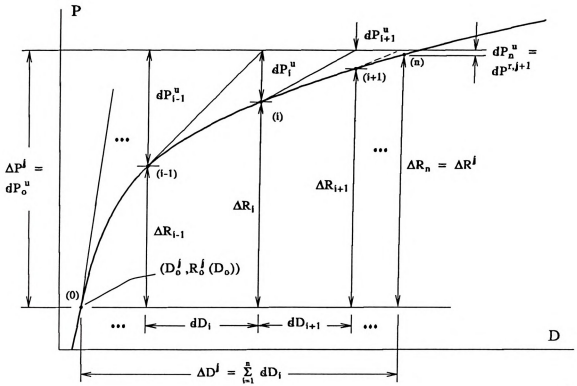

Figure 3-1 Iterative solution of nonlinear equations of equilibrium using the Newton-Raphson iteration process.

cement vector that satisfies the equation. By using Taylor's series to expand the above equation about the converged (known) solution point at the beginning of load increment j, the direct Newton-Raphson equation for iteration i of the nonlinear solution process may be written as, Figure (3-1),

$$\Delta P^j - \Delta R^j_{i-1}(D^j_{i-1}) = dP^{u,j}_{i-1} = K^j_{t,i-1}(D^j_{i-1}) \cdot dD^j_i ,$$

where ΔP^j is the applied load during increment j, $\Delta R_{i-1}{}^j(D_{i-1}{}^j)$ is the calculated structure resistance at the end of iteration i-1 as a function of $D_{i-1}{}^j$, the total structure displacement vector at the end of that iteration; $dP_{i-1}{}^{u,j}(D_{i-1}{}^j)$ is the unbalanced force at the end of iteration i-1; $K_{t,i-1}{}^j(D_{i-1}{}^j)$ is the structure tangential stiffness matrix at the beginning of iteration i-1, and dD_i^j is the unknown

incremental displacement vector during iteration i that is needed to attempt to satisfy the equilibrium equation. The solution is accepted when equation (3.1) is satisfied to within an assumed tolerance limit.

For modified Newton-Raphson method, $K_{t,i-1}^{j}$ is replaced by the stiffness matrix at the beginning of the increment, $K_{t,o}^{j}$, to avoid the calculation-intensive decomposition process for every iteration. An acceleration scheme is implemented to compensate for the resulting decrease in the speed of solution convergence.

The displacement vector through iteration i, D_i^j, may be written as $D_i^j = D^{j-1} + \Delta D_i^j$, where D^{j-1} is the displacement at beginning of current load increment, and ΔD_i^j is the accumulated incremental displacement during the current load increment through iteration i, $\Delta D_i^j = \Delta D_{i-1}^j + dD_i^j$. The increment index, j, may be omitted in the following discussion for simplicity.

Steps of Analysis for a Load Increment

The typical solution for nonlinear equilibrium for a given load increment, j, consists of the following steps:

1. Specifying the Initial Load Increment:

The analysis begins by specifying the initial load increment size, ΔP^j, to be applied for the increment, which is assumed to be the unbalanced load for the first iteration of the increment, $dP_o^{u,j}$

$$\Delta P^j = dP_o^{u,j} = \Delta f \cdot P^{lv} + dP^{r,j-1}, \qquad (3.3)$$

where Δf is the load parameter that defines the actual load forces as a ratio of the applied unit load vector, P^{lv}, and $dP^{r,j-1}$ is the residual load vector still unbalanced after convergence at the end of the previous increment. The value of Δf is influenced by the convergence rate and its value during the previous converged load increment, as discussed before.

2. Assembly and Test of the Structure Global Stiffness Matrix:

At the beginning of the increment, the structure tangential stiffness matrix, $K_{t,o}$, is formulated as a function of the structure displaced position at the beginning of the increment ($D_o^j = D^{j-1}$), and decomposed using the Cholesky decomposition method. During this process the stiffness matrix, $K_{t,o}$, is verified to be positive-definite, and if this is true its determinant is calculated and the initial displacement vector, dD_1, corresponding to the initial applied load, dP_o^u, is obtained using equation (3.4) below.

If the determinant of $K_{t,o}^j$ is small compared with the determinant of the linear-elastic stiffness matrix of the structure, the solution accuracy is verified using the procedure described in the next section. If the solution is found acceptable, the obtained displacement vector is accepted as that of the first iteration. For modified N-R method, the decomposed stiffness matrix is used during all following iterations. For direct N-R method, the stiffness matrix is updated and decomposed for every iteration but is checked for accuracy of solution only during the first iteration, since the iteration process itself acts as an indirect check in the following iterations.

On the other hand, if the stiffness matrix is not positive-definite or the solution was found unacceptable then the structure is considered either unstable or close to that state, and the solution is considered to be diverging. To overcome this situation, the stiffness matrix is formulated again using a different assumption, as explained in step (5) below, and the solution is repeated.

3. Calculation of the Structure Nonlinear Resistance:

The structure nonlinear resistance for the increment is calculated during every iteration as follows,

3.a. The incremental global displacement vector for iteration i is obtained by solving for the unbalanced load at the end of previous iteration,

$$dD_i^* = K_o^{-1} \cdot dP_{i-1}^u \quad \text{for MNR, or,}$$
$$dD_i = K_{i-1}^{-1} \cdot dP_{i-1}^u \quad \text{for DNR,}$$

where dD_i^* and dD_i are the incremental displacement vectors obtained using the modified and direct Newton-Raphson methods, respectively. For accelerated modified N-R method, dD_i^* is replaced by the modified (accelerated) vector, $dD_i = f(dD_{i-1}, dD_i^*)$, as that of current iteration. The total displacement vector for the increment is calculated as the sum of displacement vectors for all iterations up to the current one, $\Delta D_i = \Delta D_{i-1} + dD_i$.

3.b. The resistance of individual elements corresponding to ΔD_i (transformed into the element's local coordinates), is calculated as described in chapter two, and assembled into the incremental structure resistance, ΔR_i, after being trans-

formed back into global coordinates. The new unbalanced (or residual) load vector at the end of current iteration, dP_i^u, is found,

$$dP_i^u = \Delta P - \Delta R_i .$$

The vectors, dP_i^u and dD_i, Figure (3-1), are used as the residual force and displacement vectors in the process of convergence/divergence check during that iteration.

4. Check for Convergence or Divergence of the Solution:

Check for convergence or divergence of the solution process is performed using the convergence/divergence monitoring procedure described later. Depending on the results, the solution procedure continues as follows,

4.a. If the solution process has converged, then the solution for the increment is accepted and control is transferred to step (6) below.

4.b. If convergence has not been obtained yet but the solution is converging, then the solution process continues by going to step (2) above for iteration i+1.

4.c. If the solution process is determined to be diverging, then control is transferred to step (5) below.

5. Divergence Handling:

If the solution process is diverging, the load step is repeated with modified assumptions and the solution process is repeated. These modifications are implemented in the following order:

5.a. If the process diverges during the iteration process, the loading step size is probably too large and the solution is repeated with a smaller increment size using the scaling procedure described before.

5.b. If solution still diverges for the smallest load step size or if the stiffness matrix is unstable at beginning of the increment, then the structure stiffness matrix is formulated without the plastic nonlinearity effects if present. If the process still diverges in the presence of geometric effects alone or if plastic nonlinearity is not present, the stiffness matrix is formulated using the elastic-linear stiffness matrix, K_o. This option is not applicable for direct Newton-Raphson method.

5.c. If the process is still diverging after the above two steps, then the load-controlled analysis has reached its end. The ultimate load is taken as that at the end of last converging increment. If displacement-controlled analysis is required, the solution method is switched to displacement-controlled analysis and the solution process is continued. Otherwise, the analysis is ended.

6. End of Increment:

After convergence of the load increment, the final step is to update the structure and element quantities, such as displacements and forces, for use during next increment. Also, output for printing and plotting of the required data is performed. The analysis then proceeds to the next increment or is ended if the ultimate load has been reached.

3.2.3 Check for Convergence or Divergence of Solution

The solution process for nonlinear equilibrium during the load increment is monitored for convergence every iteration. If the convergence criteria is satisfied, the solution is accepted and analysis proceeds to the next load increment. At the same time, the solution process is checked for divergence to avoid large errors in the obtained solution (i.e., false convergence), false or premature termination of analysis, prevent needless calculations, or to end the analysis. If divergence is encountered, the solution is repeated using different assumptions, or the analysis is ended.

In this section, the different tests of convergence/divergence are presented first, then their implementation as a criteria for convergence or divergence is described.

3.2.3.1 Basic Tests of Solution Convergence and Divergence

The basic, or individual tests used to check the convergence and divergence of the solution process are the force, displacement, and energy tests. For the first two tests, the second order (Eucledian) norms of the residual (unbalanced) force vector of iteration i, dP_i^u, and the residual (or incremental) displacement vector of the iteration, dD_i, are traced and compared with their respective reference norms. In these tests, the translation and rotation degrees of freedom are checked separately so that,

$$
\begin{aligned}
\| dP^{u}_{(1)} \| \; / \; \| P^{ref}_{(1)} \| \; &\leq \; \epsilon_P , \\
\| dP^{u}_{(2)} \| \; / \; \| P^{ref}_{(2)} \| \; &\leq \; \epsilon_P , \\
\| dD^{u}_{(1)} \| \; / \; \| D^{ref}_{(1)} \| \; &\leq \; \epsilon_D , \\
\| dD^{u}_{(2)} \| \; / \; \| D^{ref}_{(2)} \| \; &\leq \; \epsilon_D ,
\end{aligned}
\tag{3.5}
$$

where $dP_{(1)}{}^{u}$ and $P_{(1)}{}^{ref}$ in the first equation are the force residual and reference vectors corresponding to translation degrees of freedom, and ϵ_P is the allowable force tolerance; similarly subsequent equations represent the tests for rotation forces (moments), translation displacements, and rotation displacements, with ϵ_D being the displacement tolerance limit. A tolerance limit of 0.0001 is used for ϵ_P and ϵ_D. The force or displacement test is considered convergent if both translation and rotation parts indicate convergence.

The energy test measures the work done by the unbalanced force going through the incremental displacement and compares it to the total work done for the whole increment,

$$
E^{u}_{i} \; / \; E^{ref}_{i} \quad \leq \quad \epsilon_E \tag{3.6}
$$

where $E_i{}^{u}$ and $E_i{}^{ref}$ are the residual and reference energy terms, respectively, at the end of iteration i, and ϵ_E is the tolerance limit for energy test, taken here as 0.03.

The residual force vector for iteration i is calculated as the difference between the incremental applied force and structure resistance at the end of current iteration, $dP_i^u = \Delta P - \Delta R_i$. The forces and moments in this vector contribute to their respective translation and rotation norms,

$$\|P^u_{(1)}\| = \frac{1}{n_1}\sqrt{\sum_{k=1}^{n_1} P^u(k)^2}\ ,$$

$$\|P^u_{(2)}\| = \frac{1}{n_2}\sqrt{\sum_{k=1}^{n_2} P^u(k)^2}\ ,$$

where n_1 and n_2 are the number of translation and rotation degrees of freedom in the structure, respectively. The reference norms are taken as the largest values of the total force norms throughout the analysis, evaluated after convergence of each increment,

$$\|P^{ref,jj}_{(1)}\| = \max.(\|P^{ref,j}_{(1)}\|)$$
$$\|P^{ref,jj}_{(2)}\| = \max.(\|P^{ref,j}_{(2)}\|) \qquad , j = 1, jj-1 ,$$

where jj is the current increment, and the norms of $P^{ref,j}$ for increment j are calculated similar to those of P^u above. However, minimum values of these norms are calculated as a function of the plastic forces of the structure individual members, with the plastic axial forces, N_p, and plastic bending moments, $M_{p,x}$ and $M_{p,y}$, contributing to their respective norms,

$$\text{min.}(\|P^{ref,jj}_{(1)}\|) = \frac{1}{m_1}\sqrt{\sum_{k=1}^{m_1} N_p(k)^2}\ ,$$

$$\text{min.}(\|P^{ref,jj}_{(2)}\|) = \frac{1}{m_2}\sqrt{\sum_{k=1}^{m_2} ((M_{x,p}(k) + M_{y,p}(k))/2)^2}\ ,$$

where m_1 and m_2 are the number of members contributing to each norm, respectively.

The residual displacement vector for iteration i is taken as the incremental displacement vector for that iteration, dD_i, obtained from equation (3.2),

with its two norms calculated similar to those of residual force vector above. The reference norms are taken as the largest values of the total displacement norms throughout analysis, evaluated after convergence of each increment. For the first increment, it is taken as the norm of displacement vector after first iteration. The residual displacement vector for the first iteration of every increment is found by solving for the residual force, $dD^2 = K_{t,o}^{-1} \cdot dP_1^u$.

For energy check during an iteration i, the residual energy, E_i^u, is calculated as the amount of work done by the residual forces on their corresponding residual displacements, which is the scalar product of the two vectors. Similarly, the reference energy, E_i^{ref}, is the work done by the total increment resistance force, ΔR_i, (at the end of current iteration) on its corresponding (accumulated) displacement, ΔD_i,

$$E_i^u = \{dP_i^u\}^T \cdot \{dD_i\},$$
$$E_i^{ref} = \{\Delta R_i\}^T \cdot \{\Delta D_i\}.$$

After convergence of the solution process, an additional test of the solution accuracy is made by calculating the structure internal energy on the element level through the actual force path (for example, through the member's different elasto-plastic stages) and comparing the result with the external work done by the total increment resistance force, ΔR_i, through its corresponding increment displacement, ΔD_i. At convergence, the difference should be small enough (less than 1%) for the solution to be accepted. This test is particularly

useful to verify that the approximations used to calculate the member resistance produced no significant errors.

Tests for Divergence

The divergence criteria uses the same tests for force convergence described above, but with an upper limit that indicates divergence if the test exceeds this limit in place of the tolerance limit of convergence. For force divergence test,

$$\begin{aligned} \| dP^{u}_{i(1)} \| \; / \; \| P^{ref}_{(1)} \| \;\; &\geq \;\; \tau_{1,P}, \\ \| dP^{u}_{i(2)} \| \; / \; \| P^{ref}_{(2)} \| \;\; &\geq \;\; \tau_{1,P}, \end{aligned} \tag{3.7}$$

where $\tau_{1,P}$ is the limit divergence for the residual force test. The value of $\tau_{1,P}$ used here is 10 to allow for large changes during the first few iterations without declaring false divergence.

Another test of force divergence is the rate of convergence over consecutive iterations. If the solution is converging, the residual forces and displacements for a given iteration, i, should be smaller than their values during the preceding iteration, i-1. Therefore, divergence of the iteration process may be tested by comparing the residual force norms during the current iteration to those during the preceding one. If the ratio exceeds a certain limit for both types of degrees of freedom, this test indicates divergence,

$$\begin{aligned} \| dP^{u}_{i(1)} \| \; / \; \| dP^{u}_{i-1(1)} \| \;\; &\geq \;\; \tau_{2,P}, \\ \| dP^{u}_{i(2)} \| \; / \; \| dP^{u}_{i-1(2)} \| \;\; &\geq \;\; \tau_{2,P}, \end{aligned} \tag{3.8}$$

where $\tau_{2,F}$ is the limit of divergence for the consecutive residual force test. A value of $\tau_{2,F} = 1.2$ is used here. However, to avoid reporting false divergence when the solution is near convergence, this test is applied only if its corresponding residual force test in equation (3.7) indicates large norm of the residual force, i.e., $dP^u/P^{ref} > 0.03$.

The above two tests are not applied to the displacement vectors, since the new yielding of a member joint during an iteration, for example, causes the residual displacement vector to become larger than that of the previous iteration. Also, the acceleration scheme used in the modified N-R method creates a similar situation where the displacement vector is artificially increased from one iteration to the other. Consequently, the displacement vectors are not directly included for divergence testing, but are indirectly included in the energy test.

The energy divergence tests are similar to those of the force tests,

$$\begin{aligned} &\| E_i^u \| / \| E_i^{ref} \| \geq \tau_{1,E}, \quad \text{and,} \\ &\| E_i^u \| / \| E_{i-1}^u \| \geq \tau_{2,E}, \end{aligned} \tag{3.9}$$

where E_i^u and E_i^{ref} are the residual and reference energy terms for increment i. The values of $\tau_{1,E}$ and $\tau_{2,E}$ are 10 and 1.2, respectively.

3.2.3.2 Criteria for Convergence

In general, a single convergence test is not always effective in producing accurate and robust prediction of convergence for all stages of analysis. While a stringent tolerance limit for the energy test may assure accurate prediction of

convergence, it may cause premature end of the analysis for small load increments by forcing very small absolute error tolerance and possibly producing false divergence or needless calculations before convergence. On the other hand, a relaxed tolerance limit may permit unacceptable large errors in the solution for large load increments. The same may be said about individual force or displacement tests, where the softening or hardening of the structure stiffness may cause similar problems of inconsistency.

To provide an adequate check for solution convergence during all stages of the analysis, the above three individual tests are combined to form an adaptable criteria for convergence check. In this criteria, all three tests are calculated for every iteration, and the solution is accepted if all three tests are satisfied. The rationale for this criteria lies in the different reference norms used for each of the convergence tests.

The reference value of the energy test is the only one that is directly related to the increment magnitude, while those of the force and displacement tests generally increase with the progress of analysis. For the first few load increments of the analysis, the energy test is usually satisfied well before the force and displacement tests. These two tests together, however, provide sufficient control of convergence by keeping errors small.

As the analysis approaches the ultimate load, the structure stiffness decreases and the displacement (and possibly the force) reference norms become larger, leading to more relaxed convergence check. This results in an

increase in the absolute error magnitudes allowed in the solution for the same tolerance limits. In addition, the load increment size may become smaller, resulting in even larger relative errors compared with the increment forces and displacements. The energy test imposes an upper limit on the allowable errors in the solution by directly relating the errors to the increment forces and displacements. As a result, the energy test may become the governing test of convergence during the final stages of analysis.

In addition, for modified N-R method the structure stiffness matrix used at the beginning of the increment may be different from the actual tangential stiffness matrix, as discussed before. For example, the linear-elastic stiffness matrix may be used in equation (3.4) in an analysis that involves plastic effects. This condition may result in very small displacement increments, dD_i, for the first few iterations, which may lead to false convergence. The acceleration procedure usually corrects this situation afterward. To avoid this possibility, a more stringent tolerance limit for energy test is used, $\epsilon_E = 0.001$ during the first four iterations.

3.2.3.3 Criteria for Divergence

Solution divergence may occur due to different reasons during the analysis. Divergence may occur because of the structure instability as it approaches the ultimate load, or due to sudden change in the structure stiffness during a single load increment. Also, the nonlinear solution procedure may cause instability or divergence of the solution, or may produce unacceptable

slow convergence rate. The procedures to identify and handle these situations of divergence are discussed in this section.

A. Structure Unstable at the Beginning of Load Increment

As the analysis approaches the ultimate load, the structure becomes close to instability and its stiffness close to being ill-conditioned or singular. This condition may produce significant, unacceptable errors in the obtained solution. To avoid this possibility, the solution is checked for accuracy every time the structure tangential stiffness matrix at the beginning of a load increment, $K_{t,o}$, is updated.

The proximity to the ultimate load is determined by the ratio of the determinant of the structure stiffness matrix at the beginning of the load increment, $Det(K_{t,o})$, to that of the elastic-linear stiffness matrix at the beginning of the analysis, $Det(K_o)$. If the ratio of $Det(K_{t,o})/Det(K_o) < 0.001$, then the solution is checked for accuracy, otherwise it is accepted and the nonlinear solution procedure proceeds.

The solution accuracy is checked for instability using a simple method, (13). This is done by recalculating the force and displacement vectors, $dP_{o,c}^{u}$ and $dD_{1,c}$, using double precision,

$$dD_1 = K_o^{-1} \cdot dP_o^u,$$
$$dP_{o,c}^u = K_o \cdot dD_1,$$
$$dD_{1,c} = K_o^{-1} \cdot dP_{o,c}^u.$$

The difference between the calculated and original vectors is taken as a measure of the stability of the solution. The errors in the force vector, δP, is found using the first order norm (i.e., the largest absolute value of the vector elements) of the difference between the calculated and original vectors, $dP_{o,c}^{u} - dP_{o}^{u}$, and the original vector, dP_{o}^{u}. The error in displacement vector, δD, is calculated similarly so that,

$$\delta P = \| dP_{o}^{u} - dP_{o,c}^{u} \|_1 \; / \; \| dP_{o}^{u} \|_1 ,$$
$$\delta D = \| dD_{1} - dD_{1,c} \|_1 \; / \; \| dD_{1} \|_1 .$$

If the error in either the force or displacement is larger than a certain tolerance limit, taken here as 0.001, then the stiffness matrix is considered close to being singular or ill-conditioned, and the solution is considered to be divergent. On the other hand, if both tests are satisfied, the solution is accepted and the iteration procedure proceeds.

To handle divergence due to ill-conditioned structure stiffness matrix, it is formulated again without the plastic nonlinearity if present, i.e., formulated using the elastic-nonlinear stiffness matrix and the above check is repeated. If it is still ill-conditioned using elastic-nonlinear stiffness matrix, it is formulated again using the elastic-linear stiffness matrix.

B. Divergence of Solution During Iteration

Divergence of the iteration process may be due to the fact that equilibrium is not possible under the applied load increment because it exceeds the structure ultimate load, or due to instability of the solution procedure due

to severe nonlinearity. In both cases, the unbalanced load vector produces unproportionally large displacements, that in turn produce large unbalanced forces for the following iteration. For the first case, this cycle continues and ends with divergence of the solution. For severe nonlinearity, however, the iteration process may momentarily produce large residual forces and displacements during a given iteration, but the solution may stabilize as the iteration process continues and eventually converge.

To provide a flexible divergence criteria that detects real divergence but at the same time allows for the possibility of temporary large divergence, the divergence is monitored over consecutive iterations in addition to the current iteration. For a given iteration, i, the four divergence tests described before are checked, and the number of tests that indicate divergence is found. In addition, the number of diverging tests during the previous iteration, i-1, is taken into consideration; if at least two tests were diverging during that iteration, the number of diverging tests for the current iteration is increased by one.

The divergence criteria assumes divergence of the iteration process if four of the five tests indicate divergence, otherwise the iteration process is continued. During the first four iterations where the solution and the acceleration procedure usually produces large oscillations, divergence is assumed only if all five tests indicate divergence.

In addition to testing for divergence, a maximum limit on the number of iterations for the increment is applied so the iteration process is stopped if

number of iterations exceeds 40 iterations. To handle divergence of the iteration process, a smaller load increment is found using the scaling procedure discussed before, and the solution process is repeated.

3.2.4 Data Input and Output for Analysis

The data input for the computer program is composed of four main groups, 1) Main control parameters of the structure, loads, and type of analysis, 2) description of the structure geometry and its elements and their properties, 3) Data to describe the load vectors and their combinations, and 4) Data for incremental loading and analysis parameters, and output of results.

The program control parameters specify the total number of structure members, number of element groups, number of structure nodal points, number of load vectors, and type of analysis. Nonlinear analysis parameters include the maximum number of load increments allowed throughout the analysis, the method of analysis (direct or modified N-R method), whether or not to switch to displacement-controlled analysis and the necessary information for that, and whether response curves are to be output.

Data input for the structure nodal points include their three-dimensional coordinates and restraint conditions. When the structure includes an arch as part of its geometry, the program can generate the y-coordinates of the arch nodal points given the type of arch (parabolic or circular), its span rise at the crown, and the coordinates of the end points. This procedure along with other basic input and output, and linear analysis routines was obtained from a

program written by Ralph Dusseau along with professor Robert Wen at Michigan state university, (10).

Data for each element group consists of three parts, namely the element group control parameters data, data for element property groups, and data for individual elements. The program includes three types of elements: truss element, straight beam element, and curved beam element, but only the straight beam element was used in this study. Data for control parameters specifies the number of elements in the group, number of element property groups and material properties (modulus of elasticity, yield stress, and Poison's ratio). Data for each element property group defines the section properties for that group; i.e., the area, moments of inertia, torsional constant, and ultimate plastic forces and moments of the section. Data for each element includes its two end joint nodal point numbers, and for straight or curved beams, the nodal point that defines its local y-axis in space. Also its section properties are determined by its property group number.

The program can accept up to six different "basic" load vectors, such as dead loads, live loads, or lateral loads. For a basic load vector, loading data entries for each loaded nodal point of that vector is input in the form of six load components, three forces and three moments, specified in terms of the structure global coordinate system. The program can also generate "combined" load vectors that are composed, or constructed, as combinations of the basic load vectors. These combinations are specified in the input data.

Data for incremental loading specify the load vector number to be applied, the total number of increments this vector is to be applied, NINC, the initial load increment parameter, Δf_o, the maximum number of iterations allowed before declaring divergence of the load increment, and the tolerance limits for the force, energy, and displacements convergence tests. This load vector is then applied to the structure for a total load parameter of $\Delta f_{total} = NINC \cdot \Delta f_o$, regardless of the actual number of load increments needed to apply this load parameter, or until the ultimate load is reached. This accounts for the adjustment procedure of the load increment size described before.

Output of the calculated results is controlled for incremental analysis by specifying its frequency; for example, results are output every increment, every few increments, or at the ultimate load only. Also, output for only selected nodal points and elements may be specified.

3.3 PROGRAM VALIDATION AND CHECK

The computer program was checked against various past studies, both experimental and analytical, reported in the literature with either or both geometric and material nonlinearities included. Plane and space structures, and building-type frame and arch-type structures were compared. In general, good agreement was found between the obtained results and those reported. The details of these examples are given in the following sections.

3.3.1 Geometric Nonlinearity Problems

When only geometric nonlinearity is present, the program produced very close results to those obtained using beam-column theory for so called "small-displacement" type problems (with displacement less than 1% of the structure length). The straight beam element for nonlinear elastic behavior used here is that developed by Wen and Rahimzadeh, (42), but the tolerance limits used here is smaller. As would be expected, the current program produced very close results for the same problems.

Solution of the one-story single-bay frame shown in Figure (3-2.a), is given in Figure (3-2.b), along with the solution based on beam-column theory, as reported in ref. (42) by Wen and Rahimzadeh. In both cases, one element per member was used with load step of 250 kips. It is seen that the load-displacement response and the critical load of the current solution is very close to the beam-column solution. The obtained critical load was 4710 kips, while the theoretical value was 4750 kips.

Figure (3-3.a) shows the geometry, loading, and properties of the space arch frame reported by Wen and Lange in ref. (42). The reported lateral load-displacement solutions using finite element analysis with updated and fixed coordinates are shown in Figure (3-3.b), along with current solution. The current solution is in close agreement with both solutions, and forms a lower asymptotic curve to both solutions, where it is closer to the fixed coordinates solution at the initial stage, and becomes closer to the updated coordinates

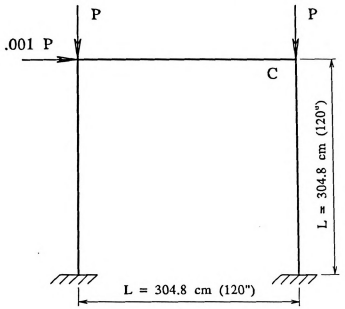

$A = 29.90\ cm^2$ ($11.77\ in^2$)

$I = 12{,}907\ cm^4$ ($3101.1\ in^4$)

$E = 2.11*10^6\ kg/cm^2$ (30,000 ksi)

(a) Dimensions, properties, and loading.

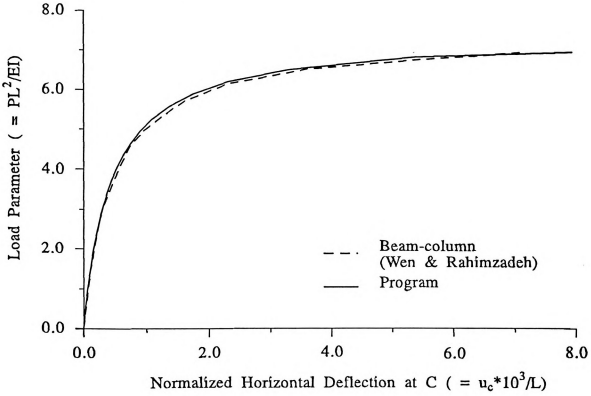

(b) Response curves.

Figure 3-2 Comparison of program with beam-column results for elastic-nonlinear behavior of single-story, single-bay frame.

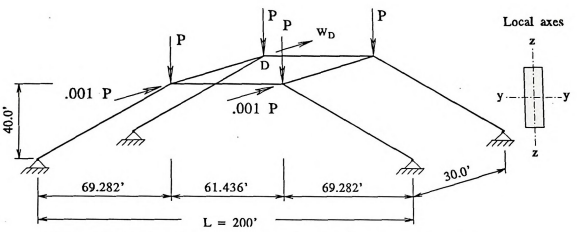

	Section 1	Section 2
A, ft^2	0.500	0.100
I_y, ft^4	0.400	0.050
I_z, ft^4	0.133	0.050
GJ, k-ft	$4.15*10^5$	$1.66*10^5$

Section 1: All Longitudinal Members

Section 2: Two Transverse Members

$E = 4.32*10^6$ ksf

(a) Dimensions, properties, and loading.

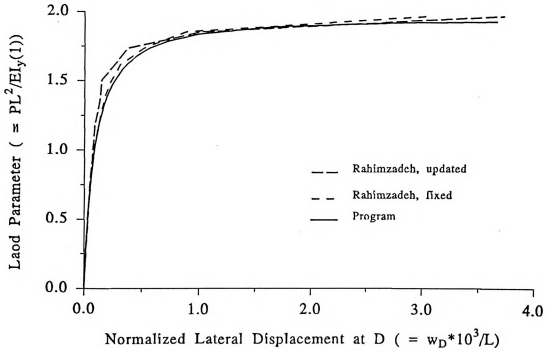

(b) Response curves.

Figure 3-3 Comparison of program with finite-element results for nonlinear-elastic behavior of a space frame.

solution after the snap stage of the response. This might be attributed to the more stringent tolerance limits of convergence used in current solution.

3.3.2 Plastic and Combined Nonlinearities Problems

The two-story, two-bay frame reported by Argyris et. al. as example 5.5 in ref. (1) is shown in Figure (3-4.a). Using the inverse parabolic function, Argyris reported that the plastic ultimate load (using simple plastic analysis) is 22.4 kp, and the combined (geometric and plastic) ultimate load is 21.5 kp.

Table (3-1) shows the calculated ultimate loads using different load functions, and the differences from those of ref. (1). It is seen that the inverse parabolic and spherical functions produce very close results to those of Argyris, with differences of less than 3%, while the other two functions generate larger differences. The simple-plastic and combined nonlinear response curves obtained by the program for the spherical function are shown in Figure (3-4.b). Also shown in the same figure is the sequence of plastic-hinge formation for the combined analysis. The sequence of plastic hinge formation for both spherical function and Argyris solutions is very similar.

Shinke, et. al., (36), reported the results of experimental tests of in-plane ultimate load of single-rib parabolic arches with rectangular cross-sections under unsymmetric loading. Using 16 elements along the arch length with equal horizontal projections, the load carrying capacity of these arches were calculated using different types of yield surface functions. Spherical, triangular, parabolic, and inverse parabolic functions were used. The results

Table 3-1 Comparison of different yield functions with calculated results of Argyris et al.

Function Type		Ultimate Load, kp.	
		Plastic Analysis	Combined Analysis
Argyris: Inverse Parabolic	P	22.40	21.50
Triangular	P	20.75	18.59
	error, %	-7.37	-13.53
Spherical	P	22.56	21.22
	error, %	0.71	-1.30
Inverse Parabolic	P	22.43	20.90
	error, %	0.13	-2.79
Parabolic	P	21.70	19.74
	error, %	-3.13	-8.19

are shown in Table (3-2), and plotted in Figure (3-5).

While the triangular yield function produced values closer to the experimental values on the lower side with error range of -1.3% to -6.7%, the inverse parabolic function produced more consistent results with errors between 9.3% to 10.4%. The spherical function produced larger errors on the higher end, with range of 14.8% to 19%. Since the plastic hinge model does not account for gradual yielding in the member, it tends to over-estimate the actual load carrying capacity of the structure because progressive yielding in its members tends to decrease its load carrying capacity by softening its stiffness,

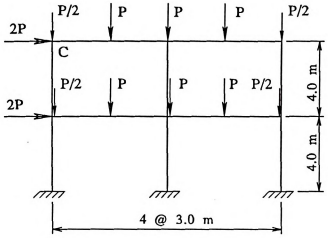

	Columns	Beams
A, m^2	0.0192	0.0118
I, m^4	$.511*10^{-3}$	$.292*10^{-3}$
N_p, kp	$73.2*10^3$	$42.0*10^3$
M_p, kp-m	$480*10^3$	$295*10^3$

$E = 2.10*10^{10}$

$\nu = 0.30$

(a) Dimensions, properties, and loading.

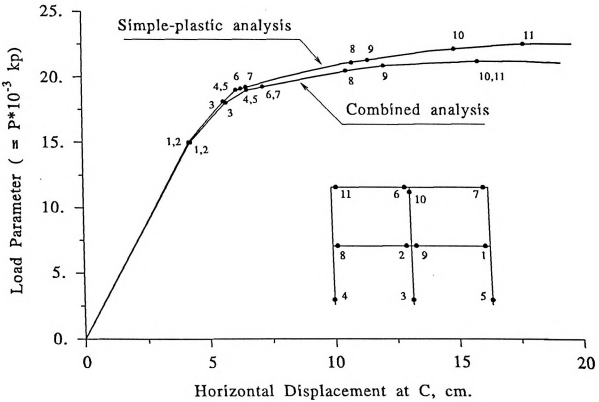

(b) Response curves and sequence of plastic hinge formation.

Figure 3-4 Behavior of a two-story, two-bay frame reported by Argyris, et. al. under plastic combined loading: response curves and failure mode.

Table 3-2 Comparison of different yield functions with experimental results of Shinke et al.

Function Type		Live to Dead Load Ratio, r' = (1-r)/r		
		0.05	0.20	0.50
Experimental Results	P	24.00	17.60	12.80
Triangular	P	23.70	16.74	11.99
	error, %	-1.25	-4.89	-6.33
Spherical	P	28.57	20.89	14.76
	error, %	19.04	18.69	15.31
Inverse Parabolic	P	26.24	19.43	14.06
	error, %	9.33	10.40	9.84
Parabolic	P	27.17	19.18	13.47
	error, %	13.21	8.98	5.23

which in turn produces larger displacement that accelerate its failure. Consequently, it is reasonable to expect the obtained results to be on the higher side of the actual capacity of the arch. Therefore, the triangular yield function, although produces the smallest errors, is not the most accurate representative of the arch behavior.

The inverse parabolic yield function, on the other hand, produced more consistent error percentage. At the same time, it more closely represents the interaction curve between axial force and bending moment for steel sections, and therefore can be assumed to produce the most reasonable results. Using the fiber model that accounts for gradual yielding and initial imperfection,

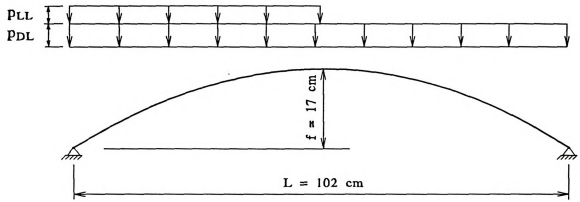

$A = 1.492\ cm^2$ $P_p = 4{,}385\ kg$ $r = p_{DL}/(p_{LL}+p_{DL})$

$I = 0.7918\ cm^4$ $M_p = 2{,}767\ kg\text{-}cm$ $r' = (1-r)/r = p_{LL}/p_{DL}$

$E = 2.06*10^6\ kg/cm^2$ $\sigma_y = 2{,}940\ kg/cm^2$ $P = (p_{DL} + 0.5p_{LL})L$

(a) Dimensions, properties, and loading.

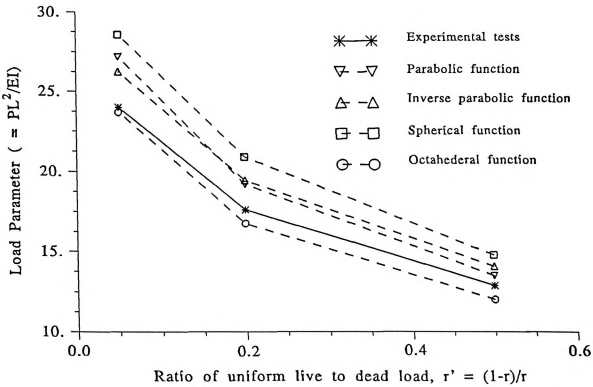

(b) Comparison of different yield functions with experimental tests.

Figure 3-5 Ultimate load of single-rib arch under vertical unsymmetric loading: comparison of different yield functions with experimental results of Shinke et. al..

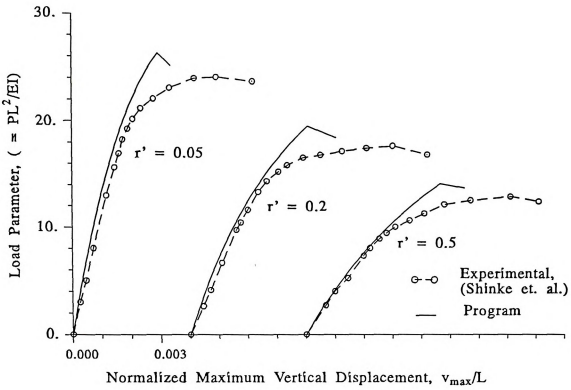

Figure 3-6 Response curves of single-rib arch under vertical loading: comparison of inverse parabolic yield function with experimental results by Shinke et. al..

Kuranishi and Yabuki (19), reported errors up to 8%. Figure (3-6) shows the response curves produced by this function as compared to the experimental curves reported by Shinke et. al., where the agreement is better as the ratio of live to dead load, r' = (1-r)/r, increases. This may be attributed to neglecting the effect gradual yielding in the arch.

CHAPTER IV

PARAMETRIC STUDY OF ARCH BEHAVIOR:

I. IN-PLANE LOAD INTERACTION

4.1 GENERAL INTRODUCTION TO PARAMETRIC STUDY

The presence of longitudinal or lateral loads on the arch -due to earthquake or wind loading, for example- results in reduction of the arch vertical ultimate load. As this reduction becomes significant, it requires consideration in the design process.

To study the effect of different load combinations on the arch ultimate load, the parametric study was divided into two parts. The first part covers in-plane behavior where interaction between longitudinal (in-plane horizontal) and vertical loading is investigated and reported in this chapter. The obtained ultimate load were compared with the arch ultimate loads under vertical unsymmetric loading. The second part, reported in next chapter, involves lateral (transverse) loading and consists of two portions where the interaction between lateral and vertical loading was studied first. In addition, the ultimate load surface (in three-dimensions) of a representative arch was constructed to explore the effect of combining all three types of loading.

The main parametric study variables include the loading combination, support type (two-hinged or fixed), type of analysis (plastic, elastic nonlinear, or combined), and the slenderness ratio. In addition to the arch total ultimate load, the study examined the vertical component of the ultimate load, the interaction curves between different loads for different types of analysis, failure modes and response curves, plastic hinge formation patterns, and the force path at the arch quarter point. For lateral loading, the effect of arch section proportions on ultimate load was also investigated.

The basic arch model and parameters, and the load patterns and combinations used in the study are described first in the next two sections.

4.1.1 Basic Arch Model and Parameters

The parametric study was carried out using a parabolic steel arch with rise to span ratio, f/L = 0.15. The arch was modeled using the straight beam finite element. Sixteen elements with equal horizontal projection, as shown in Figure (4-1.a), were used to model the arch. A preliminary investigation of the effect of the number of elements on the ultimate load produced insignificant improvement (less than 0.5%) when the arch was modeled using 32 elements. The material properties used are those typical of steel, with the ratio of elasticity modulus to yield stress, $E/\sigma_y = 805.5$.

Two section proportions were chosen for this study, Figure (4-1.b). The first section, denoted S1, was used in the first part for in-plane loading (vertical and longitudinal load interaction), with dimensions representative of a

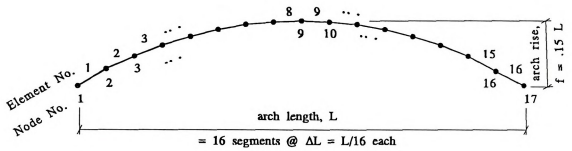

(a) Arch finite element model.

	Section S1	Section S2
D/B	2	1
D/t_f	50	100
D/t_w	100	100
I_y/A^2	4.085	4.125
r_y/r_z	2	1

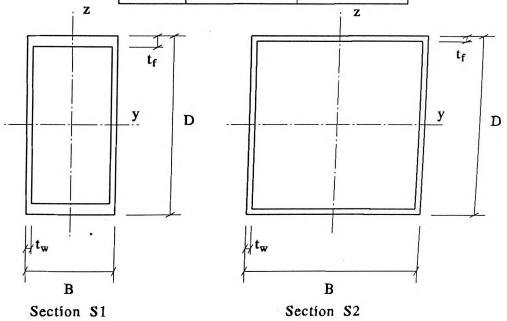

(b) Dimensions and proportions of arch sections.

Figure 4-1 Finite element model and section properties of the arch used for parametric study.

typical cross section of a box-type single arch. This section has proportions of depth to width ratio, $D/B = 2$, depth to flange thickness ratio, $D/t_f = 50$, and depth to web thickness, $D/t_w = 100$. The second section, denoted S2, was used in studies involving lateral loading and has symmetric geometric properties about its two axes of symmetry to serve as a standard section, with $D/B = 1$, $D/t_f = 100$, and $D/t_w = 100$.

The above three ratios define (or result in) one nondimensional variable for the in-plane study, I_y/A^2. For out-of-plane study, an additional non-dimensional variable is defined by these ratios, i.e., the ratio of in-plane to the out-of-plane radius of gyration, r_y/r_z. The values of I_y/A^2 for the two sections are 4.085 and 4.125, respectively, and the corresponding ratios of r_y/r_z are 1.0 and 2.0. The resulting in-plane properties of the two sections (A, I_y, N_p, and M_{py}) for the same in-plane slenderness ratio, L/r_y, are similar enough (with difference of less than 1%), that the in-plane section properties are considered constant for the two sections in the study of the arch behavior under lateral loading. For in-plane loading, the results obtained from the two sections were virtually identical.

For in-plane study, the arch slenderness ratio, L/r_y, was varied from 75 to 375 with increments of 25. For the study involving lateral load, L/r_y increments of 50 over the same range were used along with an extra point at $L/r_y = 450$.

4.1.2 Loading Distributions and Combinations

The distributions of different loads used in the study are shown in Figure (4-2). For vertical load, the probability of unsymmetric live load occurrence simultaneously with an earthquake is very small. Therefore it was taken in this study as uniformly distributed load along the horizontal projection of the arch with slight unsymmetry (r = 0.99). The slight unsymmetry is assumed here to produce unsymmetric deflection mode under vertical-only load throughout the loading process and avoid the sudden shift from symmetric mode to unsymmetric one at failure if a perfectly symmetric load was used.

The unit vertical load, P_{vu}, is defined as the total load applied to the arch using a unit uniformly distributed vertical load (with intensity of one force unit per unit horizontal length of the arch, p_{vu}), so that $P_{vu} = L \cdot p_{vu}$ (neglecting the effect of the slight unsymmetry). The uniformly distributed loads are lumped into concentrated loads that are applied through the arch nodes as shown in Figure (4-3) for this and other loading cases.

The arch ultimate vertical load, P_{vo}, is expressed in terms of P_{vu} and the load parameter at ultimate load, f_o, so that, $P_{vo} = f_o \cdot P_{vu}$, and it may be expressed in non-dimensional form, $P_{vo} \cdot L^2/E \cdot I_y = p_{vo} \cdot L^3/E \cdot I_y$. Figure (4-4) shows the change with L/r_y of the ultimate load of two-hinged arch under symmetric vertical loading using plastic, elastic, and combined types of analysis. It is seen from the figure that the elastic ultimate load is essentially constant when expressed in non-dimensional form.

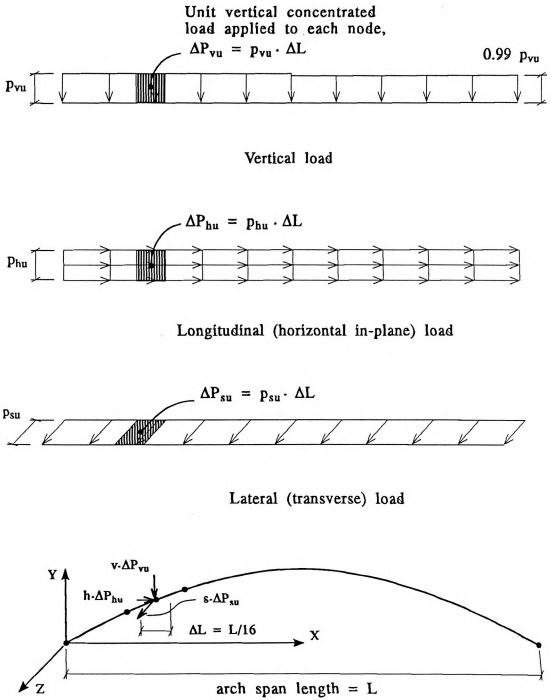

Figure 4-2 Individual unit loading distributions in the vertical, longitudinal, and lateral directions.

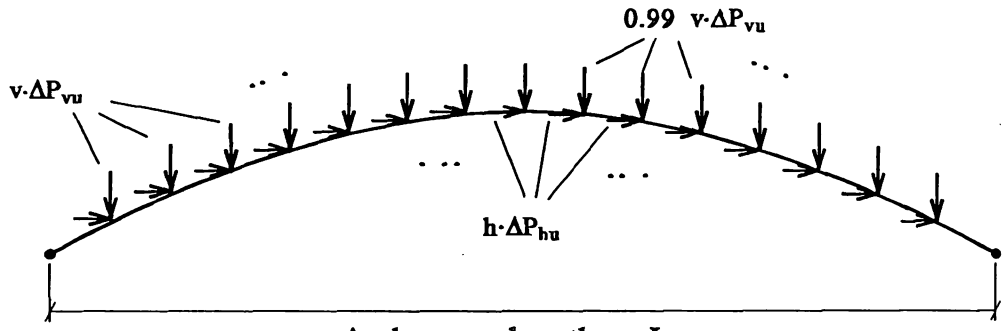

Arch span length = L

applied unit load vector, $P_{tu} = v \cdot P_{vu} + h \cdot P_{hu}$

$v + h = 1$

(a) Vertical and longitudinal loading.

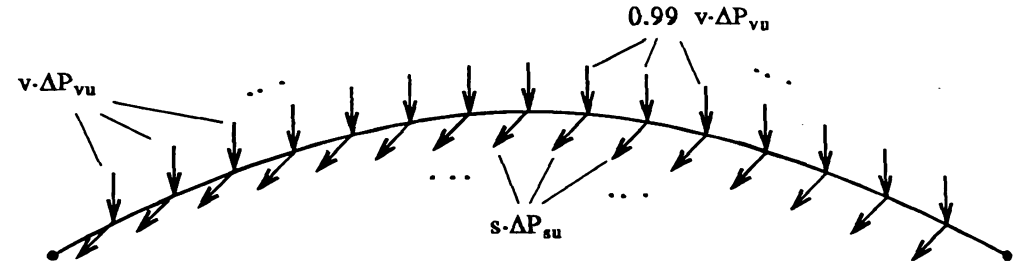

applied unit load vector, $P_{tu} = v \cdot P_{vu} + s \cdot P_{su}$

$v + s = 1$

(b) Vertical and lateral loading.

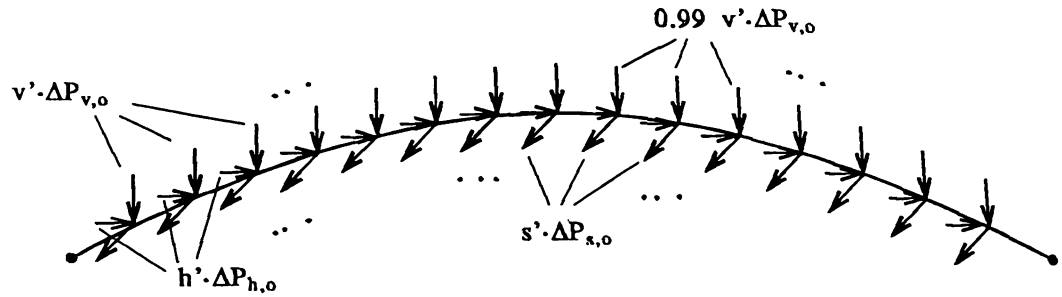

applied unit load vector,

$P'_{tu} = v' \cdot P_{v,o} + h' \cdot P_{h,o} + s' \cdot P_{s,o}$

$v' + h' + s' = 1$

(c) Vertical, longitudinal, and lateral loading.

Figure 4-3 Applied loading combinations for different loading cases of the parametric study.

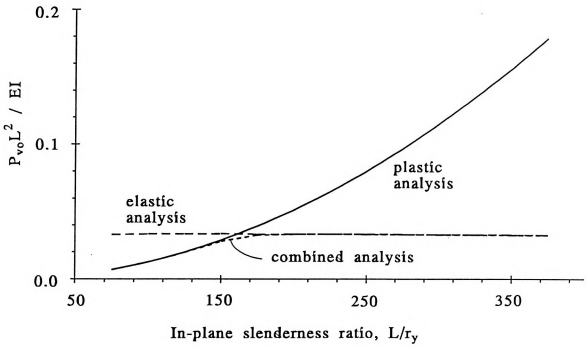

Figure 4-4 Variation of ultimate load of two-hinged arch under vertical load (r = 0.99) using different types of analysis, with in-plane slenderness ratio, L/r_y.

Longitudinal (in-plane horizontal) forces on arch structures result mainly from earthquake loading where dynamic effects generate longitudinal and vertical inertial forces in the arch. For static analysis, the longitudinal forces may be assumed to be proportional to the distribution of the structure mass along the arch horizontal length. This assumption is justified because this distribution represents the worst case loading by producing unsymmetric failure mode, which is the first modal shape of the arch. In addition, since the arch is a relatively simple structures -as compared to multi-story buildings, for example- this mode is dominant compared to higher modes.

Lateral loading was also assumed to be uniformly distributed along the arch horizontal length, since wind loads produce this distribution. Also,

earthquake lateral inertial forces of the same distribution produce the worst case lateral loading. Similar to vertical load, the unit longitudinal and lateral loads are expressed in terms of their respective uniformly distributed loads as $P_{hu} = L \cdot p_{hu}$ and $P_{su} = L \cdot p_{su}$. Notice that the value (i.e., the magnitude) of P_{vu}, P_{hu}, and P_{su} is the same although their directions are different.

When applying a combination of two or all of the three basic loads to the arch, for example vertical and longitudinal loading, the applied unit total load, P_{tu}, is applied as a proportional load with the sum of the scaling factors being equal to unity so that,

$$P_{tu} = v \cdot P_{vu} + h \cdot P_{hu}$$

$$= (1-h) \cdot P_{vu} + h \cdot P_{hu},$$

where $(v \cdot P_{vu})$ is the vertical component of P_{tu}, defined as a proportion of the unit vertical load, P_{vu}, (defined above) using the scaling factor v. Similarly, $(h \cdot P_{hu})$ is the longitudinal component of P_{tu}, defined in terms of P_{hu} by the scaling factor h. Also, $v + h = 1$. For proportional loading, the ratio of the longitudinal component to the total load is constant throughout the loading process, i.e., $h \cdot P_{hu} / P_{tu} = h =$ constant. In other words, the unit total load, P_{tu}, always has the same value for all values of h and v, since the absolute sum of its components, $v \cdot P_{vu}$ and $h \cdot P_{hu}$ is always constant.

Similarly, the unit total load due to combined vertical and lateral loads is,

$$P_{tu} = s \cdot P_{su} + v \cdot P_{vu},$$

where s is the ratio that defines lateral (or transverse) load. Also, $s + v = 1$.

Three-dimensional loading was used to construct the ultimate load surface in three-dimensional space using combined analysis. For this purpose it was more suitable to form the unit total load in terms of the arch combined ultimate loads under vertical-only, longitudinal-only, or lateral-only loads, i.e., $P_{vo,c}$, $P_{ho,c}$, and $P_{so,c}$, respectively, so that,

$$P_{tu}' = v' \cdot P_{vo,c} + h' \cdot P_{ho,c} + s' \cdot P_{so,c},$$

where v', h', and s' are the respective scaling factors corresponding to vertical, longitudinal, and lateral ultimate loads. In addition, $v' + h' + s' = 1$. Note that P_{tu}' does not always have constant value.

4.2 IN-PLANE LOAD INTERACTION: INTRODUCTION

The in-plane interaction between vertical and longitudinal loads and its effect on the arch behavior is presented in the rest of this chapter. The main objective is to study the arch ultimate load and how it is affected by different variables, such as the arch slenderness ratio, type of analysis, and the longitudinal load ratio. Other aspects of arch behavior, like the interaction curves between vertical and longitudinal components of the load, failure modes, and tracing the force path at the quarter point of the arch with the progress of loading are also studied.

Both types of arch end support conditions, two-hinged and fixed, are considered. The behavior of two-hinged arch is presented first, followed by the behavior of fixed arch. To study the effect of longitudinal load on the arch

behavior, the ratio of longitudinal load to total load, h, is varied from 0.0 (vertical load only) to 1.0 (longitudinal load only), with intermediate values of 0.0625, 0.25, 0.50, and 0.75. Values for other variables were discussed in the previous section.

Finally, the arch ultimate load under unsymmetric vertical loading was studied and the obtained results were compared with the arch ultimate load under vertical and longitudinal loads. In particular, the effect on the arch capacity to carry vertical symmetric load (e.g., dead load) due to the presence of vertical unsymmetric load or longitudinal load is studied and compared for the two cases. The vertical load unsymmetry ratio, r, is varied from 0.0 (arch loaded on half span only) to 0.99 (practically symmetric vertical load), with intermediate values of 0.33, 0.50, and 0.88.

4.3 BEHAVIOR OF TWO-HINGED ARCH UNDER VERTICAL AND LONGITUDINAL LOADING

The ultimate load and behavior of two-hinged arch under different types of analysis are presented in this section.

4.3.1 Variation of the Ultimate Load of Two-Hinged Arch with Slenderness Ratio

The ultimate load of two-hinged arch is obtained for the three types of analysis, namely plastic analysis where only plastic effects are included, elastic nonlinear analysis where only elastic nonlinearity (or geometric nonlinearity) is included, and combined analysis where both plastic and elastic nonlinearities

are included. The last type represents the lower limit of the first two, while the AASHTO design formula is based on the elastic analysis. In the following, discussion of the three types of analysis is presented.

4.3.1.1 Plastic Ultimate Load of Two-Hinged Arch

The total plastic ultimate load of parabolic arch under a vertical symmetric uniformly distributed load, $P_{vo,p}$, is obtained for reference based on linear analysis as the load that causes the stress at the arch support to reach the yield stress,

$$P_{vo,p} = 2A\sigma_y / \sqrt{\frac{1}{16}(\frac{L}{f})^2 + 1} \qquad (4.1)$$

This formula applies to both cases of two-hinged and fixed arch, since the arch fails due to thrust action at the support in both cases.

Figure (4-5.a) shows the change with L/r_y of the arch total plastic ultimate load, $P_{t,p}$, normalized to the vertical-only plastic ultimate load, $P_{vo,p}$. From this figure it is seen that the presence of longitudinal load generally reduces the arch ultimate load from its capacity under vertical-only load. The exception is for low values of h and low values of the slenderness ratio, L/r_y, where it is slightly higher, because the longitudinal component of the ultimate load has negligible effect on reducing the vertical load carrying capacity of the very stiff arch.

For a given value of h, the arch normalized ultimate load, $P_{t,p}/P_{vo,p}$, decreases as L/r_y increases. The relationship is nearly linear (i.e. has constant

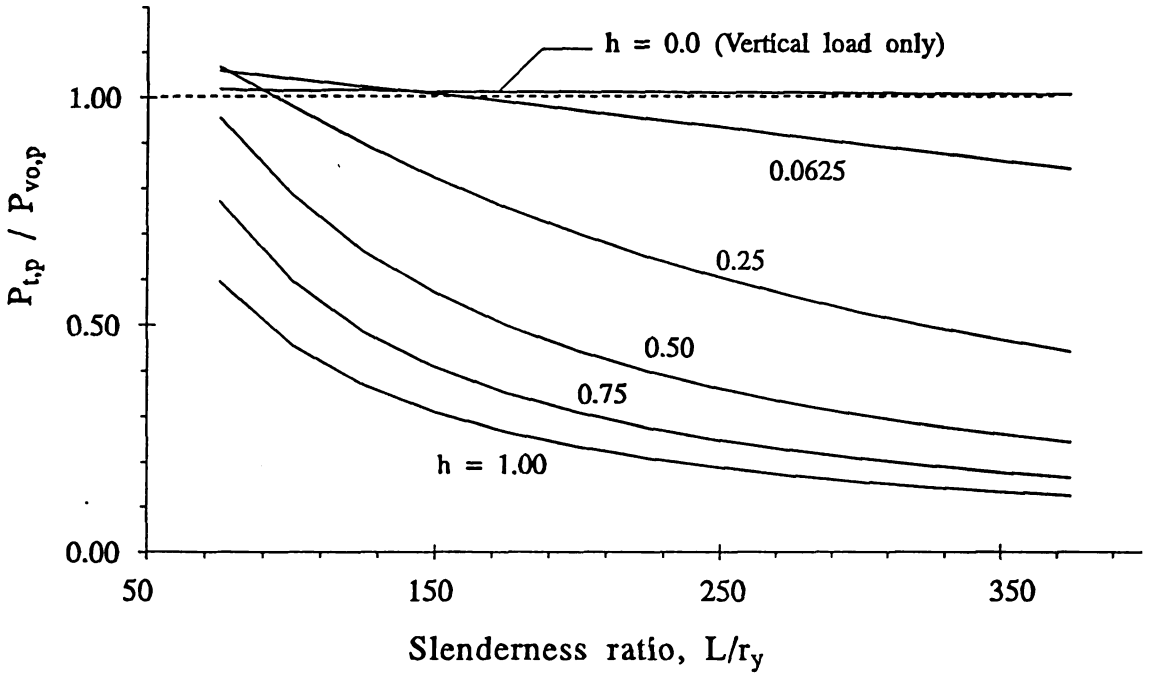

(a) Total load normalized to $P_{vo,p}$.

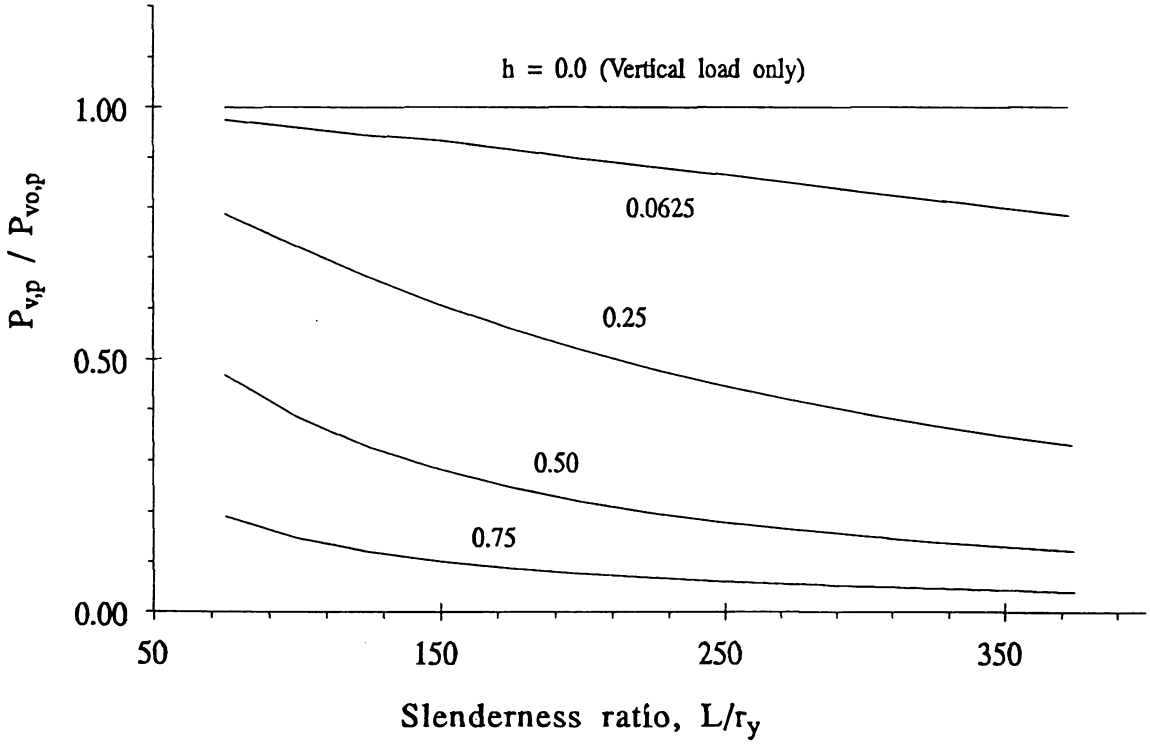

(b) Vertical component normalized to $P_{vo,p}$.

Figure 4-5 Variation with L/r_y of the plastic ultimate load of two-hinged arch under vertical and longitudinal loading.

rate of decrease) along the L/r_y axis for small values of h (= 0.0625). For larger values of h, the relationship changes to nonlinear with the rate of decrease being largest for low values of L/r_y then stabilizing to a constant rate as L/r_y increases. In general, the plastic ultimate load becomes more sensitive to the presence of longitudinal load (i.e., its decrease from $P_{vo,p}$ is larger) as L/r_y increases. The ratio of the longitudinal-only to vertical-only ultimate loads, $P_{ho,p}/P_{vo,p}$, ranges from 60% (for L/r_y = 75) to 12% (for L/r_y = 375).

The vertical component of the total plastic ultimate load, $P_{v,p}$, normalized to $P_{vo,p}$ is shown in Figure (4-5.b), where the trends are similar to those of the total ultimate load but with less degree of nonlinearity along the L/r_y axis. Since the arch capacity under longitudinal-only load is smaller than its capacity under vertical-only load, the arch ultimate load becomes controlled by its longitudinal component as h increases; i.e., the arch reaches its ultimate load when its longitudinal component ($P_{h,p}$) approaches its capacity ($P_{ho,p}$). Consequently, as $P_{ho,p}/P_{vo,p}$ decreases, the ultimate load and therefore its vertical component decrease for the same value of h.

4.3.1.2 Elastic-Nonlinear Ultimate Load of Two-Hinged Arch

Figure (4-6.a) shows the arch elastic ultimate load normalized to $P_{vo,p}$. It is seen that the relationship is similar for all values of the longitudinal load ratio, h, and all curves are grouped in a narrow band. However, the nonlinearity of the curves along the L/r_y axis increases with the increase of h, with the

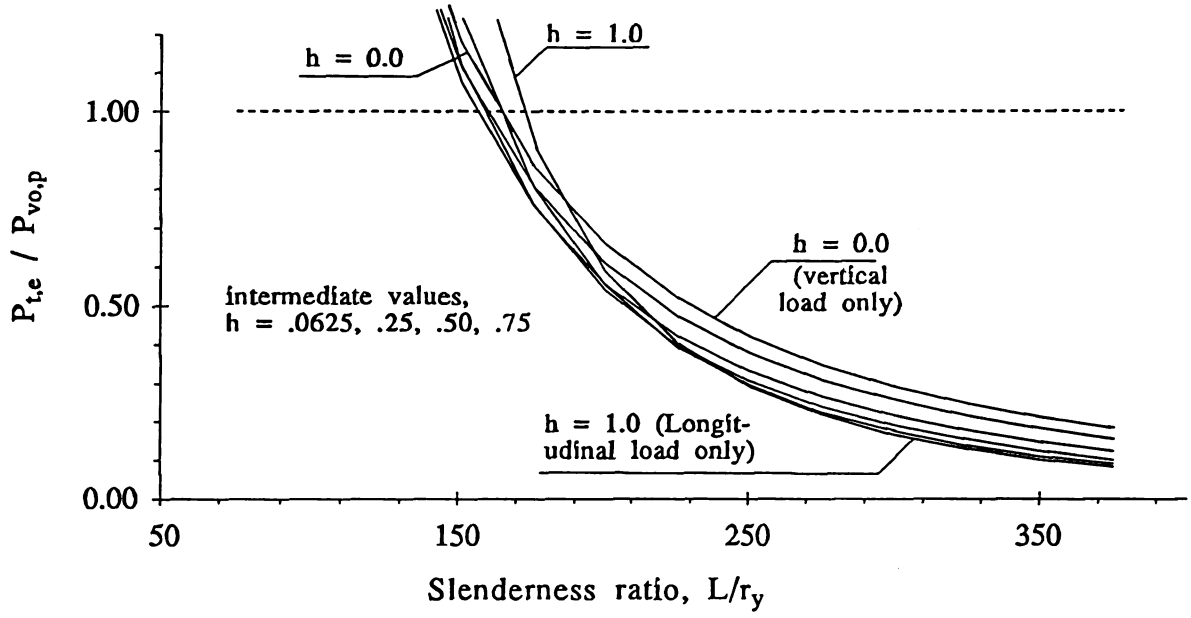

(a) Total load normalized to $P_{vo,p}$.

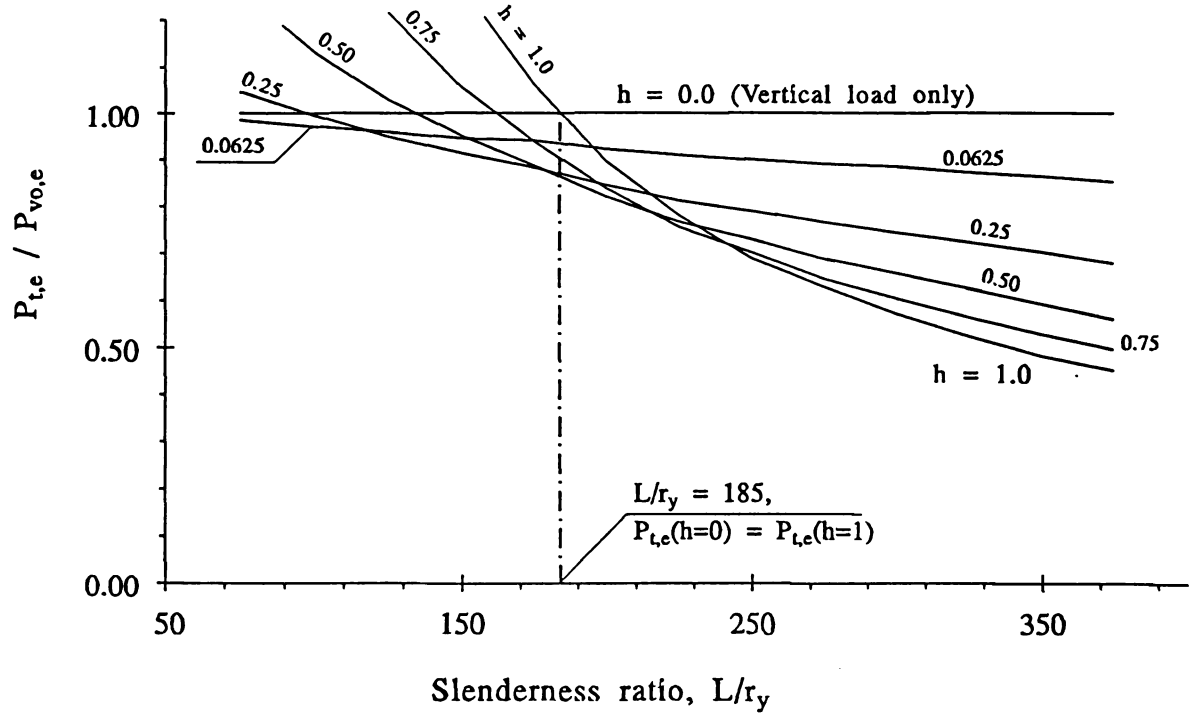

(b) Total load normalized to $P_{vo,e}$.

Figure 4-6 Variation with L/r_y of the elastic-nonlinear ultimate load of two-hinged arch under vertical and longitudinal loading.

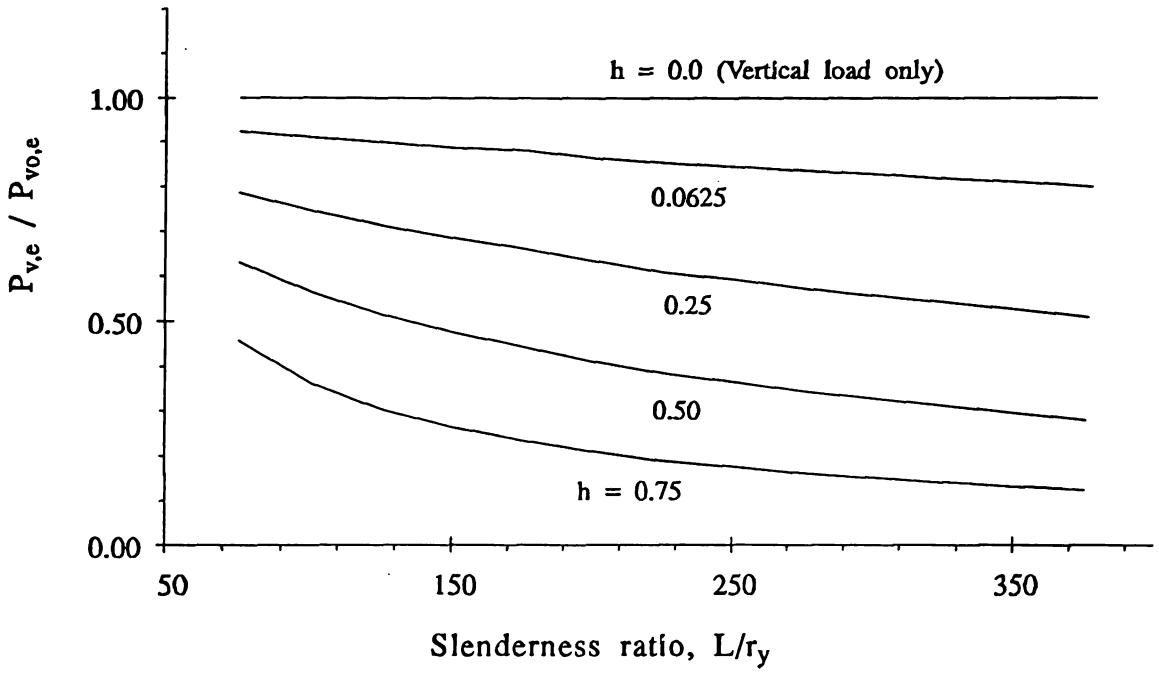

(c) Vertical component normalized to $P_{vo,e}$.

Figure 4-6 continued.

curves shifting down and to the right at the same time. In other words, the ultimate load for longitudinal-only load, $P_{ho,e}$, is higher than that for vertical-only load, $P_{vo,e}$, for stiff arches. But as L/r_y increases, $P_{ho,e}$ decreases by a faster rate to become lower than $P_{vo,e}$ for slender arches. These trends are shown more clearly in Figure (4-6.b) where the same results are normalized to the elastic ultimate vertical-only load, $P_{vo,e}$. The two curves of h = 0.0 and h = 1.0 intersect (i.e., $P_{ho,e} = P_{vo,e}$) at $L/r_y = 185$.

The vertical component of the ultimate load, $P_{v,e}$, is shown in Figure (4-6.c) normalized to $P_{vo,e}$. It is seen that for most of the studied range of L/r_y, the rate of reduction of $P_{v,e}$ with h is largest for small values of h. Along the L/r_y axis, the reduction (for constant h) is smallest for low L/r_y, and becomes

larger as L/r_y increases. These trends are similar to those of plastic analysis, Figure (4-5.b), but the reductions are smaller than those of plastic analysis, i.e., the ratio of $P_{ho,e}/P_{vo,e}$ is always larger than the corresponding ratio of $P_{ho,p}/P_{vo,p}$ for the same L/r_y.

4.3.1.3 Combined Ultimate Load of Two-Hinged Arch

The arch combined ultimate load (where both plastic and elastic-nonlinear effects are included) is shown in Figure (4-7.a), normalized to $P_{vo,p}$. The combined ultimate load basically represents the lower envelope of the individual plastic and elastic-nonlinear curves, where it becomes asymptotic to the elastic curve for high slenderness ratio, L/r_y, ($L/r_y > L/r_{y)cr} = 165$, which is defined as the value of L/r_y where plastic and elastic ultimate vertical-only loads are equal) whereas it approaches the plastic curve for lower L/r_y.

Fig (4-7.b) shows the total combined ultimate load normalized to the combined ultimate load under vertical-only load, $P_{vo,c}$. In this figure, the reduction in combined ultimate load due to the presence of longitudinal load (for a given h) is largest for the region around the critical slenderness ratio, $L/r_{y)cr}$. The formation of this plunge in the curves is due to the transient shift of the combined curves from following the plastic curves to following the elastic curves (which are higher, i.e., exhibit less reduction than the correponding plastic ones for the same values of h and L/r_y) in the region around $L/r_{y)cr}$.

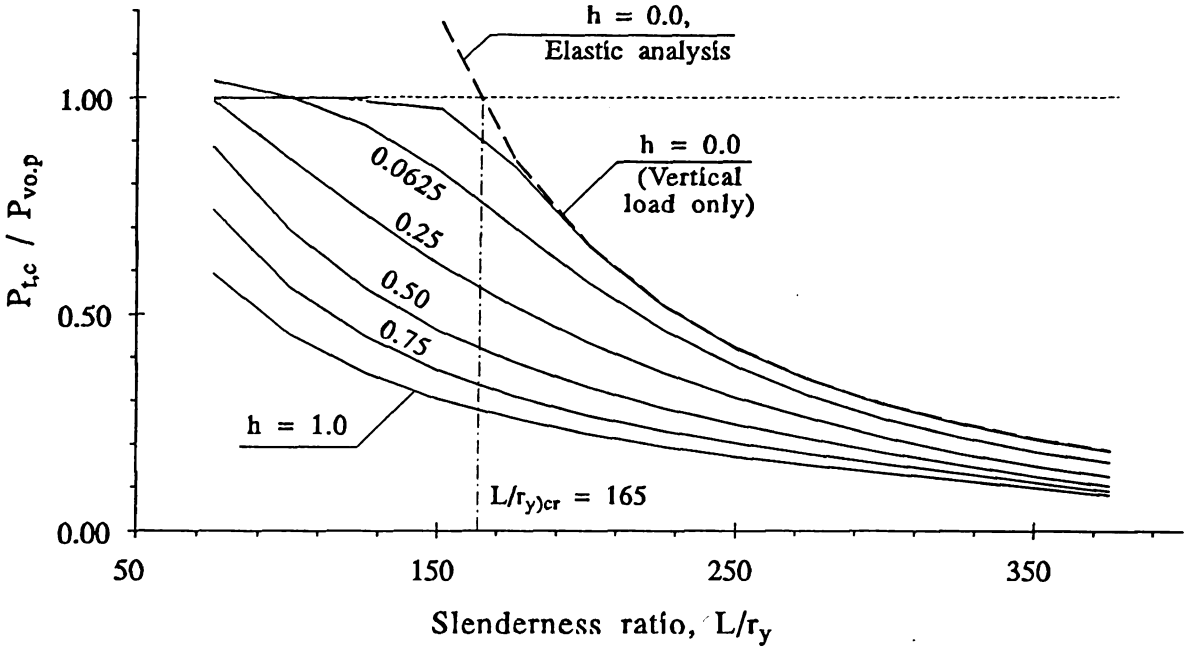

(a) Total load normalized to $P_{vo,p}$.

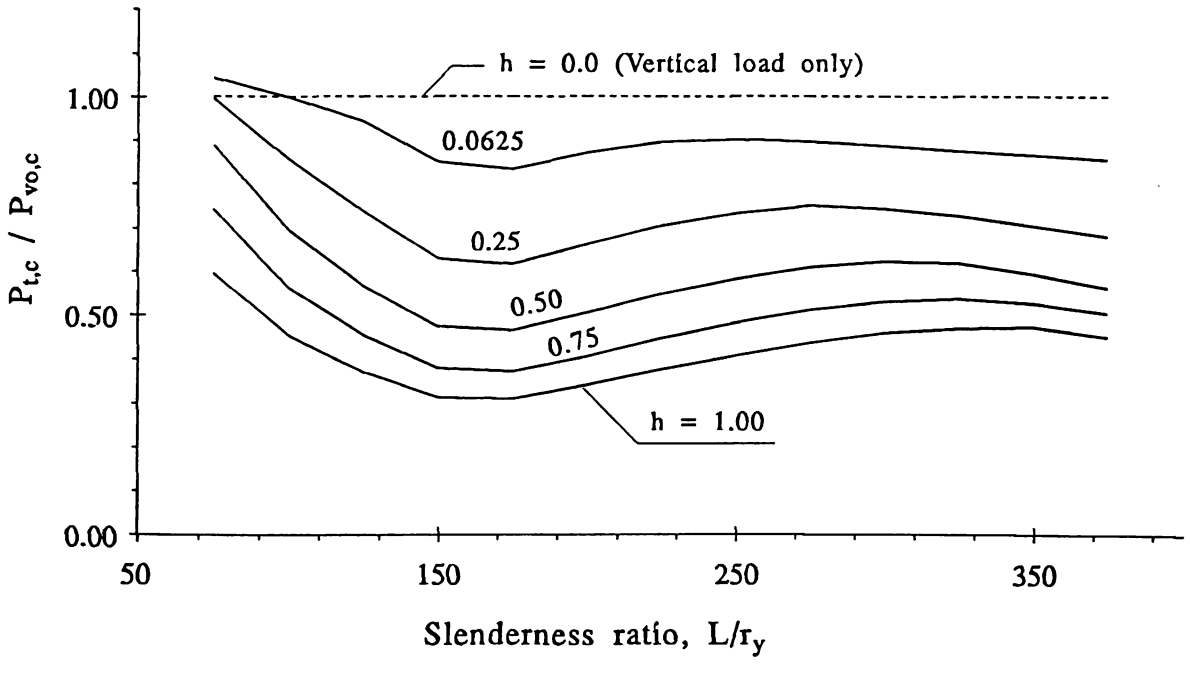

(b) Total load normalized to $P_{vo,c}$.

Figure 4-7 Variation with L/r_y of the combined ultimate load of two-hinged arch under vertical and longitudinal loading.

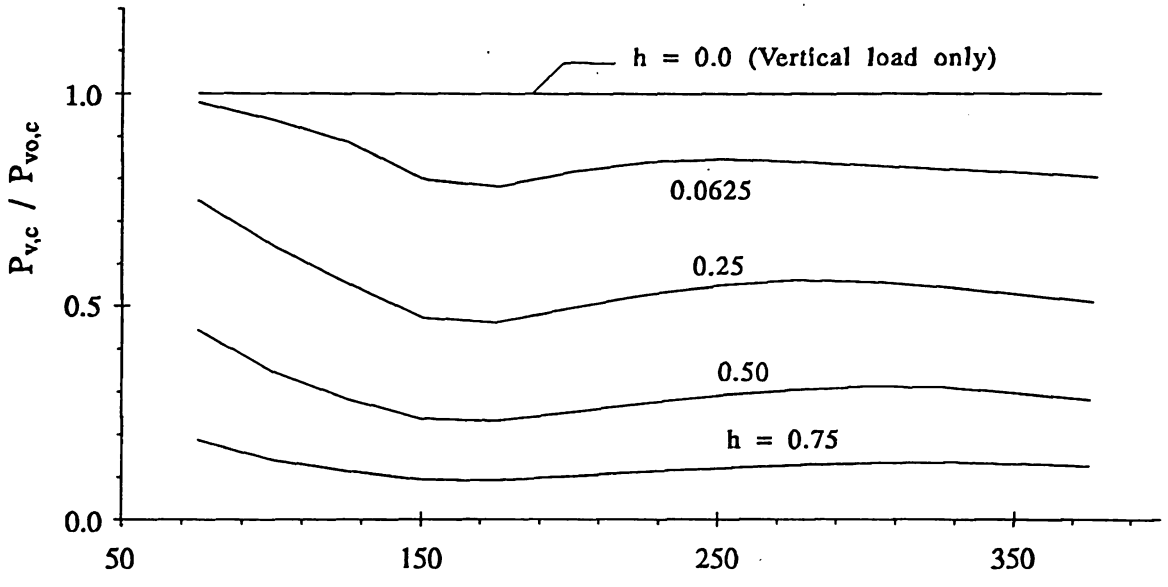

(c) Vertical component normalized to $P_{vo,c}$.

Figure 4-7 continued.

Figure (4-7.c) shows the vertical component of the total combined ultimate load normalized to $P_{vo,c}$, which follows the same trends as the total load, but with less fluctuation. This figure represents the actual reduction in the arch vertical ultimate load due to presence of longitudinal load. For example, for h = 0.25 (where longitudinal load = 0.33 of vertical load), the arch vertical load capacity ranges from 50% to 75% of its capacity under vertical-only load, $P_{vo,c}$, while for h = 0.50 (where longitudinal load = vertical load) the arch capacity ranges from 25% to 47% of $P_{vo,c}$.

To more clearly show the effect of combining both geometric and elastic nonlinearities on the arch ultimate load, the elastic and combined loads for each value of h, $P_{t,e}(h)$ and $P_{t,c}(h)$, were normalized to the plastic load for that value,

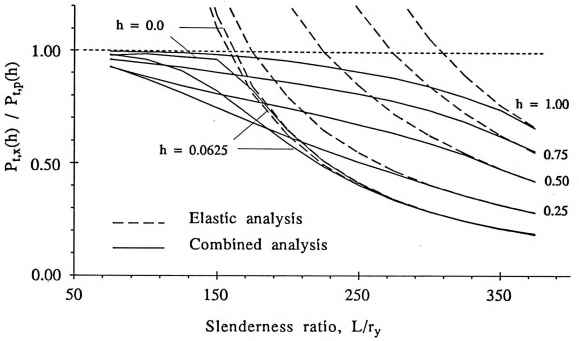

Figure 4-8 Elastic and combined ultimate loads of two-hinged arch under vertical and longitudinal loading normalized to corresponding plastic ultimate loads of same value of h.

$P_{t,p}(h)$ in Figure (4-8). From this figure it is seen that in the range where plastic load governs, the combined ultimate load has the smallest reduction from plastic ultimate load for h = 0.0 and 1.0, while it is most significant for h = 0.25. The latter ratio is where the direction of the total load resultant on the left half of the arch span is approximately perpendicular to the chord extending from the arch support to its crown; such loading case would be the most effective in producing unsymmetric deflection mode.

For high L/r_y the curves follow the elastic behavior where the reduction is largest for h = 0.0 and smallest for h = 1.0. In addition, as h increases, the point of intersection of the elastic curves with the plastic curves (represented

by the horizontal dashed line) shifts to the right along the L/r_y axis, in effect extending the range of significance for combined effect.

4.3.2 Variation of The Ultimate Load of Two-Hinged Arch with the Ratio of Longitudinal Load to Total Load

The effect of the change in the ratio of longitudinal load to total load, h, on the arch total load carrying capacity is shown in Figure (4-9). The effect of the value of h on the "vertical component" of the arch load carrying capacity is presented later in this chapter when the arch behavior under unsymmetric vertical load is discussed.

Figure (4-9.a) shows the variation with h of the plastic ultimate load, $P_{t,p}$, (normalized to $P_{vo,p}$) for different values of L/r_y. For $L/r_y = 75$, the relation begins with a slight increase in ultimate load to 108% of $P_{vo,p}$ as h increases from 0.0 to 0.25, then decreases to a low of 60% of $P_{vo,p}$ as h increases from 0.25 to 1.0. For higher L/r_y, the protrusion disappears and the ultimate load decreases with h for its entire range to a minimum of 12% for $h = 1.0$ and $L/r_y = 375$. However, the rate of decrease of ultimate load becomes smaller as L/r_y increases.

Figure (4-9.b) shows the variation with h of the elastic ultimate load, $P_{t,e}$, normalized to $P_{vo,e}$, for different values of L/r_y. For $L/r_y = 75$, the ultimate load increases with h for its entire range, with accelerating rate of increase as h increases to reach 400% of $P_{vo,e}$ for $h = 1.0$. As L/r_y increases, the sharp increase of individual curves with h rapidly changes to a decrease

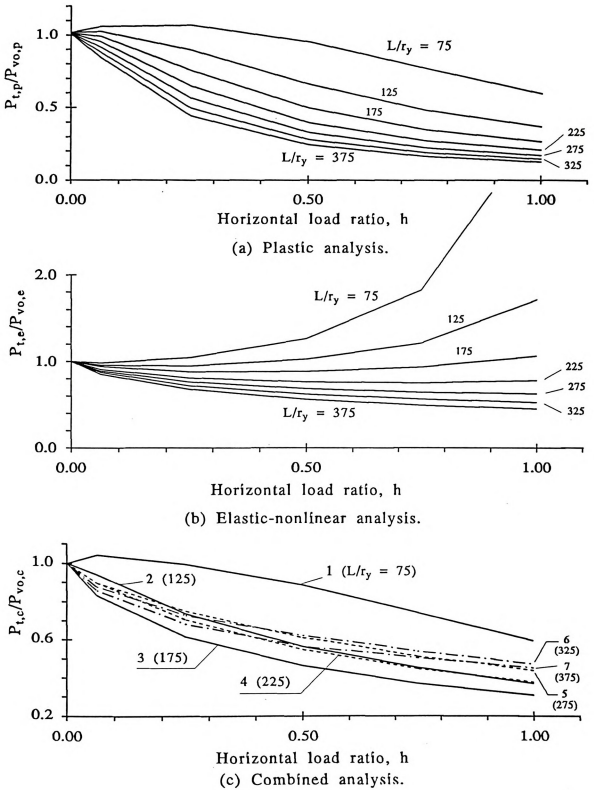

Figure 4-9 Variation of the plastic, elastic, and combined ultimate loads of two-hinged arch with h for different values of L/r_y.

over the entire range of h, with the decrease reaching 50% for $L/r_y = 375$. The sharp increase with h may be related to the ratio of the arch longitudinal to vertical stiffness, which is higher than unity for low L/r_y and less than unity for high L/r_y. For a given value of h, the rate of decrease of the ultimate load becomes smaller as L/r_y increases.

Figure (4-9.c) shows the variation with h of the combined ultimate load, $P_{t,c}$, normalized to $P_{vo,c}$ for different values of L/r_y, where the curves exhibit the same phenomenon of being similar to plastic curves for lower L/r_y and then shifting to the elastic curves as L/r_y increases. The first three curves decrease gradually following plastic ones, then the second two (marked by dashed lines) increase marking the region of transition. Finally, the last two curves (marked by dash-dotted lines) decrease again similar to elastic curves. It is noteworthy that most of the curves are banded closely together; for h = 0.5 (where vertical and longitudinal loads are equal), five of the seven curves are enclosed by the limits of 65% and 55%.

4.3.3 Ultimate Load Interaction Curves of Two-Hinged Arch

Figure (4-10) shows three sets of interaction curves between the vertical and longitudinal components of the total load for different values of slenderness ratio ($L/r_y = 125$, 225, and 325). For each set the vertical and longitudinal components of the ultimate load from plastic, elastic, and combined analyses, $P_{v,x}$ and $P_{h,x}$, are normalized first to the plastic vertical-only and longitudinal-only ultimate loads, $P_{vo,p}$ and $P_{ho,p}$, respectively (figures on left), then to their

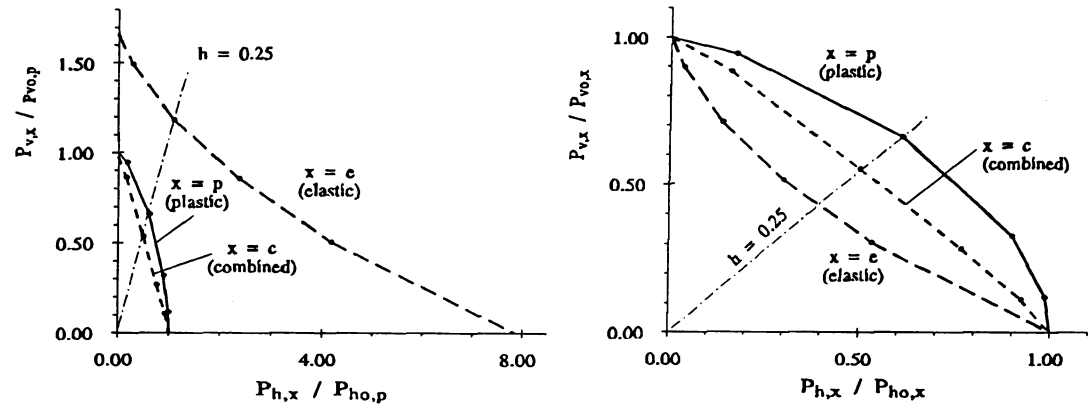

(a) stiff arch, L/r_y = 125. h = 0.25

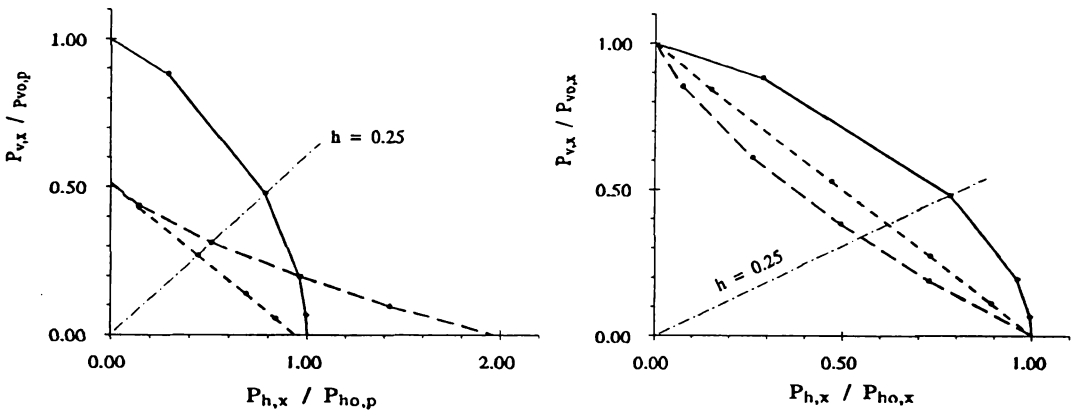

(b) medium arch, L/r_y = 225.

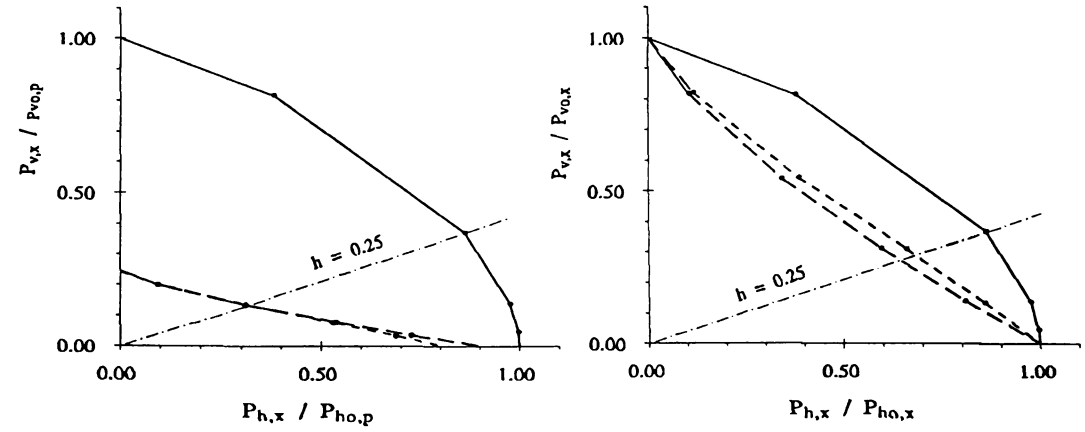

(c) slender arch, L/r_y = 325.

Figure 4-10 Interaction curves between vertical and longitudinal loading of two-hinged arch for different values of L/r_y.

corresponding vertical-only and longitudinal-only ultimate loads, $P_{vo,x}$ and $P_{ho,x}$ (figure on right). The suffix "x" represents type of analysis where x = p for plastic (for example, $P_{v,p}/P_{vo,p}$), e for elastic, or c for combined.

The figures on left show the relative values of elastic and combined ultimate loads compared to plastic ultimate loads for different values of L/r_y. For a given value of L/r_y, of the ratio of elastic ultimate load to plastic one for vertical-only load, $P_{vo,e}/P_{vo,p}$, is always smaller than the corresponding ratio for longitudinal-only loading, $P_{ho,e}/P_{ho,p}$. This is also obvious in Figure (4-8). The effect of this difference on the interaction curves for combined analysis (which is basically a lower envelope for the other two curves) is evident for L/r_y = 225 where elastic behavior controls the vertical-only loading while plastic behavior controls longitudinal-only loading, resulting in a significant reduction in the combined ultimate load for intermediate values of h compared to either plastic or elastic ones.

The figures on right show that the shape of the interaction curve for plastic and elastic analyses are essentially independent of L/r_y: convex for plastic analysis and concave for elastic analysis. Nonetheless, as L/r_y increases, the location on the interaction curve of the point corresponding to a given value of h shifts from the vertical axis toward the horizontal axis. For example, for h = 0.25, the value of $P_{v,p}/P_{vo,p}$ decreases while $P_{h,p}/P_{ho,p}$ increases with L/r_y, as shown in the figure.This is attributed to the decrease in the ratio of $P_{ho,p}/P_{vo,p}$ as L/r_y increases. This behavior is also true for elastic and combined analysis. For

combined analysis, the interaction curves shift from convex form for low L/r_y values, where it is closer to that of plastic analysis, to concave form -similar to the elastic curve- for higher values of L/r_y.

4.3.4 Failure Modes and Response Curves of Two-Hinged Arch

The deflected shape of two-hinged arch at the ultimate load (or failure modes) for different types of analysis and values of h are shown in Figure (4-11) for $L/r_y = 125$, and in Figure (4-12) for $L/r_y = 225$. The deflection is magnified by a factor of 5 for plastic and combined loading for clarity.

In both figures, the apparent symmetric (or almost symmetric) failure modes of plastic curves under vertical loading ($h = 0.0$) indicate the arch failure is due to thrust action at the support. This is confirmed by the curve discontinuity near the left arch support due to plastic hinge formation. The only other symmetric failure mode is that of stiff arch for combined analysis under vertical loading, where geometric effects are negligible. For $h > 0.0$, the failure modes are unsymmetric and smooth for all other cases. For elastic curves, the deflection magnitudes show a clear gradual increase with h, but for other types of analysis the curves are inseparable and overlapped. It is important to mention here that for all studied cases, the apparent symmetric failure modes at the ultimate load change to unsymmetric modes when the analysis is continued past the ultimate load point (using displacement-controlled analysis, as explained in chapter 3).

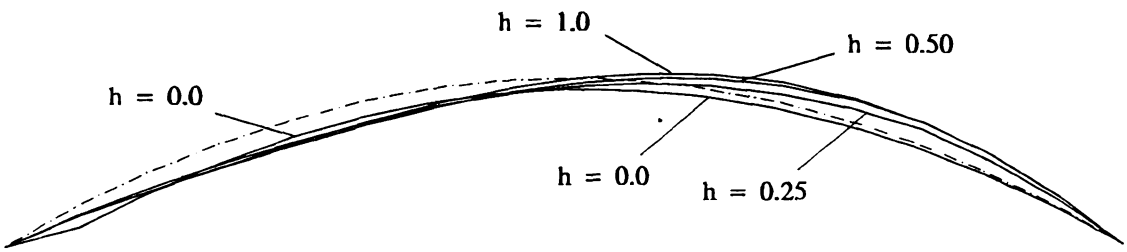

Deflection Magnification Factor, DMF = 5

(a) Deflected shape under plastic analysis.

DMF = 5

(b) Deflected shape under combined analysis.

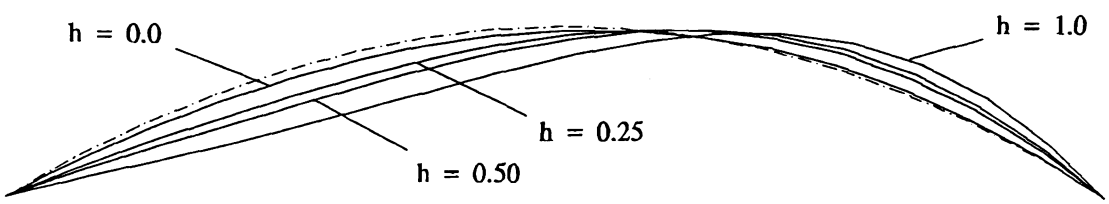

DMF = 1

(c) Deflected shape under elastic analysis.

Figure 4-11 Deflected shapes of two-hinged stiff arch (L/r_y = 125) at ultimate load for different types of analysis and values of h.

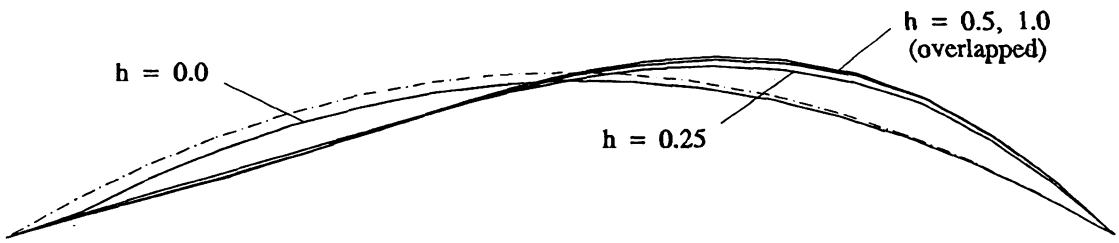

DMF = 5

(a) Deflected shape under plastic analysis.

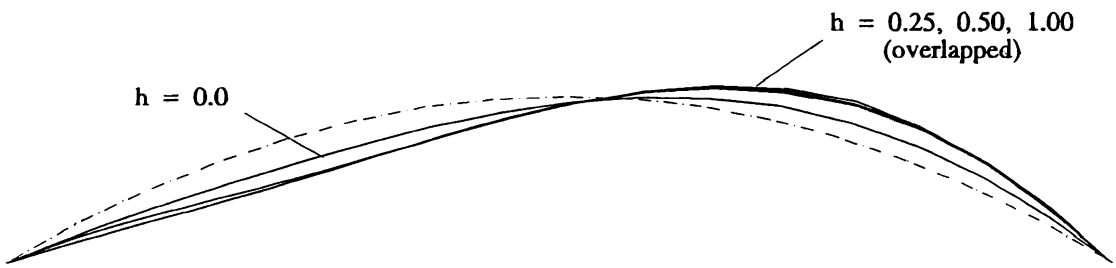

DMF = 5

(b) Deflected shape under combined analysis.

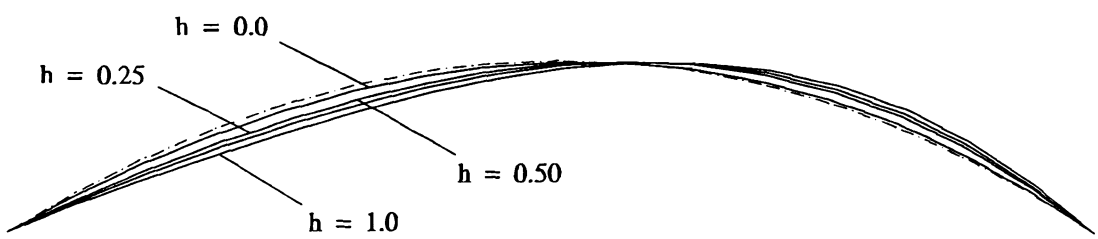

DMF = 1

(c) Deflected shape under elastic analysis.

Figure 4-12 Deflected shapes of two-hinged medium arch (L/r_y = 225) at ultimate load for different types of analysis and values of h.

Comparison of the two figures reveals that the deflection at ultimate load increases modestly with L/r_y for plastic and combined analysis, where the arch flexibility more than compensates for the lower ultimate load. For elastic analysis, it decreases notably, since the ultimate load decreases more rapidly. Within each figure, the deflection at ultimate load for elastic analysis is larger than that of plastic or combined analysis, since geometric effects tend to propagate deflections for elastic analysis while plastic hinge formation forces premature failure for the latter two cases.

Figure (4-13) shows the vertical and longitudinal displacement response curves at the quarter point of a medium arch ($L/r_y = 225$) for different values of h, under combined analysis where it shows the influence of plastic and geometric effects on displacement. As the arch is loaded, the response curves for combined and elastic analysis are initially the same. If the plastic ultimate load is significantly larger than the elastic one, the elastic and combined curves follow the same path, as shown in Figures (4-13.a). But if the plastic ultimate load is close to or less than the elastic ultimate load, yielding occurs in the arch (at some joint). This causes the combined curve to separate from the elastic curve and follow a path similar or lower than that of plastic analysis, and reach its combined ultimate load prematurely, Figure (4-13.b and c).

From the figure, the initial slope of the curves decreases drastically with h; for example the initial slope under longitudinal-only load is about 5% that for vertical-only load. The ratio of maximum vertical to longitudinal

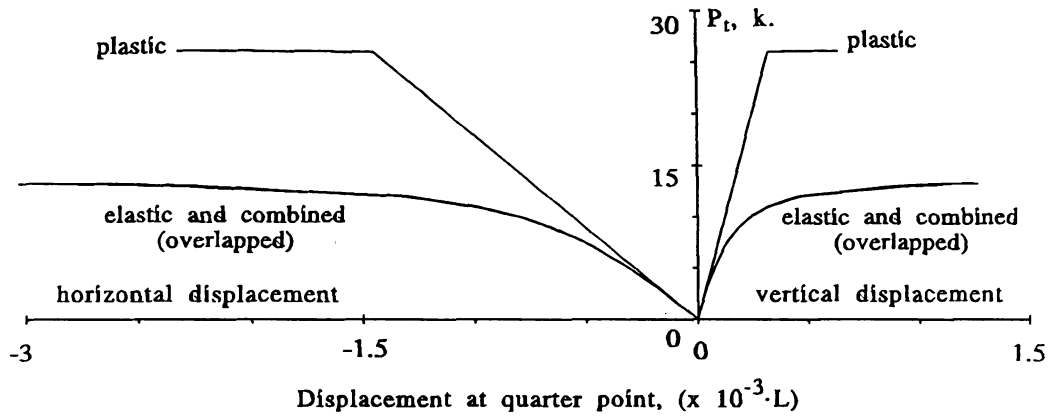

(a) Response under vertical load (h = 0.0).

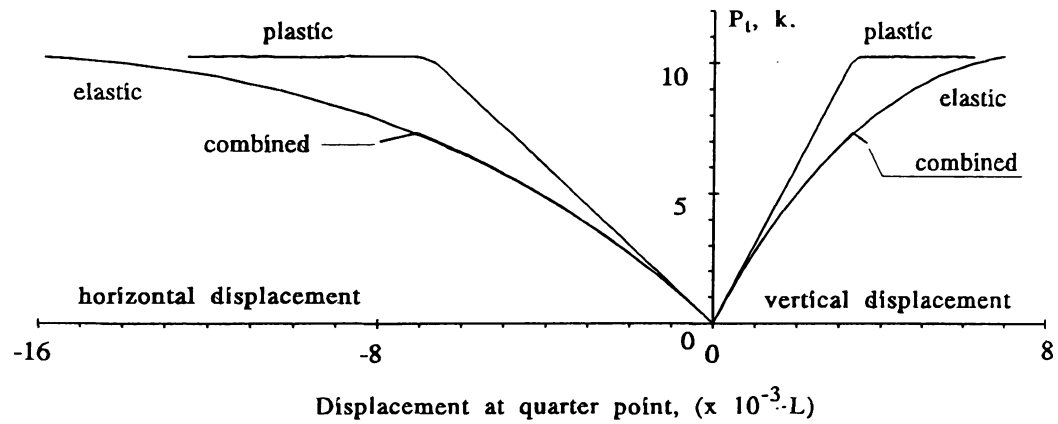

(b) Response under vertical and horizontal load (h = 0.5).

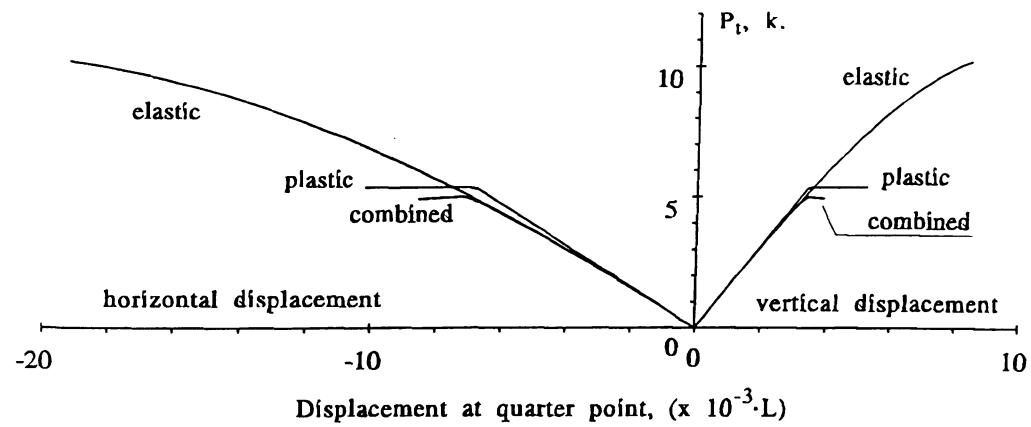

(c) response under horizontal load (h = 1.0).

Figure 4-13 Displacement response curves at quarter point of medium two-hinged arch (L/r_y = 225) for different values of h.

components of the plastic displacement is essentially the same for values of $h > 0.0$ (about 1.6) but is much larger for $h = 0.0$ (about 3.3). The corresponding ratios for elastic and combined displacements remain the same for all values of h (about 2.3).

4.3.5 Plastic Hinge Formation and Force Path at Quarter Point of Two-Hinged arch

Table (4-1) shows the order of plastic hinge formation with the progress of loading in two-hinged arch ($L/r_y = 225$) for different values of h due to plastic and combined analysis. Figure (4-14) shows the force path at the left quarter point (node #5, at the right end of member #4, see Figure (4-1)), where the relation between axial force and bending moment is traced until failure.

For $h = 0.0$, the plastic force path follows a path that is close to the N-axis, suggesting axial load-dominated behavior. In addition, the development of plastic hinge near the left support causes moment release and further shift toward the P-axis. On the other hand, the combined curve exhibits a significant divergence from the plastic one and a shift toward the M-axis with increase of loading, demonstrating the effect of elastic nonlinearity which generates moment in the arch. Failure under combined analysis occurs without formation of any plastic hinge in the arch.

With the increase of h from 0.0 to 0.25, the force path for plastic analysis shifts notably toward the M-axis and the axial force at failure decreases. Also, as h increases the position of the plastic hinge formation

Table 4-1 Plastic hinge formation in hinged arch for different types of analysis under different load combinations.

h	Plastic Analysis			Combined Analysis		
	Member: Joint	P at Yield	Yield Status*	Member: Joint	P at yield	Yield Status
0.00	$P_{t,p}$ = 26.11			$P_{t,c}$ = 13.39		
	1:2	26.00	Y	none	-	-
0.0625	$P_{t,p}$ = 24.59			$P_{t,c}$ = 12.00		
	15:1	24.40	Y	4:2	12.00	Y
	3:2	24.58	Y			
0.25	$P_{t,p}$ = 16.74			$P_{t,c}$ = 9.42		
	14:1	16.01	Y	14:1	9.42	Y
	4:2	16.74	Y			
	5:1	16.74	Y			
0.50	$P_{t,p}$ = 10.26			$P_{t,c}$ = 7.32		
	14:1	10.00	Y	14:1	7.32	Y
	4:1	10.26	Y			
0.75	$P_{t,p}$ = 7.09			$P_{t,c}$ = 5.96		
	14:1	7.00	Y	14:1	5.96	Y
	3:2	7.08	Y			
	4:1	7.08	Y			
1.00	$P_{t,p}$ = 5.35			$P_{t,c}$ = 5.01		
	3:2	5.34	Y	14:1	4.81	Y
	14:1	5.34	Y	13:2	4.82	Y

* Y = joint yields, U = joint unloads.

moves along the arch axis from the left support toward the crown until it reaches the quarter point for h = 0.25. In addition, another hinge forms near the right quarter point briefly before the left hinge formation. For combined analysis, the divergence of the force path from that of plastic analysis is less significant since moment is generated in the arch in both cases. Only one

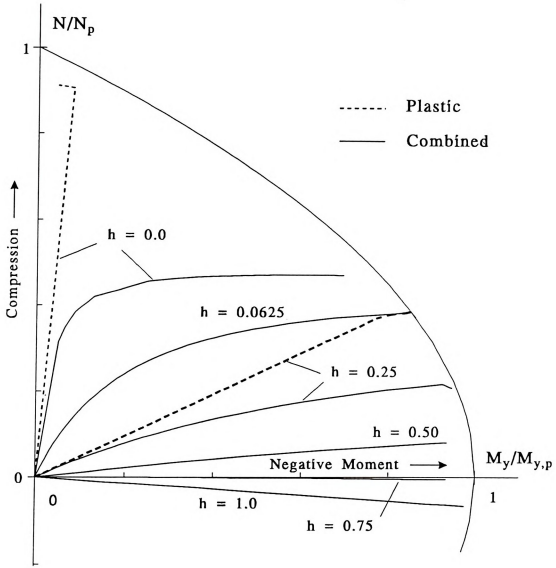

Figure 4-14 Relation between axial force and bending moment at the left quarter point of hinged-arch ($L/r_y = 225$).

plastic hinge forms in the arch at the ultimate load causing instability of the arch; this hinge forms at the left quarter point for h = 0.0625 while it jumps to the right side for h = 0.25.

As h increases beyond 0.25, the trend of decreasing axial force continues where it gradually changes from compression to tension as h increases to 1.0. Since the magnitude of axial force is small in this range, the difference between plastic and combined curves becomes negligible. The position of the plastic hinge that forms in the right half remains unchanged for both plastic and combined cases, while that forming in the left, which forms during plastic analysis only, slightly shifts back toward the support.

4.4 BEHAVIOR OF FIXED ARCH UNDER VERTICAL AND LONGITUDINAL LOADING

The behavior of fixed arch was studied using the same arch geometry, section properties, and loading combinations. The effect of fixing the arch supports increases the arch ultimate load, although the observed trends are similar to those of two-hinged arch. In this section, the obtained results are presented, with emphasis on the differences from those of two-hinged arch.

4.4.1 Variation of the Ultimate Load of Fixed Arch with Slenderness Ratio

The plastic, elastic-nonlinear, and combined ultimate loads of the fixed arch were obtained for the same values of L/r_y and h used for two-hinged arch. The results are presented in the following subsections.

4.4.1.1 Plastic Ultimate Load of Fixed Arch

Figure (4-15.a) shows the variation with L/r_y of the plastic ultimate load of fixed arch, $F_{t,p}$, normalized to $P_{vo,p}$ (the vertical-only ultimate load of two-

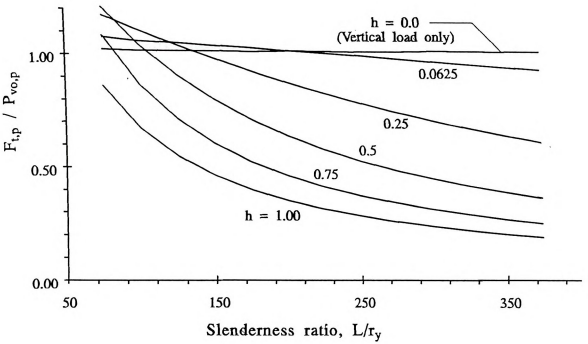

(a) Total load normalized to $P_{vo,p}$ ($P_{vo,p}$ = $F_{vo,p}$).

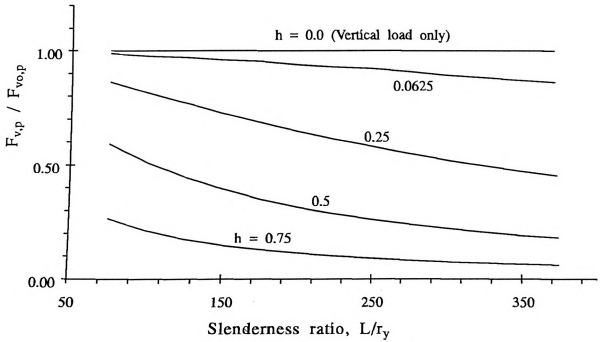

(b) Vertical component normalized to $F_{vo,p}$.

Figure 4-15 Variation with L/r_y of the plastic ultimate load of fixed arch under combined vertical and longitudinal loading.

hinged arch). From this figure, it is seen that the vertical-only ultimate load of fixed arch is practically equal to that of two-hinged arch, i.e., $F_{vo,p} \approx P_{vo,p}$. For other curves of $h > 0.0$, the general trend is similar to that of two-hinged arch, Figure (4-5.a), with comparable degree of nonlinearity. However, the total ultimate load of fixed arch for given values of h and L/r_y is always larger than the corresponding total ultimate load of two-hinged arch. Figure (4-15.b) shows the vertical component of the ultimate load, $F_{v,p}$, normalized to $F_{vo,p}$, where the same trends of total load are also true.

Table (4-2) presents the increase in the ultimate loads due to fixing the arch supports in percentage form for selected values of h and L/r_y for plastic, elastic, and combined analysis. The values in the table also apply to the comparison of the vertical components of the ultimate loads of fixed and two-hinged arches since the loading is proportional and the scaling factors are the same in both cases for each entry. From the table it is obvious that for constant values of L/r_y, the increase in plastic ultimate load due to fixing the arch supports becomes larger as h increases. For stiff arches this increase is gradual over the range of h, while for slender arches it is unevenly concentrated in the range from $h = 0.0$ to 0.5.

Viewing the same data for constant values of h, the gain in plastic ultimate load is largest for longitudinal-only loading, with the gain being constant with L/r_y for $h = 0.0$ (with no gain from the two-hinged case), and $h = 1.0$ (where the gain ranges from 49% to 52%). For $h = 0.25$ and 0.50, the

Table 4-2 Relative Increase of fixed arch ultimate load in comparison with two-hinged arch for different types of analysis and values of longitudinal load ratio, h.

Type of analysis	h	$F_{t,x}(h)/P_{t,x}(h)$, %		
		$L/r_y = 125$	$L/r_y = 225$	$L/r_y = 325$
Plastic	0.00	0.00	0.19	0.56
	0.25	16.33	27.78	35.00
	0.50	37.35	45.42	48.49
	1.00	49.22	51.29	51.85
Elastic-nonlinear	0.00	113.73	117.78	119.76
	0.25	137.56	154.31	163.32
	0.50	161.83	187.86	201.31
	1.00	561.84	317.46	304.69
combined	0.00	0.78	76.62	120.71
	0.25	26.72	47.56	95.56
	0.50	41.40	50.27	68.24
	1.00	50.23	58.43	74.39

gain gradually increases with L/r_y between the limits of the other above-mentioned two cases.

4.4.1.2 Elastic-Nonlinear Ultimate Load of Fixed Arch

The elastic-nonlinear ultimate load of fixed arch, $F_{t,e}$, is shown in Figure (4-16.a) normalized to $P_{vo,p}$, and Figure (4-16.b and c) normalized to $P_{vo,e}$ and $F_{vo,e}$, respectively. It is seen from the first figure that the main effect of fixing the arch support is to significantly shift the critical slenderness ratio, $L/r_{y)cr}$ to

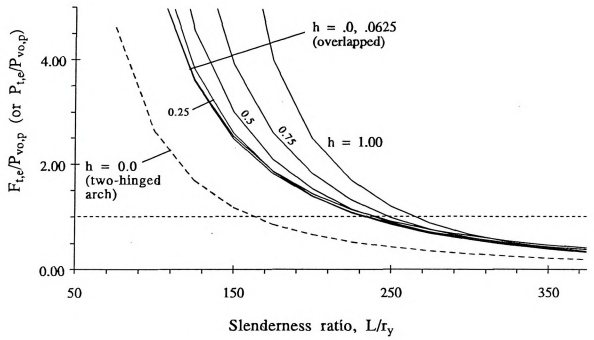

(a) Total load normalized to $P_{vo,p}$.

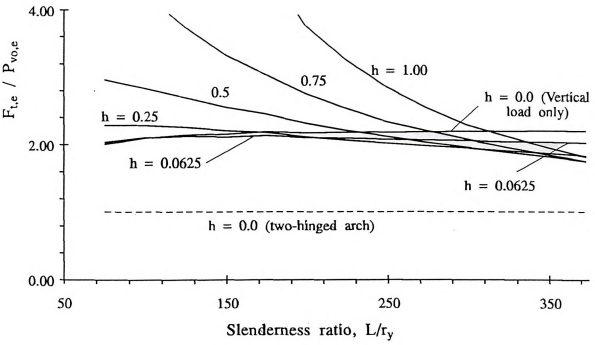

(b) Total load normalized to $P_{vo,e}$.

Figure 4-16 Variation with L/r_y of the elastic ultimate load of fixed arch under vertical and longitudinal loading.

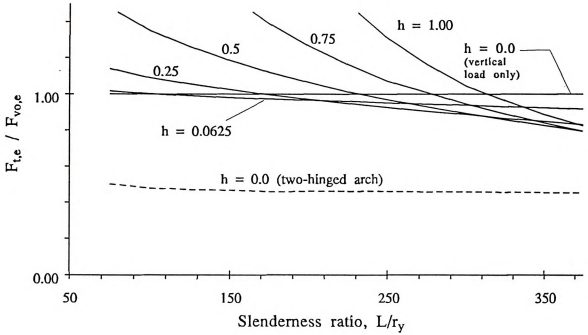

(c) Total load normalized to $F_{vo,e}$.

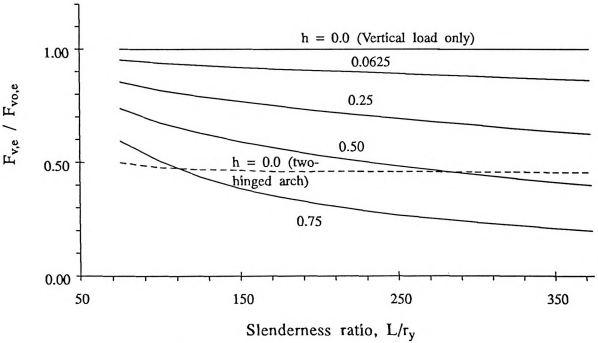

(d) Vertical component normalized to $F_{vo,e}$.

Figure (4-16) continued.

the right (where $F_{vo,p} = F_{vo,e}$ at $L/r_{y)cr} = 240$, compared with $L/r_{y)cr} = 165$ for two-hinged arch), extending the range where plastic behavior dominates. Also, the nonlinearity of the curves increases with h, with the difference between the curves becoming more significant as L/r_y decreases.

The second and third figures show that for the studied range of L/r_y, the lower envelope for the curves of total elastic ultimate load exhibits a gain of at least 80% (for h = 0.50 and $L/r_y = 375$) compared to $P_{vo,e}$. For h = 0.0, the ratio of $F_{vo,e}/P_{vo,e}$ is roughly constant with the gain in ultimate load about 114% to 120%. As h increases, the curves shift mainly to the right along the L/r_y axis, with smaller shift down. The curves of h = 0.0 and h = 1.0 intersect (i.e., $F_{ho,e} = F_{vo,e}$) at $L/r_y = 310$; in comparison, for two-hinged arch, $P_{vo,e} = P_{ho,e}$ at $L/r_y = 185$.

The decrease in the vertical component of the elastic-nonlinear ultimate load, $F_{v,e}$, Figure (4-16.d), exhibits similar trend to that of two-hinged arch, but again the rate of decrease with both h and L/r_y is smaller. For example, vertical load component of fixed arch for h = 0.5 (where longitudinal load is equal to the vertical load) is larger than the vertical-only ultimate load of two-hinged arch, $P_{vo,e}$, for most of the L/r_y range.

Table (4-2) shows that for constant values of h, the gain in elastic-nonlinear ultimate load of fixed arch compared to corresponding two-hinged case is at least 114% (for h = 0.0 and $L/r_y = 125$), and reaches up to 560% (for h = 1.0 and $L/r_y = 125$). This drastic gain is attributed to the increased

nonlinearity of the curves of fixed arch with the increase of h, coupled with the shift of all the curves of fixed arch along L/r_y axis compared with those two-hinged curves. Because of the combination of these two factors, the gain in ultimate load with L/r_y is not uniform, where it is constant for h = 0.0, and increases for h = 0.25 and 0.50, but decreases for h = 1.0.

4.4.1.3 Combined Ultimate Load of Fixed Arch

The combined ultimate load of fixed arch is shown in Figure (4-17.a and b) normalized to $P_{vo,p}$, and $P_{vo,c}$, respectively. From the first figure, the expansion of the plastic range in comparison with two-hinged arch is obvious. Otherwise, the figure exhibits the same aspects of behavior as those of two-hinged arch, but with smaller decrease of ultimate load for the same value of h and L/r_y.

The second figure shows the effect of fixing the arch supports on its ultimate load as compared to two-hinged arch, Figure (4-7.b). Similar to plastic analysis, the gain is modest for low L/r_y, while it is significant for high L/r_y, coinciding with elastic analysis. The region of transition from the plastic- to elastic-dominated regions may be roughly defined by the two values of the critical slenderness ratio for two-hinged and fixed arch, $L/r_{y)cr}$ = 165 and 240.

Figure (4-17.c and d) show the total and vertical component of the combined ultimate loads, respectively, normalized to $F_{vo,c}$. These figures reflect the change in the ultimate load and its vertical component of fixed arch due to the presence of longitudinal load, where they show similar behavior to that of

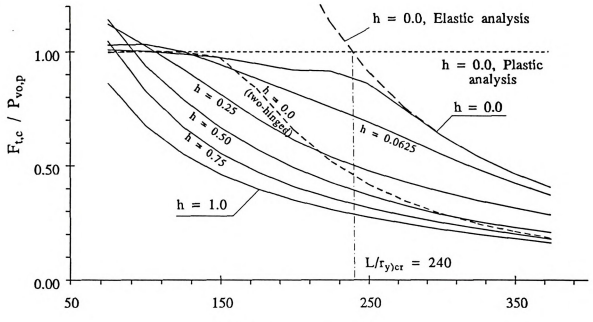

(a) Total load normalized to $P_{vo,p}$.

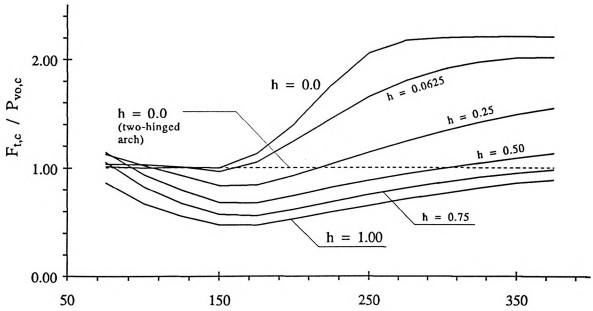

(b) Total load normalized to $P_{vo,c}$.

Figure 4-17 Variation with L/r_y of the combined ultimate load of fixed arch under vertical and longitudinal loading.

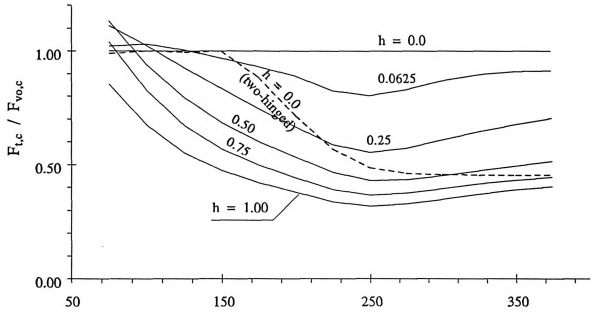

(c) Total load normalized to $F_{vo,c}$.

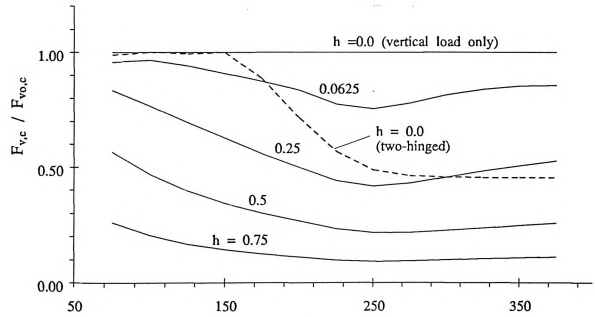

(d) Vertical component normalized to $F_{vo,c}$.

Figure (4-17) continued.

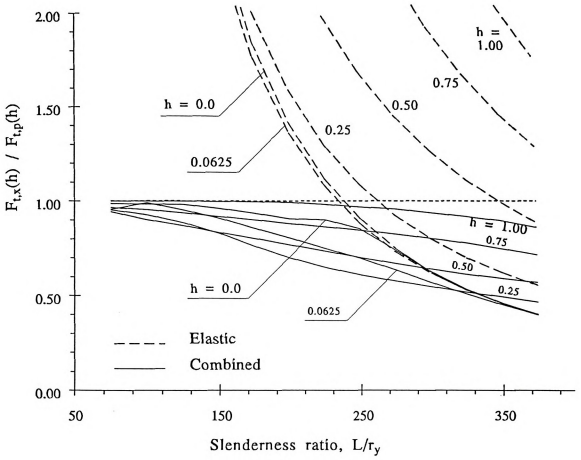

Figure 4-18 Elastic and combined ultimate loads of fixed arch under vertical and longitudinal load normalized to corresponding plastic loads of the same value of h.

two-hinged arch, but with slower decrease with h and the middle plunge (due to transition from plastic- to elastic-dominated behavior) being shifted to the right.

Figure (4-18), shows the combined and elastic ultimate loads for a given h normalized to the plastic ultimate load of the same h. Similar to two-hinged case, it shows the most decrease in ultimate load -due to combining plastic and geometric effects- is for h = 0.25 and 0.5. Measuring the decrease for a given value of h as that at the point when $F_{t,e} = F_{t,p}$, it is seen that the decrease in the

case of fixed arch is slightly larger than that of two-hinged arch; for example, the respective values for h = 0.25 are 40% and 30%.

The gain in combined ultimate load of fixed arch compared with that of two-hinged arch is shown in Table (4-2). It is seen that for constant h the gain in ultimate load always increases with L/r_y, although the rate of this gain levels out as h increases. This is attributed to the change from plastic- to elastic-dominated behavior, which occurs at different stages for fixed and two-hinged cases (i.e., $L/r_{y)cr}$ is different for fixed and two-hinged arches). Also, for each case this change is not synchronized with L/r_y (i.e., the value of L/r_y where $F_{t,e}(h) = F_{t,p}(h)$ is not the same for all values of h, as clearly seen from Figure (4-18)).

The combination of these two factors produces the fluctuating values of the gain in ultimate load with h for constant L/r_y. For example, the gain in ultimate load for the same value of $L/r_y = 325$ changes from 121% for h = 0.0 (where it is equal to that of elastic analysis), to 74% for h = 1.0 (which is closer to that of plastic analysis). For h = 0.25, the gain is 95%, which is in the middle between the corresponding plastic (35%) and elastic (163%) values. For h = 0.5, the gain is 68%, which is the lowest value for $L/r_y = 325$.

4.4.2 Variation of The Ultimate Load of Fixed Arch with the Ratio of Longitudinal to Total Load

The variation with h of the plastic ultimate load of fixed arch is shown in Figure (4-19.a) normalized to $F_{vo,p}$, where it is similar to that of two-hinged

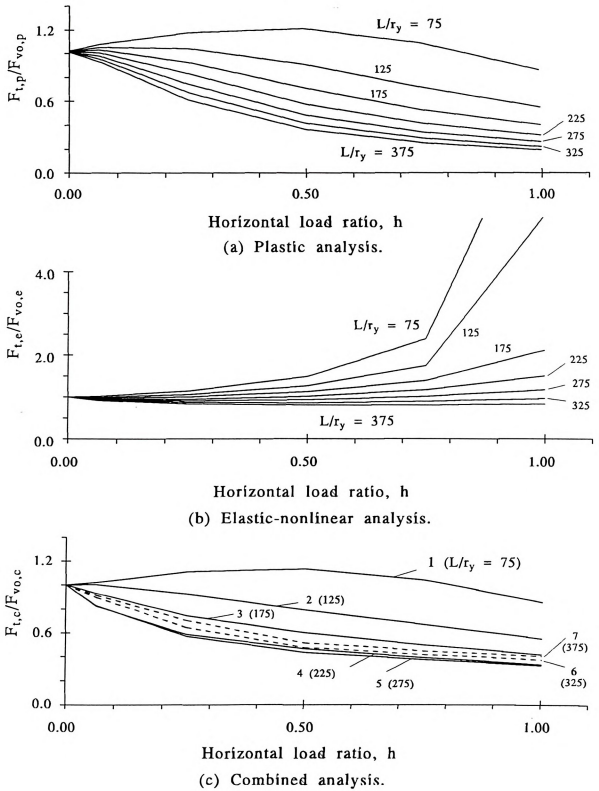

Figure 4-19 Variation of the plastic, elastic, and combined ultimate loads of fixed arch with h for different values of L/r_y.

arch, but with slower decrease with h for all curves. In particular, for L/r_y = 75 the increase with h of the normalized ultimate load continues from 0.0 to 0.50 where it peaks at 120% then decreases to 60% for h = 1.0. The lowest ultimate load ratio of 20% occurs for h = 1.0 and L/r_y = 375.

The elastic ultimate loads of fixed arch are shown in Figure (4-19.b) normalized to $F_{vo,e}$. The variation with h is similar to that of two-hinged arch, but with slight shift up for all curves, where the ultimate load reaches a minimum of 50% of $F_{vo,e}$ for h = 1.0 and L/r_y = 375.

The variation of combined ultimate load of fixed arch with h normalized to $F_{vo,c}$, Figure (4-19.c), shows a slight partial increase with h for L/r_y = 75 -similar to plastic curves- while it decreases with h for other curves of L/r_y. The rate of decrease gradually becomes smaller with L/r_y until the ultimate load bottoms out around L/r_y = 275 and begins to increase again for the rest of the range, indicating the shift from plastic to elastic behavior. The last stage of decreasing again to coincide with elastic curves -exhibited by two-hinged arch- is not present here, since it occurs outside the studied range of L/r_y. Compared to Figure (4-9), the figure also shows similar but wider banding of the curves.

4.4.3 Ultimate Load Interaction Curves of Fixed Arch

The general trends of the interaction curves for fixed arch, Figure (4-20), are similar to those of two-hinged arch, where the plastic interaction curves are convex, elastic curves are concave with higher nonlinearity for low L/r_y, and combined curves change with L/r_y from the plastic to elastic ones.

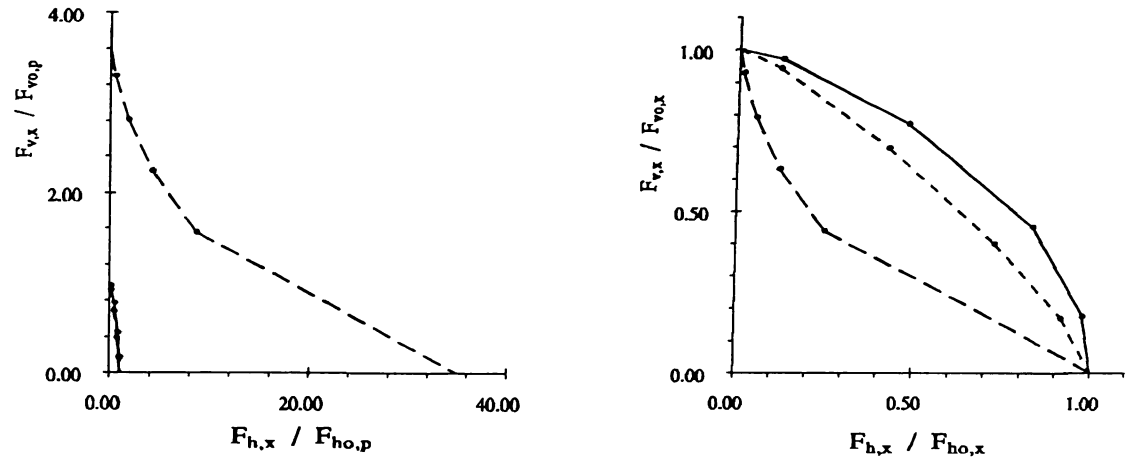

(a) stiff arch, $L/r_y = 125$.

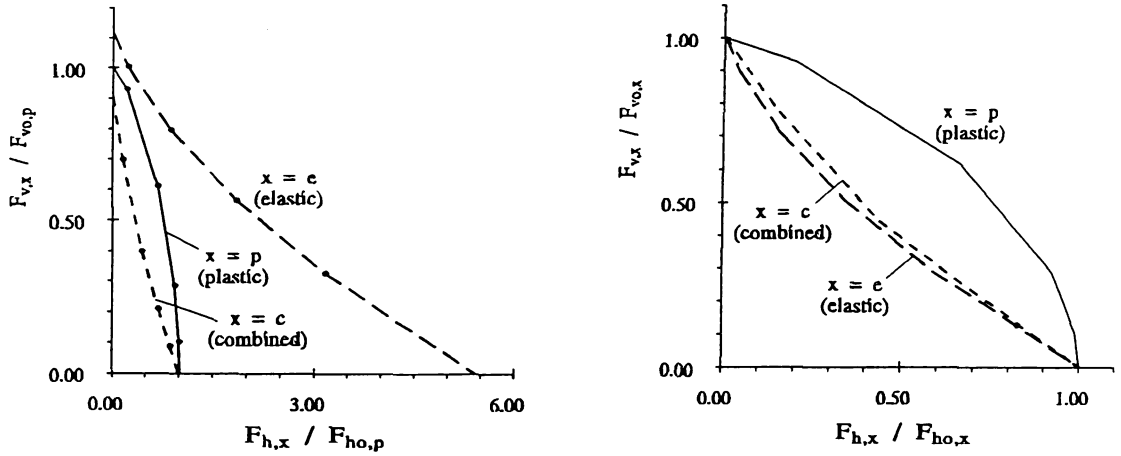

(b) medium arch, $L/r_y = 225$.

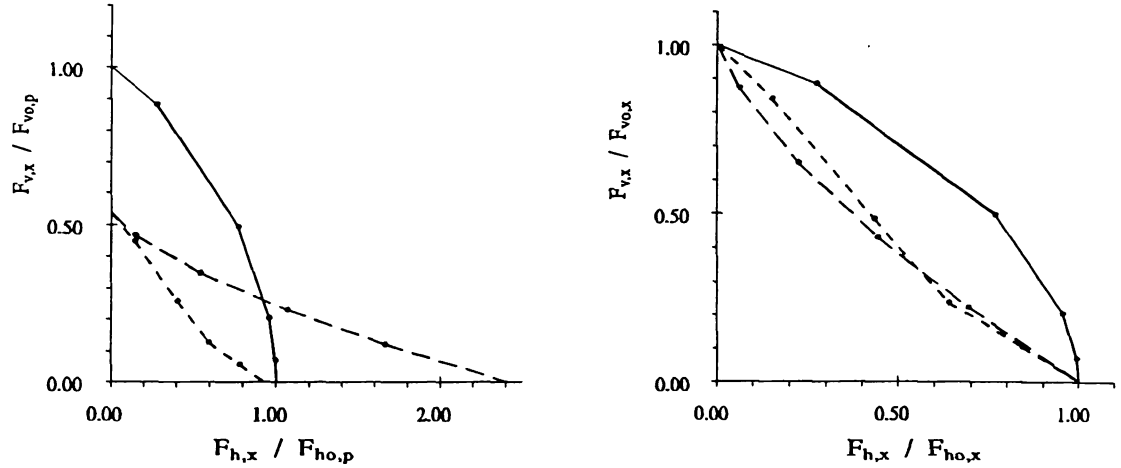

(c) slender arch, $L/r_y = 325$.

Figure 4-20 Interaction curve between vertical and longitudinal loading of fixed arch for different values of L/r_y.

For the first case of $L/r_y = 125$, Figure (4-20.a), the curves to the right in the figure (normalized to $F_{vo,p}$ and $F_{ho,p}$) show that the elastic ultimate load for vertical-only loading is about 3.5 times its plastic ultimate load (compared to 1.6 for hinged arch). For longitudinal-only loading the corresponding ratio is 36 (compared to 8 for hinged arch), with ten fold increase from that of vertical-only loading.

The three figures on left show that plastic behavior controls the combined behavior for $h = 1.0$ for the whole range of L/r_y. For $h = 0.0$, plastic behavior controls only the first case ($L/r_y = 125$), while elastic behavior controls the last case ($L/r_y = 325$), with the intermediate case, ($L/r_y = 225$), influenced by both. As a result, the largest effect of combining plastic and elastic effects for fixed arch is for the case of $L/r_y = 325$.

4.4.4 Failure Modes and Response Curves of Fixed Arch

The deflected shape of fixed arch is shown in Figure (4-21) for $L/r_y = 125$ (stiff arch), and in Figure (4-22) for $L/r_y = 225$ (medium arch), for different types of analysis and values of h. Fixing the arch supports results in forcing symmetric failure mode (at the ultimate load) for $h = 0.0$ for both plastic and combined analysis in both figures, and in preventing the large rotation at the plastic hinges near the support. On the other hand, the plastic curve for $h = 0.25$ and $L/r_y = 125$ clearly exhibits bending-dominated behavior, where large plastic deformations occur at the plastic hinges formed in the two quarter-point regions before the arch reaches its ultimate load. This

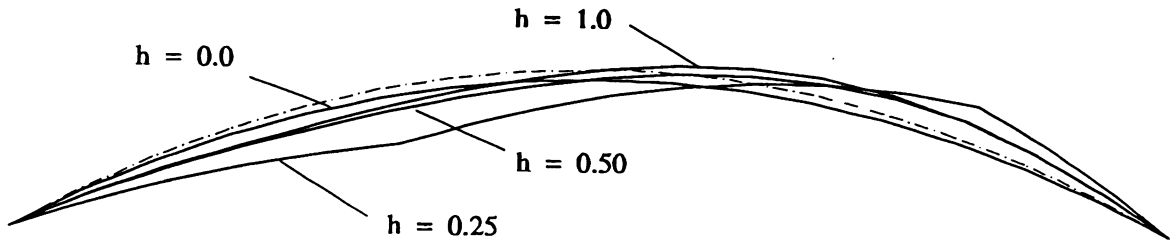

Deflection Magnification
Factor, DMF = 5

(a) Deflected shape under plastic analysis.

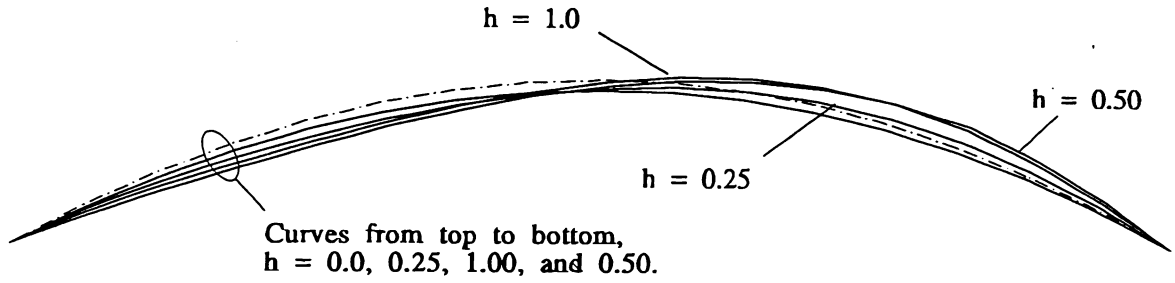

DMF = 5

(b) Deflected shape under combined analysis.

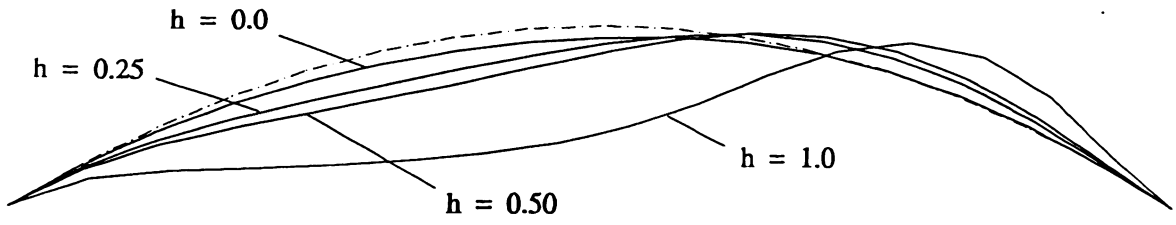

DMF = 1

(c) Deflected shape under elastic analysis.

Figure 4-21 Deflected shapes of fixed stiff arch (L/r_y = 125) at maximum load for different types of analysis and values of h.

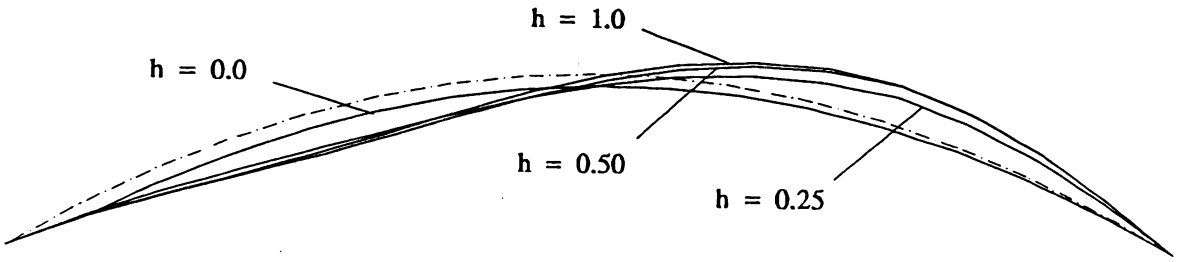

DMF = 5

(a) Deflected shape under plastic analysis.

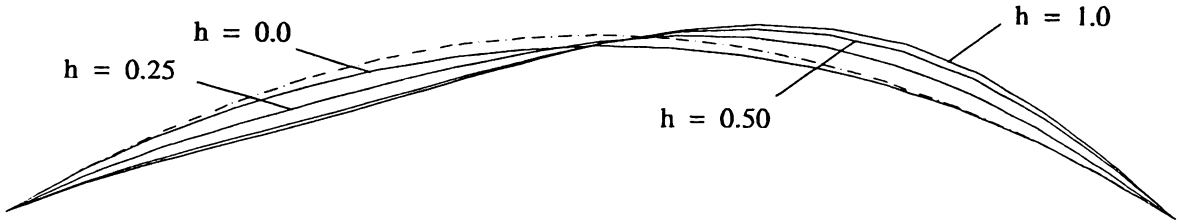

DMF = 5

(b) Deflected shape under combined analysis.

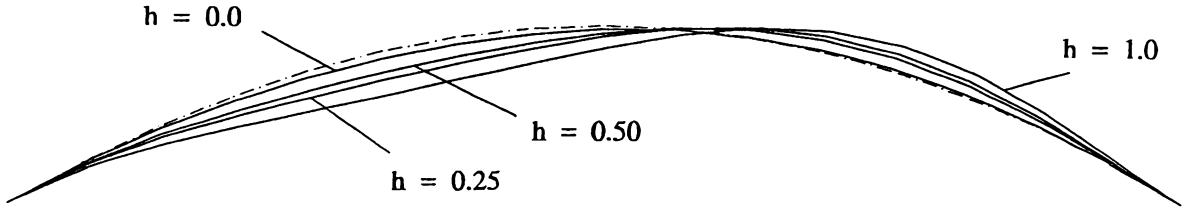

DMF = 1

(c) Deflected shape under elastic analysis.

Figure 4-22 Deflected shapes of fixed medium arch (L/r_y = 225) at maximum load for different types of analysis and values of h.

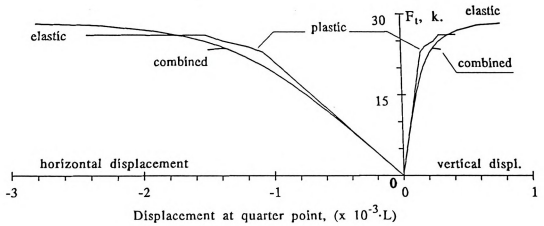

(a) response under vertical load (h = 0.0).

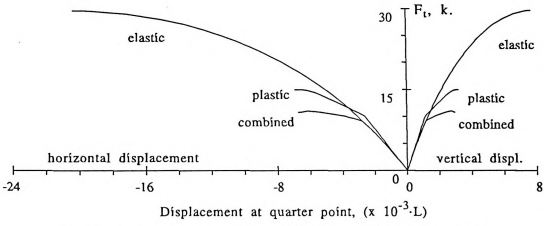

(b) response under vertical and horizontal load (h = 0.5).

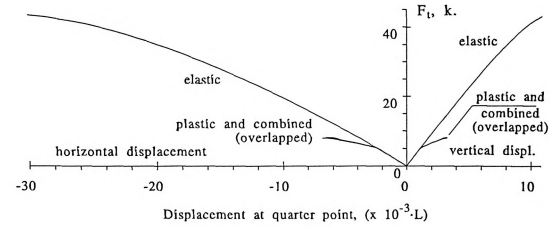

(c) response under horizontal load (h = 1.0).

Figure 4-23 Response curves of fixed medium arch (L/r_y = 225) for different types of analysis and values of h.

demonstrates the redundancy of fixed arch.

All other failure modes for all types of analysis are unsymmetric at ultimate load, with essentially similar trends to those of two-hinged arch; namely elastic deflections are larger than deflections of other types for same L/r_y, and deflection magnitude of plastic and combined curves increases and that of elastic ones decrease with L/r_y. However, the elastic deflection of fixed stiff arch is much larger than that of two-hinged arch, due to the large increase in ultimate load. Also, the plastic and combined curves for different values of h within each group are more separated (i.e., increase gradually with h) than the corresponding curves of two-hinged arch; this is particularly true for combined curves of medium arch.

The longitudinal and vertical displacement response curves of fixed arch ($L/r_y = 225$) are shown in Figure (4-23), where they are comparable to those of two-hinged arch with some differences. For example, the decrease in the initial slope of the curves with h is similar to that of hinged arch but is slower. Also, the ratio of maximum vertical to longitudinal displacements at quarter point exhibit similar trends to those of hinged arch as they change with h, but the ratios are higher.

4.4.5 Plastic Hinge Formation and Force Path at Quarter Point of Fixed Arch

Table (4-3) shows the order of plastic hinge formation in fixed arch ($L/r_y = 225$) for different values of h due to both plastic and combined

Table 4-3 Plastic hinge formation in fixed arch for different types of analysis under different load combinations.

h	Plastic Analysis			Combined Analysis		
	Member: Joint	F at Yield	Yield Action*	Member: Joint	F at yield	Yield Action
0.00	$F_{t,p} = 26.20$			$F_{t,e} = 23.65$		
	1:1	23.10	Y	1:1	23.65	Y
	16:2	24.30	Y			
	1:2	26.15	Y			
	16:2	26.15	U			
0.0625	$F_{t,p} = 25.97$			$F_{t,e} = 19.51$		
	1:1	21.66	Y	1:1	19.50	Y
	16:2	24.40	Y			
	15:1	25.80	Y			
	4:2	25.97	Y			
0.25	$F_{t,p} = 21.39$			$F_{t,e} = 13.90$		
	1:1	16.00	Y	1:1	13.35	Y
	16:2	16.42	Y	16:2	13.64	Y
	13:1	20.80	Y			
	14:1	21.36	Y			
	5:1	21.38	Y			
	13:1	21.39	U			
0.50	$F_{t,p} = 14.92$			$F_{t,e} = 11.00$		
	1:1	10.01	Y	1:1	9.20	Y
	16:2	10.03	Y	16:2	9.21	Y
	13:1	14.41	Y	13:1	11.00	Y
	5:1	14.92	Y			
0.75	$F_{t,p} = 10.67$			$F_{t,e} = 9.22$		
	1:1	6.84	Y	1:1	6.64	Y
	16:2	6.85	Y	16:2	6.80	Y
	13:1	10.42	Y	13:1	9.22	Y
	4:2	10.66	Y			
	5:1	10.66	Y			
1.00	$F_{t,p} = 8.09$			$F_{t,e} = 7.95$		
	1:1	5.21	Y	1:1	5.21	Y
	16:2	5.21	Y	16:2	5.22	Y
	4:2	8.08	Y	13:1	7.80	Y
	13:1	8.08	Y	12:2	7.83	Y
				12:2	7.88	U
				4:2	7.97	Y

* Y = joint yields, U = joint unloads.

analysis, and Figure (4-14) shows the force path at its left quarter point. From the table, for all cases of plastic analysis the first and second plastic hinges form at the left and right supports, respectively, effectively transforming the fixed arch into a hinged one. Afterwards, inner plastic hinges form in a fashion very similar to that of hinged arch, where a plastic hinge forms near the left support for h = 0.0. Also, its position shifts toward the crown as h increases to reach the quarter point at h = 0.25, then remain in the same region as h increase to 1.0. On the right side, plastic hinges form near the right quarter point for h = 0.0625 to 1.0.

For combined analysis, the same observations are essentially true, but the arch may fail due to elastic nonlinearity before development of all the plastic hinges. For h = 0.0, only one plastic hinge forms in the arch before failure, but as h increases, more hinges develop in the arch.

Figure (4-24) shows the force path at the quarter-point of fixed arch (L/r_y = 225). Comparison of the figure with that of hinged arch, Figure (4-14), reveals two main observations. First, all force path curves are shifted toward the N-axis; this shift is more obvious for curves influenced by both axial force and moment (h = 0.0625 and 0.25). Second, the formation of a plastic hinge in the arch causes the force path to shift suddenly toward the M-axis, as evident from the multi-segment curves of h = 0.25.

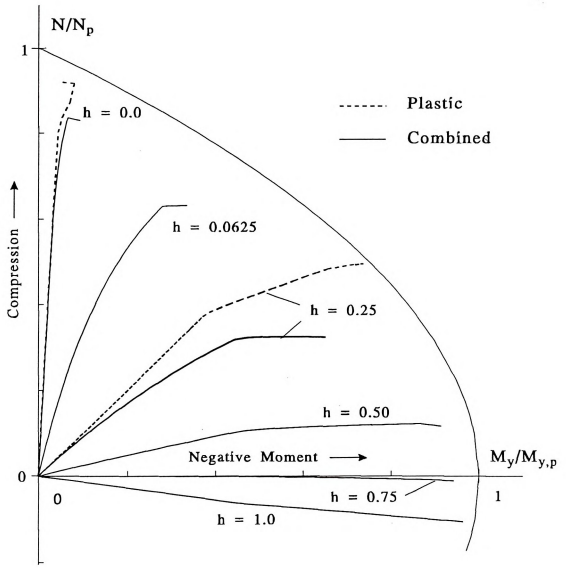

Figure 4-24 Relation between axial force and bending moment at the left quarter point of fixed arch ($L/r_y = 225$).

4.5 ARCH ULTIMATE LOAD UNDER VERTICAL UNSYMMETRICAL LOAD: COMPARISON WITH VERTICAL AND LONGITUDINAL LOAD

The arch ultimate load under vertical unsymmetric loading was extensively studied in the literature, and the different aspects of arch behavior

and design under this type of loading are well understood. By comparing the load carrying capacity under vertical and longitudinal loads with the well known case of vertical unsymmetric load, the process of accounting for the first type of load may become easier.

In this section, the variation with L/r_y of the ultimate load of two-hinged arch under vertical unsymmetric load is presented for different values of the vertical load unsymmetry ratio, r. This ratio is defined in terms of the unsymmetric (e.g., live load) intensity, p_{LL}, which is applied only to one half of the arch span, and the symmetric (e.g., dead load) intensity, p_{DL}, which is applied to the full span length of the arch, so that r is the ratio of the symmetric load intensity to the total (symmetric plus unsymmetric) load intensity, $r = p_{DL}/p_t$, where $p_t = p_{DL}+p_{LL}$. For this study, r is varied from 0.99 (practically symmetric load) to 0.0 (with no symmetric load), with intermediate values of 0.88, 0.50, and 0.33.

Finally, comparison between the case of vertical unsymmetric load and that of vertical and longitudinal loading is made by correlating the vertical symmetric component of the ultimate load under the two cases. This was performed for both two-hinged and fixed arches.

4.5.1 Ultimate Load of Two-Hinged Arch Under Vertical Unsymmetrical Loading

The variation with L/r_y of the plastic, elastic-nonlinear, and combined ultimate loads of two-hinged arch under vertical unsymmetrical loading (for

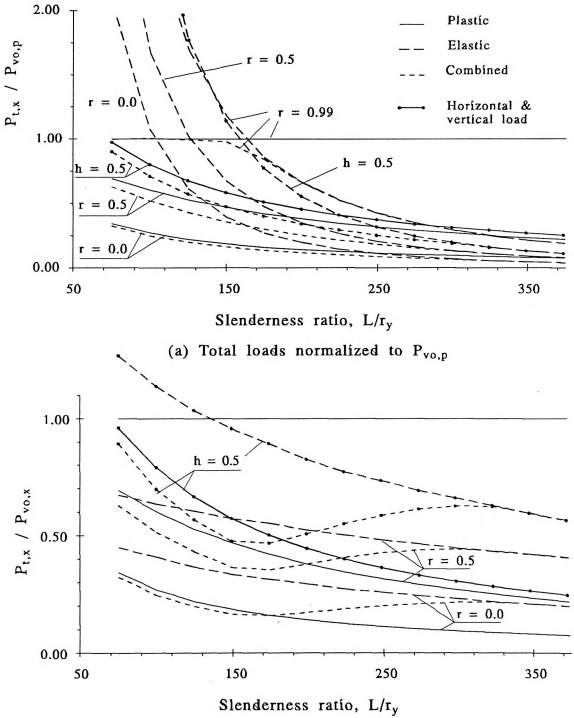

Figure 4-25 Plastic, elastic-nonlinear, and combined ultimate loads of two-hinged arch under unsymmetrical vertical loading.

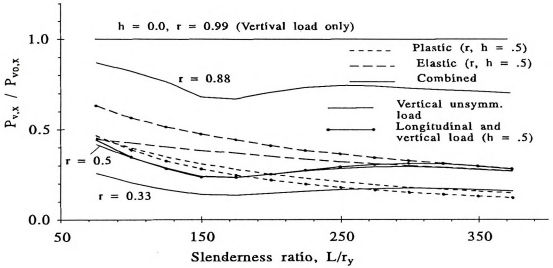

(c) Vertical component normalized to respective vertival loads.

Figure (4-25), continued.

r = 0.99, 0.5, and 0.0) and under vertical and longitudinal loading (for h = 0.50) are shown in Figure (4-25.a) normalized to $P_{vo,p}$. Figure (4-25.b) shows the total ultimate loads and Figure (4-25.c) shows the symmetric vertical components, with the curves of each type of analysis normalized to their corresponding vertical-only ultimate load, $P_{vo,x}$, where x represents p (plastic), e (elastic), and c (combined).

In the first two figures, it is seen that with the decrease of r, the plastic, elastic, and combined ultimate loads significantly decrease from their respective values under vertical-only load, $P_{vo,x}$. The decrease of the vertical unsymmetric curves with r is for the whole range of L/r_y, in contrast with vertical and longitudinal load where, for example, the elastic curves of h = 0.5 exceed those of h = 0.0 at some point.

Comparing curves of unsymmetric vertical load for different types of analysis, it is seen that the plastic load decreases with L/r_y faster than elastic load for constant r, with the combined curve shifting between the two. Figure (4-25.c) shows that for r = 0.50 and h = 0.50, the decrease in vertical component of ultimate load is comparable between the two loading cases for all types of analysis, specially for combined analysis. The combined curves for r = 0.33 and 0.88 are added for illustration of the rate of decrease with r.

Figure (4-26) shows the elastic and combined ultimate loads for r = 0.99, 0.5, and 0.0 normalized to their corresponding plastic ultimate loads of the same value of r. Here also, the figure exhibits similar trends to those of longitudinal loading, where the largest effect of combining elastic and plastic nonlinear effects is for r = 0.5.

4.5.2 Comparison of The Vertical Symmetric Component of The Ultimate Load of Two-Hinged and Fixed Arches for The Two Loading Cases

Direct comparison of the two loading cases in terms of the arch total ultimate load is not the proper measure of the reduction in the arch load carrying capacity, since the loading directions and patterns are different. Instead, the "vertical symmetric" component of the ultimate load (in both cases) is a more accurate and representative measure, since it is the common denominator and measures the arch capacity to carry dead load in the presence of other types of load. The maximum vertical symmetric load that the arch can carry occurs when r = 0.99 and h = 0.0, $P_v(r=0.99,h=0.0) = P_{vo}$. The

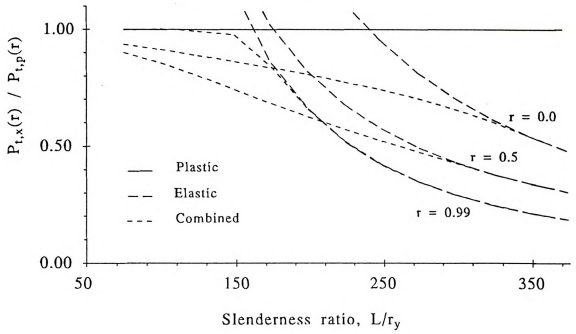

Figure 4-26 Elastic and combined ultimate loads of two-hinged arch under vertical unsymmetrical loading normalized to corresponding plastic ultimate loads of same value of r.

reduction with r and h is measured in comparison with this value.

For vertical and longitudinal load, the vertical component of the ultimate load (which is symmetric by definition) for a given value of h, $P_v(h) = v \cdot P_t(h) = (1\text{-}h) \cdot P_t(h)$. The value of h varies from 0.0 (vertical-only load) to 1.0 (with no vertical load).

For vertical unsymmetric load, the total ultimate load is $P_t = p_{DL} \cdot L + p_{LL} \cdot L/2 = p_t \cdot L\ (r + (1\text{-}r)/2)$, while its vertical symmetric component, $P_v(r) = L \cdot p_{DL} = p_t \cdot L \cdot r$. Expressing P_v in terms of P_t, we can write,

$$P_v(r) = P_t(r) \cdot 2r/(1+r).$$

The unsymmetry ratio, r, varies from 0.99 (for practical vertical symmetric load) to 0.0 (with no symmetric load).

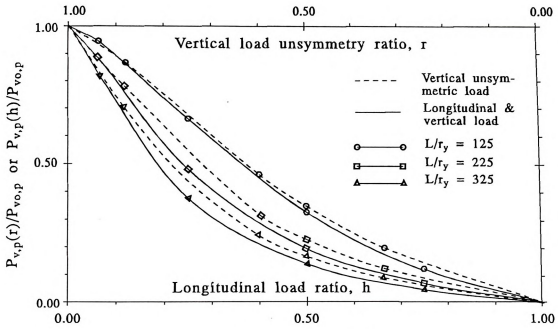

(a) Plastic analysis.

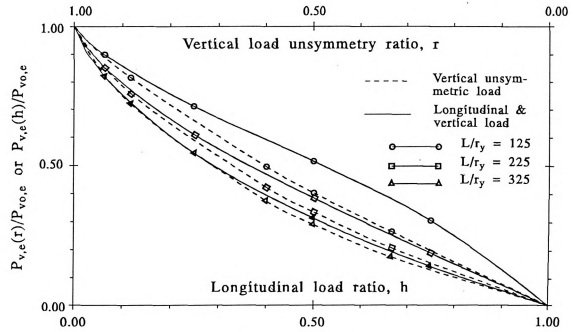

(b) Elastic analysis.

Figure 4-27 Variation of the vertical symmetric component of the ultimate load of two-hinged arch in the presence of vertical unsymmetric or vertical and longitudinal loads.

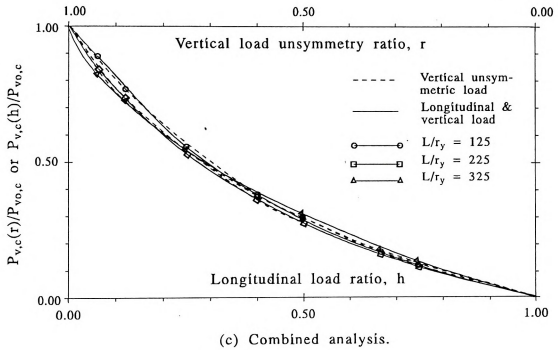

(c) Combined analysis.

Figure (4-27), continued.

Figure (4-27.a, b, and c) show the change in the vertical symmetric component of the plastic, elastic-nonlinear, and combined ultimate loads of two-hinged arch for the two loading cases. Similarly, Figure (4-28.a, b, and c) show the same curves for fixed arch. These figures show that the decrease with (1-r) and with h of the vertical symmetric component, P_v, is essentially similar.

From Figure (4-27), both plastic and elastic curves of two-hinged arch for both loading cases shift down (i.e., the curve nonlinearity increases with h or (1-r)) as L/r_y increases. However, the elastic curves exhibit less nonlinearity than plastic ones, where the vertical and longitudinal elastic curve for L/r_y = 125 is roughly linear, with the nonlinearity increasing with L/r_y until the elastic curve for L/r_y = 325 become close to (i.e., coincides with) that of plastic curve

for L/ry = 125. This behavior explains the very little change in the nonlinearity of combined curves, Figure (4-27.c), which are similar to plastic curves for low L/r_y and similar to elastic curves for high L/r_y.

Comparing the curves of the two loading cases in each part of the figure, it is seen that the plastic and combined curves are very close for a given value of L/r_y, while the difference is larger between the elastic curves, specially for lower L/r_y.

For fixed arch, Figure (4-28), the trends are similar to those of two-hinged arch for plastic and elastic analysis, while the combined curves show larger change with L/r_y. However, both plastic and elastic curves of fixed arch exhibit less nonlinearity with h and (1-r) than their corresponding curves of two-hinged arch. Also, for a given value of h or (1-r), the decrease of the elastic curves from L/r_y = 125 to 325 is larger than that of plastic curves. The combination of these two factors clarify the larger change of combined curves with L/r_y. But more importantly, the curves of vertical unsymmetric load are very similar to those of vertical and longitudinal ones for the same L/r_y.

The nearly identical variation of the ultimate load vertical component, P_v, with (1-r) and h suggests that longitudinal loading on the arch may be accounted for in the preliminary design process by transforming it into an equivalent vertical unsymmetric load. Also, if both vertical unsymmetric and longitudinal loads are present simultaneously along with vertical symmetric load, their effect on reducing the vertical symmetric load capacity may be

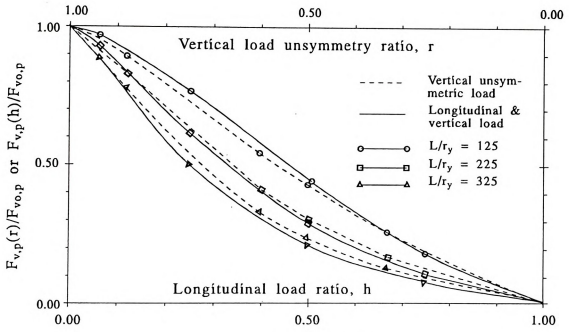

(a) Plastic analysis.

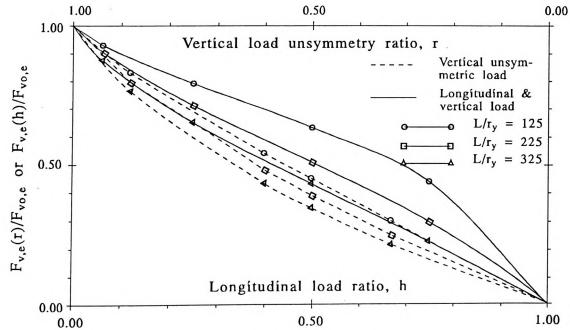

(b) Elastic analysis.

Figure 4-28 Variation of the vertical symmetric component of the ultimate load of fixed arch in the presence of vertical unsymmetric or vertical and longitudinal loads.

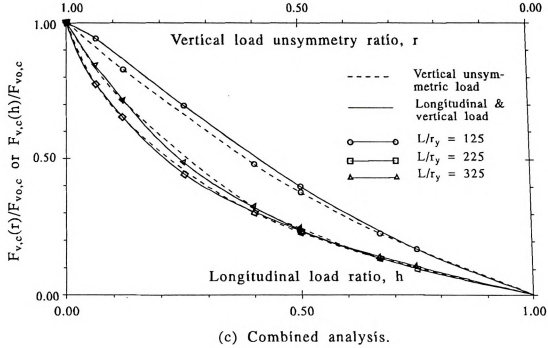

(c) Combined analysis.

Figure (4-28), continued.

accounted for by calculating an equivalent ratio of dead to total load, $r_{eq} = p_{DL}/p_t$, where the total load intensity on the arch, $p_t = p_{DL} + p_{LL} + p_h$, where p_h is the longitudinal load intensity. For example, assume an arch with unsymmetric live load intensity, $p_{LL} = 0.25 \cdot p_{DL}$ and longitudinal load intensity, $p_h = 0.40 \cdot p_{DL}$. The load unsymmetry ratio, $r = 1/(1+0.25) = 0.80$, $(1-r) = 0.20$, and the longitudinal load ratio, $h = 0.40/(1+0.40) = 0.29$. If both effects are added simultaneously, the total load intensity is $p_t = (1+0.25+0.40) \cdot p_{DL} = 1.65 \cdot p_{DL}$, and the equivalent load unsymmetry ratio, $r_{eq} = 1/1.65 = 0.61$, and $(1-r_{eq}) = 0.39$. Verification of this example for a two-hinged arch ($L/r_y = 225$) under combined analysis, produced a difference of less than 3% in the vertical symmetric component of the combined ultimate load between the two cases.

CHAPTER V

PARAMETRIC STUDY OF ARCH BEHAVIOR:

II. THREE-DIMENSIONAL BEHAVIOR

5.1 INTRODUCTION

In this chapter, the arch behavior involving lateral loading is discussed. The interaction between vertical and lateral loading was investigated first, and then the three-dimensional ultimate load surface of an arch under combination of vertical, longitudinal, and lateral loads was constructed.

In the first part, the behavior of fixed arch under combinations of vertical and lateral loads was studied, where the total ultimate load and its vertical component, the interaction curves between vertical and lateral load components, and failure modes and response curves of the arch were obtained using plastic, elastic, and combined analysis. In the second part, the three-dimensional ultimate load surface was constructed using combined analysis, and the interaction between each two of the three components was explored.

For analysis that involves lateral loading, the arch was always fixed in the lateral direction; i.e., the rotations about the global X- and Y-axes were restrained at the supports. This assumption is based on practical considerations where the arch bridge usually consists of two ribs connected by lateral bracing,

and the whole system is restrained from rotation about the X- and Y-axes at the supports. This is also supported by the preliminary analysis results performed in the next section.

5.2 EFFECT OF SUPPORT TYPE AND SECTION PROPERTIES ON THE ARCH ULTIMATE LOAD

Figure (5-1) shows the effect on the ultimate load due to fixing the arch support and varying its section properties in the presence of lateral load. For this purpose, two sections were used, S1 and S2 (Figure (4-1)), with ratios of the out-of-plane to in-plane slenderness ratios of the arch, $(L/r_z)/(L/r_y) = r_y/r_z$, is 2.0 and 1.0, respectively. In Figure (5-1.a), the ultimate vertical loads of S2-fixed arch (i.e., fixed arch with section S2) and S2-hinged arch are plotted against L/r_y normalized to $P_{vo,p}(S1)$. In this figure, the ratio of the lateral load, F_s, to total load, F_t, $s = F_s/F_t$, are 0.0 and 0.001. The ultimate lateral-only loads ($s = 1.0$) of S1-fixed, S1-hinged, and S2-fixed arches are plotted in Figure (5-1.b) against the lateral slenderness ratio, L/r_z, normalized to $P_{so,p}(S2)$.

Note that the arch vertical-only ultimate load is the same for fixed and two-hinged arches for both sections, i.e., $F_{vo,p}(S1) = P_{vo,p}(S1) = P_{vo,p}(S2)$.

Under vertical-only load ($s = 0.0$), the increase in the elastic in-plane ultimate load due to fixing the support is significant (up to 120%, see also Table (4-2)). For the studied section proportions however, this increase disappears almost entirely in the presence of even the smallest lateral load ($s =$

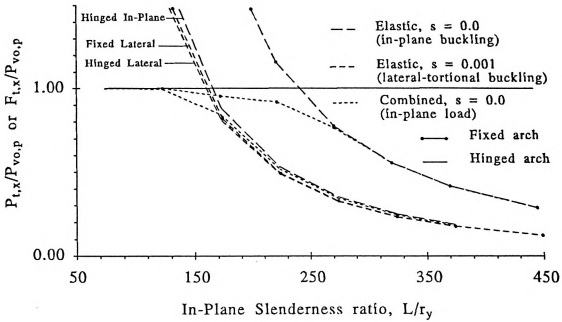

(a) Vertical in-plane and lateral-torsional ultimate loads normalized to $P_{vo,p}$.

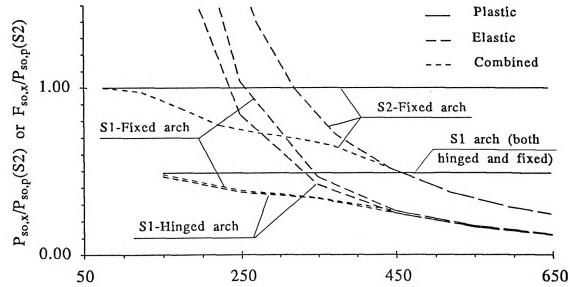

(b) Lateral ultimate loads normalized to $P_{so,p}(S2)$.

Figure 5-1 Effect of the type of arch supports and its relative lateral to in-plane stiffness on its vertical and lateral ultimate loads.

0.001) where the failure mode changes from in-plane to lateral-torsional one and the ultimate loads of hinged and fixed arches become almost equal, with differences of less than 5%. Moreover, these ultimate loads are smaller than -though close to- the vertical in-plane ultimate load of two-hinged arch, leading to the conclusion that the restraint of the in-plane support rotation has negligible effect on the arch ultimate load if it fails in torsion.

Under lateral-only load (s = 1.0), Figure (5-1.b), the plastic ultimate loads of two-hinged and fixed arches of the same section are identical, $P_{so,p} = F_{so,p}$, since the arch is fixed in the lateral direction for both cases and the in-plane properties are irrelevant to lateral load when geometric effects are neglected. The combined and elastic ultimate loads, however, are not identical for the two types of support but are close enough -specially for combined curves- to confirm the above conclusion. In addition, the figure shows the effect of varying the ratio of lateral to in-plane slenderness ratios on the plastic, elastic, and combined lateral ultimate loads where they are about doubled for S2-fixed arch compared to S1-fixed arch.

5.3 BEHAVIOR OF FIXED ARCH UNDER VERTICAL AND LATERAL LOADS

The interaction between vertical and lateral loading was studied for fixed arch only, since the effect of support type on the arch ultimate load was found insignificant. In addition to ultimate loads, the interaction curves between lateral and vertical loading, the deflection modes, and the response curves of

the arch were also studied. The obtained results are discussed in the following sections.

5.3.1 Variation of the Ultimate Load of Fixed Arch with In-Plane Slenderness Ratio

The plastic, elastic, and combined ultimate loads of fixed arch were obtained for different values of the ratio of lateral to total applied load, $s = F_s/F_t$. To adequately trace the change in ultimate load, the values of s = 0.0, 0.001, 0.01, 0.0625, 0.125, 0.25, 0.50, and 1.00 were used.

5.3.1.1 Plastic Ultimate Load of Fixed Arch

Figure (5-2.a) shows the variation with the in-plane slenderness ratio, L/r_y, of the total plastic ultimate load, $F_{t,p}$, normalized to $P_{vo,p}$. Figure (5-2.b) shows the vertical component of the plastic ultimate load, $F_{v,p}$, also normalized to $P_{vo,p}$. From the first figure, it is seen that the ultimate load gradually decreases with L/r_y for constant s. Also, the curves change from linear for small values of s to nonlinear as s increases, with the nonlinearity (i.e., the rate of change with L/r_y) being higher in the low L/r_y range. This behavior is similar to that under vertical unsymmetric loading or vertical and longitudinal loading.

The ratio of the plastic ultimate loads under lateral-only load (s = 1.0) to that under vertical-only load (s = 0.0), $F_{so,p}/F_{vo,p}$, decreases from 20% for L/r_y = 75 to 5% for L/r_y = 450. It is notable that the plastic lateral-only ultimate load is linearly dependent on the section out-of-plane properties, while

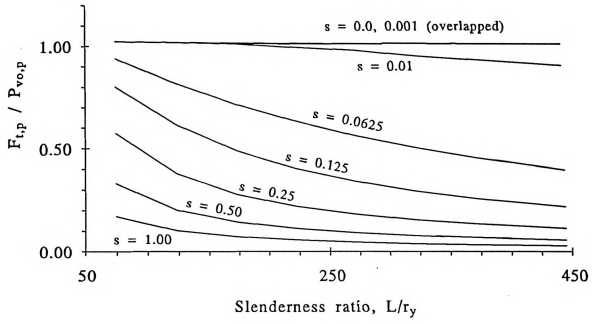

(a) Total load normalized to $P_{vo,p}$.

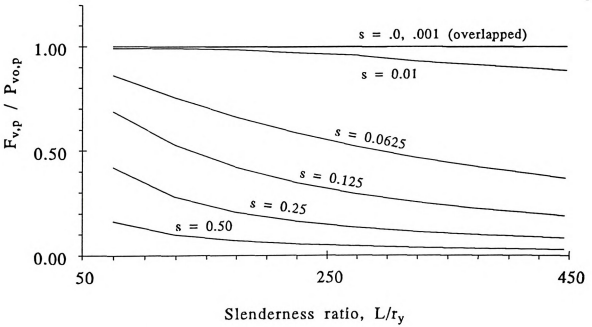

(a) Vertical component normalized to $P_{vo,p}$ (= $F_{vo,p}$).

Figure 5-2 Variation with L/r_y of the plastic ultimate load of fixed arch under vertical and lateral loading

the vertical-only one is dependent on the section in-plane properties, as discussed before. Consequently, the choice of section properties has significant effect on these ratios. In addition, while the proportions of section S1 were chosen to reflect those of a typical box-arch bridge, those of S2 were chosen to have symmetric properties about its major axes. A practical arch bridge would normally have larger lateral stiffness, and therfore larger ratios of $F_{so,p}/F_{vo,p}$.

The vertical component of ultimate load, Figure (5-2.b), exhibits similar trends to those of the total ultimate load but with less degree of nonlinearity for all curves. Similar to the case of longitudinal and vertical loading, the vertical load component always decreases with the lateral load ratio, s. However, the magnitude and rate of decrease also depends on the ratio of $F_{so,p}/F_{vo,p}$, which explains the observed behavior. In contrast, the interaction curves between the vertical and lateral load components (discussed later) are less dependent on the section properties. This discussion is also true for both elastic and combined ultimate loads.

5.3.1.2 Elastic Ultimate Load of Fixed Arch

The variation with L/r_y of the total elastic-nonlinear ultimate load of fixed arch, $F_{t,e}$, is shown normalized to $P_{vo,p}$ in Figure (5-3.a), and to $F_{vo,e}$ in Figure (5-3.b). Its vertical component, $F_{v,e}$, is shown in Figure (5-3.c) normalized to $F_{vo,e}$. The curves in the first two figures show significant drop in the ultimate load for s = 0.001 compared to that of s = 0.0 for the whole range. As mentioned previously, this is due to the change from in-plane failure

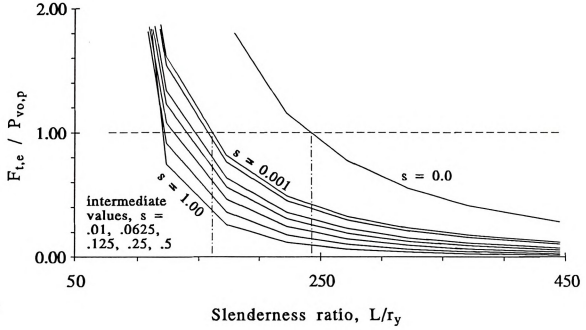

(a) Total load normalized to $P_{vo,p}$.

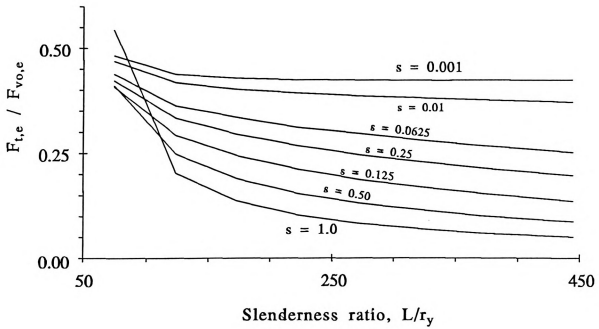

(b) Total load normalized to $F_{vo,e}$.

Figure 5-3 Variation with L/r_y of the elastic ultimate load of fixed arch under vertical and lateral loading.

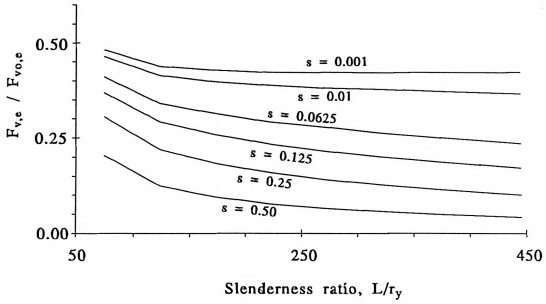

(c) Vertical component normalized to $F_{vo,e}$.

Figure 5-3 continued.

mode to lateral one because the arch in-plane ultimate load is larger than its lateral-torsional ultimate load (also called lateral-torsional buckling load).

From Figure (5-3.b), the curve of s = 0.001 shows a consistent decrease of about 45% from the vertical load ($F_{vo,e}$) for the whole range of L/r_y. Other curves show similar consistent decrease except for very low L/r_y, where they tend to be more nonlinear with low L/r_y. For L/r_y = 75, the curves for s = 0.5 and 1.0 increase with s. The vertical component of the ultimate load, Figure (5-3.c), shows consistent decrease for the whole range of L/r_y (i.e., has less nonlinearity) for all values of s.

5.3.1.3 Combined Ultimate Load of Fixed Arch

The variation with L/r_y of the total combined ultimate load of fixed arch, $F_{t,c}$, is shown in Figure (5-4.a) normalized to $P_{vo,p}$, and in Figure (5-4.b)

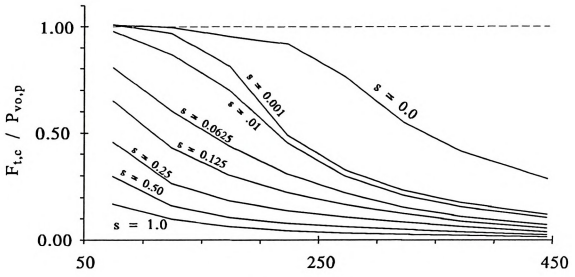

(a) Total load normalized to $P_{vo,p}$.

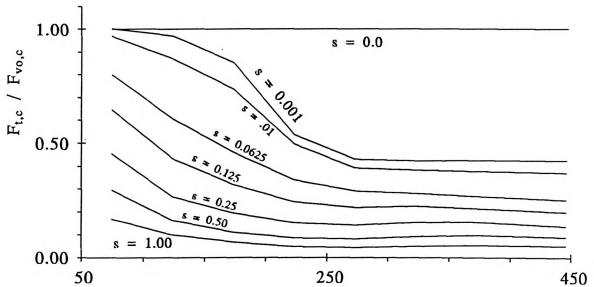

(b) Total load normalized to $F_{vo,c}$.

Figure 5-4 Variation with L/r_y of the combined ultimate load of fixed arch under vertical and lateral loading.

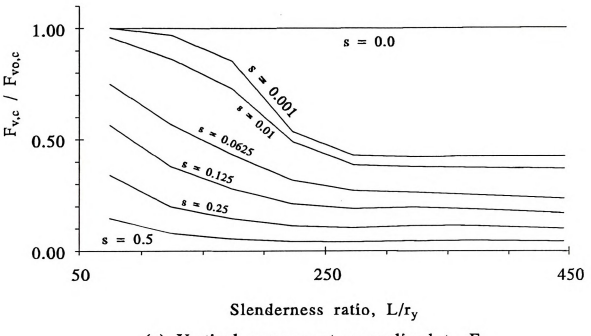

(c) Vertical component normalized to $F_{vo,c}$.

Figure 5-4 continued.

normalized to $F_{vo,c}$. The vertical component, $F_{v,c}$, is shown in Figure (5-4.c) also normalized to $F_{vo,c}$.

From the first figure, for low values of s (≤ 0.06), the combined curves are asymptotic to both plastic and elastic curves, with a sharp decrease of the ultimate load over a short interval of L/r_y. For larger values of s, the transition from plastic- to elastic-dominated behavior is smoother, where for low L/r_y the presence of geometric effects causes larger reduction in combined ultimate loads compared to plastic ones. In addition, as L/r_y increases, the reduction in both plastic and elastic ultimate loads from their respective vertical ultimate loads becomes comparable for constant s, as illustrated in the example below.

Figures (5-4.b and c) show the transition from plastic-dominated to elastic-dominated behavior in terms of the relative reduction of the ultimate

load and its vertical component from the arch vertical ultimate load, $F_{vo,c}$. At $L/r_y \approx 250$, the combined curves are predominated by the elastic behavior.

The above observations are illustrated by the following example. For $s = 0.125$ the reductions in the vertical load capacity of the arch due to plastic, combined, and elsatic analysis (i.e., $F_{v,p}/F_{vo,p}$, $F_{v,c}/F_{vo,c}$, and $F_{v,e}/F_{vo,e}$) for $L/r_y = 75$ are 0.69, 0.58, and 0.37, respectively, and for $L/r_y = 250$ they are 0.32, 0.20, and 0.23 for $L/r_y = 250$. For $L/r_y = 450$, these ratios are 0.19, 0.17, and 0.17, which are very similar for the three types of analysis.

5.3.2 Ultimate Load Interaction Curves

The interaction curves between the vertical and lateral load components of the ultimate load are shown in Figure (5-5) for three values of L/r_y (125, 225, and 325), where they are presented similar to those of longitudinal and vertical ones. The figures on the left show the relative values of the vertical and lateral components of the plastic, elastic, and combined ultimate loads with respect to their corresponding vertical-only and lateral-only plastic loads. Similar to those of two-hinged arch under longitudinal and vertical loading, the ratio of lateral elastic to plastic ultimate loads, $F_{so,e}/F_{so,p}$, is always larger than the corresponding ratio of vertical loads, $F_{vo,e}/F_{vo,p}$. Also, combining elastic and plastic nonlinearity has the largest effect for $L/r_y = 225$, with the plastic and elastic behavior dominating for lower and higher L/r_y, respectively.

In the figures on the right, every load component is normalized to its corresponding ultimate load, for example, $F_{v,e}/F_{vo,e}$ and $F_{s,e}/F_{so,e}$, and so on. It

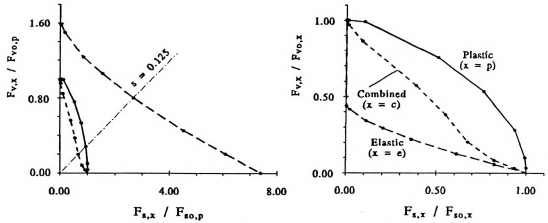

(a) Stiff arch, L/r_y = 125.

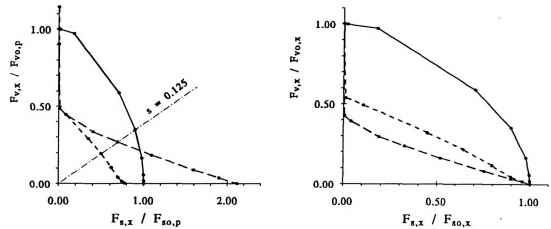

(b) Medium arch, L/r_y = 225.

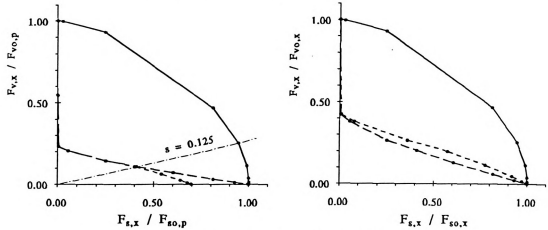

(c) Slender arch, L/r_y = 325.

Figure 5-5 Interaction curves between vertical and lateral load components for fixed arch.

is seen that the plastic interaction curves are convex, while the elastic and combined curves are either linear or slightly concave for the range of s = 0.001 to 1.0. Also, the shapes of these curves are basically independent of L/r_y. The initial drop in the elastic ultimate load due to the change from vertical in-plane failure mode for s = 0.0 to lateral-torsional failure mode for s = 0.001, is consistent over the L/r_y range, while it is gradual for combined curves.

5.3.3 Failure Modes and Response Curves

The vertical and horizontal projections of the deflected shapes of medium arch (L/r_y = 225) corresponding to the ultimate plastic, combined and elastic loads are plotted in Figure (5-6) for s = 0.0, 0.001, 0.01, 0.0625, and 1.0. All deflections are magnified by a factor of 5 for clarity. It is well established that the in-plane failure mode due to vertical-only load (s = 0.0) is always unsymmetric in the presence of geometric effects, although this unsymmetry may not be well developed at the point of ultimate load, as in the case of combined curves in Figure (5-6.b). However, tracing the deflection through post-ultimate load always produces unsymmetric modes.

It is seen that in the presence of lateral load (i.e., for all values of $s \geq 0.001$), the in-plane deflection mode is always symmetric with magnitudes that increase slightly with s. On the other hand, the lateral deflections show distinct increase in their magnitude with s. The only exceptions are the combined curves of s = 0.01 and 0.06 that are almost identical, apparently due to

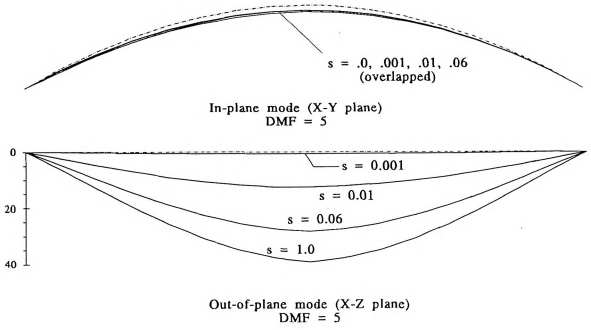

(a) Deflections under plastic analysis.

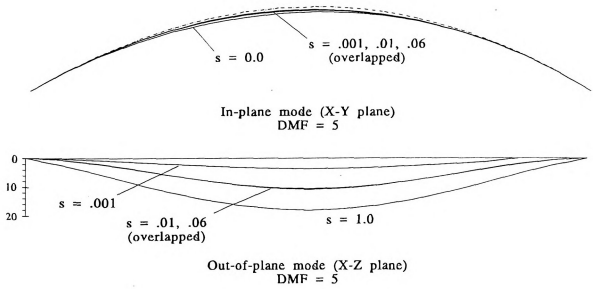

(b) Deflections under combined analysis.

Figure 5-6 Deflected shapes of fixed medium arch (L/r_y = 225) at ultimate load for different types of analysis and values of s.

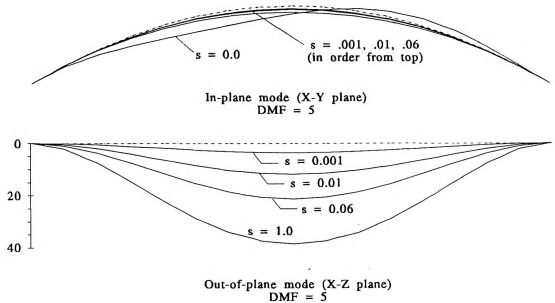

(c) Deflections under elastic analysis.

Figure 5-6 continued.

premature plastic failure.

The magnitudes of combined lateral deflections are smaller than the corresponding plastic or elastic curves (with about 50% reduction) because of premature failure due to combination of geometric and plastic effects, as illustrated later. Also, the rotation at the supports is large for plastic analysis, indicating yielding of joints at the supports. For elastic and combined analysis, it is small indicating that the support did not yield yet at the maximum load (for combined analysis), and the failure is governed by lateral instability of the arch rather than local failure.

The presence of geometric effects propagates lateral deflections, which are substantially larger than corresponding in-plane ones for elastic and combined curves. This becomes clear when comparing the lateral deflection

curves of s = 0.001 to those of s = 0.01 for the three types of analysis. For example, the ratio of maximum lateral deflections at the crown for s = 0.001 and s = 0.01 is about 0.30 to 0.35 for elastic and combined analysis, while this ratio is very small ($<< 0.10$) for plastic analysis.

The response curves at the quarter point of fixed arch (with $L/r_y = 225$) are shown in Figure (5-7) for s = 0.001, 0.01, and 0.06. Figure (5-7.a) clearly shows the effect of geometric nonlinearity on the elastic and combined response curves. As the load is initially applied, the lateral displacement (abbreviated L.D.) is smaller than the in-plane displacement (IP.D.). Also, the curves of elastic, plastic, and combined displacements are the same.

With the progress of loading, however, the lateral displacement increases unproportionally -due to geometric effects- while the in-plane displacement (IP.D.) increases steadily throughout the loading. This behavior continues with accelerated rate until the magnitude of the lateral displacement far exceeds that of in-plane displacement at failure. This is known as the snap-through phenomenon, where the deflection changes from predominantly in-plane mode to an out-of-plane one. For plastic analysis, the two displacements increase proportionally throughout the loading process until failure.

The initial slope of the lateral displacement is more dependent on the value of s where it significantly increases with s, while that of in-plane displacement is roughly the same for the three cases; the two become equal at s = 0.01, Figure (5-7.b). The curves also show that the displacement magnitudes

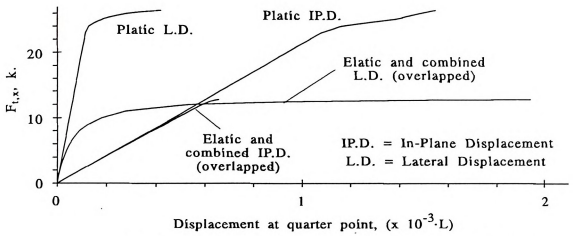

(a) Response under predominantly vertical load, s = 0.001.

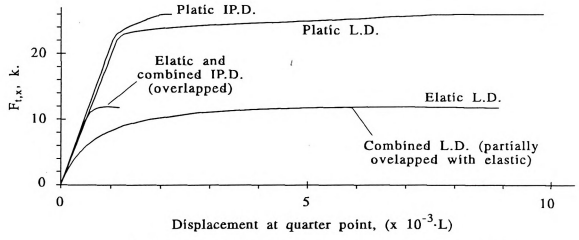

(b) Response under vertical and lateral load, s = 0.01.

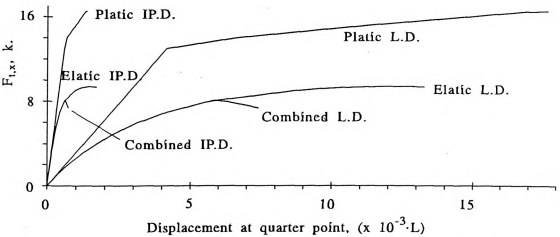

(c) Response under vertical and lateral load, s = 0.06.

Figure 5-7 Response curves for fixed arch under vertical and lateral loading.

at ultimate load significantly increase from s = 0.001 to s = 0.01, but increase to a lesser extent from s = 0.01 to 0.0625. The combined response curve for s = 0.0625 exhibits a sudden decrease after reaching the ultimate load, in contrast with the smooth, horizontal curves for $s \leq 0.01$. This behavior indicates failure due to plastic effects (i.e., formation of plastic hinges), and explains the overlapping of the deflection curves for s = 0.01 and 0.0625 in Figure (5-6.b).

5.4 THREE-DIMENSIONAL ULTIMATE LOAD SURFACE

The objective of this section is to study the interaction between the three types of loading applied simultaneously to the arch under combined analysis, and examine the change in relationship between any two of the three loads in presence of the third. For this purpose, an arch with medium slenderness ratio, $L/r_y = 225$, with S2 section was used.

The ultimate load surface was constructed by applying a load vector that is a combination of the three principal ultimate loads,

$$P' = v' \cdot F_{vo,c} + h' \cdot F_{ho,c} + s' \cdot F_{so,c},$$

where $F_{vo,c}$, $F_{ho,c}$, and $F_{so,c}$ are the combined ultimate loads under vertical-only, longitudinal-only, or lateral-only loading, respectively, also called the principal ultimate loads, and v', h', and s' are their respective scaling factors so that,

$$v' + h' + s' = 1.$$

To obtain a uniform mesh of points on the surface, the value of v' was varied from 0.0 to 1.0 with increments of 0.1. The individual values of h' and

s' were determined from the above relation so that $h' + s' = 1 - v'$, and by defining the ratio of s'/h'. Values of $s'/h' = 0.0$ (i.e., $s' = 0.0$), 0.33, 1.0, 3.0, and ∞ (i.e. $h' = 0.0$) were used. The resulting surface is defined by lines of constant s'/h', called here longitudinal lines for the purpose of discussion. These lines extend from the corner of the principal ultimate load on the vertical axis (where $v' = 1$, $h' = s' = 0$) to the horizontal plane of longitudinal-lateral loads (where $v' = 0$). These lines are intersected by lines of constant v', called transverse lines.

In addition, a value of $s' = 0.02$ was used to produce an additional line on the ultimate load surface that is parallel to the line of $s' = 0.0$. This extra line represents the interaction curve between vertical and longitudinal loading in the presence of a small lateral force that would cause lateral failure mode when it is the controlling mode. This provides insight into the arch behavior as it fails in lateral mode.

The combined ultimate load surface is shown in Figure (5-8) in normalized form, i.e., for each point on the surface the three ultimate load components are normalized to their respective principal ultimate loads. The thick lines on the surface represent the interaction between each two of the three loads. The line of $s' = 0.0$ represents the interaction between only longitudinal and vertical loads, which is the same as the combined curve in Figure (4-20.b), while the line of $h' = 0.0$ represents the interaction between only vertical and lateral loads, and is the same as that of combined analysis in

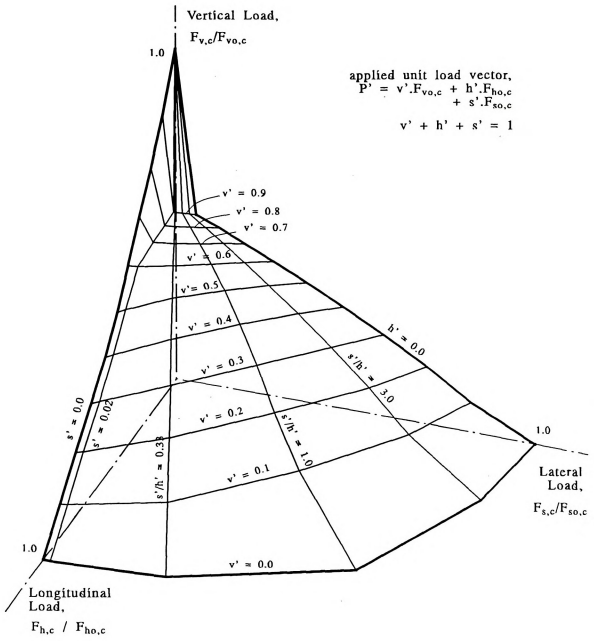

Figure 5-8 Ultimate load surface of fixed arch (L/r_y = 225).

Figure (5-5.b). The line of $v' = 0.0$ represents the interaction between longitudinal and lateral loads, and is denoted as the surface base.

The shape of the ultimate load surface resembles a dome with the vertical load axis as its axis of revolution. In the figure, the line of $s' = 0.0$ is the only longitudinal line that extends smoothly for its entire range. All other longitudinal lines exhibit sharp drop in the vertical component of the ultimate load, $F_{v,c}/F_{vo,c}$, from the vertical corner (where $v' = 1.0$) to the point of $v' = 0.9$. For this point, the ratio of $F_{v,c}/F_{vo,c}$ ranges from 0.55 (for $s' = 0.02$) to 0.52 (for $s' = 1.0$). This sudden drop in the arch vertical ultimate load is attributed to the change of the mode of failure from in-plane to lateral one in the presence of lateral load. From the point of $v' = 0.9$, these longitudinal lines extend smoothly to the surface base ($v' = 0.0$), forming a convex-shaped surface.

5.4.1 Two-Dimensional Interactions Between The Ultimate Load Components

The projections of the ultimate load surface on its principal planes produces the two-dimensional views shown in Figure (5-9.a, b, and c) for vertical-longitudinal, vertical-lateral, and longitudinal-lateral views, respectively.

The presence of lateral load has the effect of consistent reduction of the arch ultimate load with the increase of s'/h', Figure (5-9.a). This is more understood by defining the envelope of the arch ultimate load as the lateral-

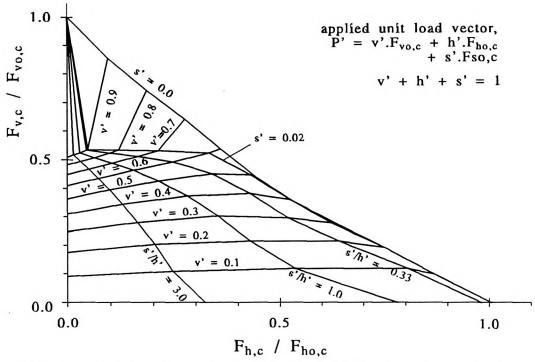

(a) Relation between vertical and longitudinal components.

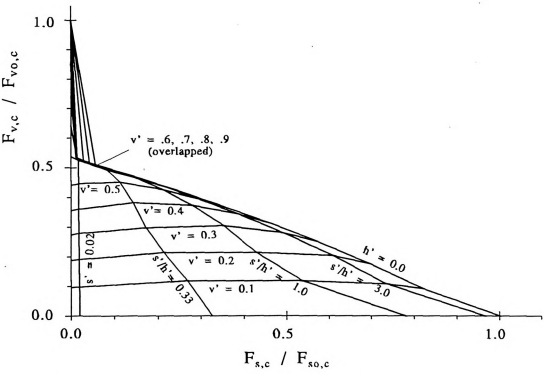

(b) Relation between vertical and lateral components.

Figure 5-9 Projections of the ultimate load surface onto its principal planes.

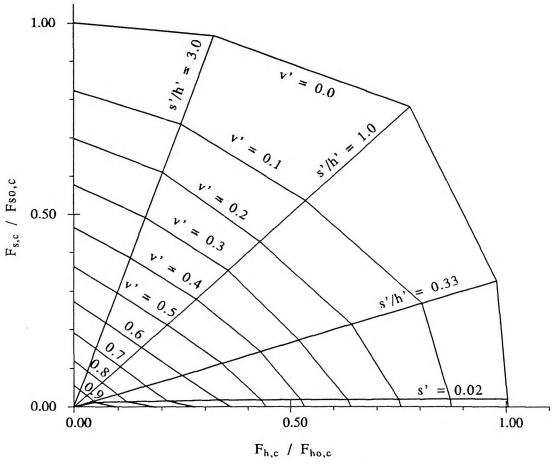

(c) Relation between longitudinal and lateral components.

Figure 5-9 continued.

torsional ultimate load, i.e., the line of $s' = 0.02$. This line represents the practical limit on the arch capacity when it fails in lateral-torsional mode. The lines of $s'/h' =$ constant are basically parallel to this envelope for the whole range of $v' = 0.0$ to 0.9, and the reduction in the arch ultimate load is consistent as s'/h' increases.

It is notable that the change of the failure mode from in-plane mode ($s' = 0.0$) to lateral one (for $s' \geq 0.02$), also changes the shape of the

interaction curves of the ultimate load from a concave one to a convex-like one. This means that an arch with its in-plane vertical ultimate load being smaller than its lateral-torsional vertical ultimate load is more sensitive to the presence of lateral loads; i.e., in the presence of a small lateral load, a longitudinal load (with a given value of h', for example) would decrease the vertical load capacity of such an arch more significantly than it would decrease an arch that has a lateral-torsional vertical ultimate load smaller than its vertical in-plane ultimate load.

The presence of longitudinal load has less consistent effect on the relation between the vertical and lateral components of the ultimate load, Figure (5-9.b). In this figure, the line of $h' = 0.0$ constitutes an upper envelope of the other curves. However, the lines of $s'/h' =$ constant are not parallel to this line, but merge into it as v' increases. In other words, for a given $v' =$ constant, as the ratio of lateral load, s', increases (i.e., the larger s'/h'), the vertical load capacity decreases only slightly.

Analogy may be drawn between this case and the case of column buckling under vertical load with small lateral perturbation load (which corresponds to the lateral load component on the arch); the larger the lateral load, the smoother the response curve and the smaller the obtained ultimate load (as defined by a limit displacement) compared to the theoretical load.

The relation between longitudinal and lateral loads for constant v', Figure (5-9.c), changes gradually -but quickly- from convex for $v' = 0.0$ to

perfectly linear for $v' = 0.6$. For $v' > 0.6$, the relation continues to be linear for the range of $s' = 1.0$ to $s' = 0.02$, which is the envelope for the arch lateral-torsional behavior. For this range, the lines of $v' = 0.6$ to 0.9 are overlapping, Figure (5-9.b), and the vertical component of the ultimate load changes only slightly for all these curves. Consequently, it may be concluded that the presence of longitudinal load has negligible effect on the arch behavior as it fails in a lateral-torsional mode.

CHAPTER VI

SUMMARY AND CONCLUSIONS

6.1 SUMMARY

The main goal of this research is the study of ultimate load capacity of single parabolic arches under different loading combinations. In particular, the interaction between vertical and longitudinal (horizontal in-plane) loading, and between in-plane and lateral (transverse, i.e., normal to the plane of the arch) loading. The developed computer program performs elastic, plastic, and combined analysis (which considers geometric, material, and both nonlinearities, respectively).

6.1.1 Nonlinear Finite Element and Solutions

The arch was modeled using a straight beam finite element model. The elastic nonlinear model used here is that developed by Wen and Rahimzadeh (42), and based on the averaged axial strain model. The plastic behavior was modeled using the classic elasto-plastic hinge model where the plasticity is confined to the member ends, (28).

The member plastic resistance was calculated using a three-stage procedure that traces the member resistance through the three possible stages of

having both end joints elastic, one plastic, and both plastic. For each stage involving plasticity at a joint, the new force point -which is calculated using the plastic stiffness matrix- was made to stay at the yield surface by iteratively modifying the gradient vector at the beginning of that stage.

For combined analysis, the elastic-nonlinear stiffness matrix used in the plastic hinge model is calculated as a function of the elastic portion of the member displacement vector. But since it was not known beforehand, the value at the previous iteration -on the structure level- was used.

Four types of functions were used to represent the yield surface, namely spherical, triangular, parabolic, and inverse parabolic. The singularity of the gradient in the regions of discontinuity in these functions, i.e., along ridges and at corners of the yield surface, was avoided by using special substitute functions that would produce a unique direction in the singularity region.

The nonlinear solution used the fixed coordinates (vis-a-vis moving coordinates), and the elements stiffness matrices were derived using the Lagrange-small rotations coordinates. The system of nonlinear equations on the structure level was solved using a modified Newton-Raphson method with acceleration scheme, (9). A displacement-controlled procedure, (6), was used to trace the response beyond the ultimate load point when needed. In addition, a simple procedure for load step adjustment was implemented to define the ultimate load more precisely. The solution convergence was checked using separate displacement, force and energy tests.

Comparisons with reported solutions in the literature seem to validate the program and show good agreement between the current implementation of nonlinear element models and those reported by others. Comparisons with experimental results show that the inverse parabolic function gives the most consistent results, and therefore was used in the parametric study.

6.1.2 In-Plane Arch Behavior

The plastic, elastic, and combined ultimate loads of both two-hinged and fixed arches were studied under different combinations of vertical and longitudinal loading.

The change with slenderness ratio, L/r_y, in the total ultimate load from that under vertical load only due to increasing the longitudinal load depends significantly on the type of analysis (i.e., the presumed behavior of plastic, elastic-nonlinear, or combined). The plastic ultimate load gradually decreases with an increase in the ratio of longitudinal to total loads, h, except for very low values of L/r_y and h. The elastic ultimate load increases with h for lower values of L/r_y and decreases for higher values.

The combined ultimate load is similar to plastic ultimate load for lower L/r_y -where plastic effects control the arch behavior- while it is similar to elastic load for higher L/r_y. Also, the effect of combining both plastic and geometric nonlinearities is maximum for $h = 0.25$, where the total load resultant is perpendicular to the chord extending from the arch support to its crown.

For two-hinged arch, the ratio of longitudinal to vertical plastic ultimate loads, $P_{ho,p}/P_{vo,p}$, range from 60% for stiff arches to 15% for slender ones. For fixed arch, the respective ratios are 90% and 20%. The corresponding ratios of elastic ultimate loads, $P_{ho,e}/P_{vo,e}$, range from an increase of 400% to a decrease of 45% for two-hinged arch, and from more than 800% to 90% for fixed arch. The combined analysis ratios, $P_{ho,c}/P_{vo,c}$, for two-hinged arch decrease from 60% for stiff arches to 30% for medium arches, but the ratio increases to 45% for slender arches. For fixed arch, these ratios are 90%, 30%, and 40%, respectively. For a given value of h, the reduction in the arch capacity to carry vertical load is strongly dependent on the ratio of the ultimate load under vertical-only load to that under longitudinal-only load.

Compared to two-hinged arch, fixing the arch supports results in 100% increase in the vertical-only elastic ultimate load and at least 300% increase in longitudinal-only ultimate load. The vertical-only plastic load remains the same because of failure due to pure axial load in both cases, while the longitudinal-only plastic ultimate load increases by 50%.

For both two-hinged and fixed arches, the interaction curves between vertical and longitudinal components of the ultimate load are convex for plastic analysis and concave for elastic analysis. Those of combined analysis change from convex to concave as L/r_y increases.

The arch capacity to carry vertical load (e.g., dead load) due to the presence of longitudinal load always decreases for all types of analysis. However, this decrease is larger for plastic analysis than elastic analysis.

Comparison of the arch behavior under vertical symmetrical and longitudinal load with its behavior under vertical unsymmetrical loading reveals similar behavior. This is specially true with regard to the rate of decrease of the vertical symmetric component in both cases. This similarity provides a simple measure of the decrease in arch capacity to carry both live and earthquake loads simultaneously with the dead load, for example.

The failure modes at ultimate load are unsymmetrical, and the deflection magnitude at ultimate load increases with h for all types of analysis. The magnitudes for combined analysis are smaller than those of elastic and plastic types of analysis. As L/r_y increases, the magnitude of elastic deflections at ultimate load decreases, while that of plastic and combined analysis increases.

For two-hinged arch, the plastic hinge formation moves from near the support toward the quarter point as h increases from 0.0 to 0.25, then stays in that region as h increases further. For fixed arch, plastic hinges form at the support first. Afterwards, the arch behaves similar to two-hinged arch. The force path at the quarter point of the arch span shifts from predominantly compression axial force for vertical load only to predominantly bending moment as the longitudinal load ratio increases. This behavior is accelerated in the presence of geometric effects, and due to fixing the arch supports.

6.1.3 Out-of-Plane Arch Behavior

The lateral ultimate load is insensitive to fixing the arch against in-plane rotation at the supports, while the section lateral properties affect it proportionately. As a result, only fixed arch was studied.

Under vertical and lateral loading, the arch plastic ultimate load decreases gradually as the ratio of lateral to vertical load, s, increases. The elastic ultimate load drops suddenly in the presence of lateral load due to change from in-plane to lateral failure mode. The combined ultimate load shifts from a gradual decrease to a sudden drop as L/r_y increases. Since the in-plane and out-of-plane ultimate loads are not directly related to each other, their relative ratios are not meaningful, and the observed trends of ultimate load cannot be generalized; instead, the reduction in the vertical component with s is more meaningful.

The interaction curves are convex for plastic analysis, and slightly concave for elastic analysis. Those of combined analysis are closer to elastic curves for the whole range of L/r_y. At the ultimate load, the lateral deflections are distinctly larger than in-plane ones for all types of analysis, with the combined curves having smaller magnitudes. The plastic hinge formation at supports causes large rotations and contributes to the large deflections.

The combined ultimate load surface was constructed by applying the three loads simultaneously, namely, vertical, longitudinal, and lateral loads. The shape of the surface roughly resembles a dome with the vertical load axis

as its axis of revolution. However, the relative magnitude of the arch vertical in-plane to the lateral-torsional ultimate loads is important in determining the shape of the surface. For an arch with lateral-torsional ultimate load larger than its in-plane vertical ultimate load, the ultimate load surface would have a significantly different shape.

When the arch fails in lateral-torsional mode, as in the studied case, its capacity to carry vertical load does not change significantly in the presence of relatively small longitudinal load (up to $0.4 \cdot F_{ho,c}$). Similarly, a small lateral load (up to $0.2 \cdot F_{so,c}$) has negligible effects. This is due to the convex ultimate load surface. The interaction curve between lateral and longitudinal loads is convex for low vertical load ratio, and becomes linear as the magnitude of vertical load component reaches the lateral-torsional ultimate load.

6.2 CONCLUSIONS

The main conclusions of this research are summarized in the following:

1. The plastic hinge model is versatile enough to represent the unique arch behavior when the axial force in the element is high. The function type used to represent the yield surface in the plastic hinge model has significant effect on the arch ultimate load. The inverse parabolic function produced values closer to experimental results than other types of functions compared.

2. The presence of longitudinal loads on the arch significantly decreases the arch capacity to carry vertical loads for all type of analysis, particularly plastic analysis. The ratio of the arch ultimate load under longitudinal-only load to its

ultimate load under vertical-only load is an important factor in affecting the rate of decrease.

3. The combined analysis represents a lower bound for both elastic and plastic types of analysis, and the arch behavior shifts from one that is dominated by plastic behavior to one that is dominated by elastic behavior as L/r_y increases. The effects of combining both plastic and geometric nonlinearities is highest when the ratio of longitudinal to total loads, $h \approx 0.25$, when the direction of the total load resultant would be approximately perpendicular to the chord extending between the arch support and its crown.

4. The presence of longitudinal load affects the arch behavior in many aspects in a quite similar way to the presence of unsymmetrical gravity load (e.g., live load), in particular, in the reduction of arch capacity to carry vertical symmetrical load (e.g., dead load). This suggests using an equivalent unsymmetrical load to represent the longitudinal load effects in a preliminary design process.

5. When the arch lateral-torsional ultimate load is smaller than its in-plane vertical ultimate load, the arch failure mode changes from in-plane to out-of-plane mode. Moreover, the presence of lateral load on the arch causes significant drop in the arch ultimate load.

6. The shape of the ultimate load surface is significantly related to the failure mode. For out-of-plane failure mode, the surface shape due combined analysis was found to convex-like.

6.3 RECOMMENDATIONS

The behavior of arches under different combinations of loading is broadly open for research. The following topics are some examples of topics still in need of exploration.

1. The arch behavior under combinations of both vertical unsymmetrical and longitudinal loads simultaneously with vertical symmetrical loads needs to be studied, with the aim to develop a quantitative relationship between the arch load carrying capacities for the two modes of loading. It is reasonable to expect the results to support the current findings.

2. The study of arch bridges as a whole system need to be studied more extensively. The extension of this study to include the effect of different components of the arch is recommended. for example, the effect of the arch deck and in-plane and out-of-plane bracing systems on the arch ultimate load under longitudinal loads.

Also, expansion of the study of the interaction between vertical and lateral loads and the ultimate load surface to include different ratios of lateral to in-plane section properties and lateral bracing systems would produce useful data for design.

3. Study of the dynamic effects of earthquake loading on the arch vertical ultimate load capacity is important. In particular, estimation of the equivalent static longitudinal load that represents the dynamic earthquake effects for design purpose is needed.

APPENDIX

APPENDIX A

METHODS OF SOLUTION OF NONLINEAR F.E.M. EQUATIONS

A.1 INTRODUCTION

The system of nonlinear equations generated by the finite element model is solved here using procedures based on the Newton-Raphson iteration method. The ultimate load of the structure is obtained by incrementally applying the unit load vector to the structure until failure. This may be called load-controlled analysis since the analysis is controlled by increasing the load parameter.

After the ultimate load point, more than one displacement path may be possible for the same load decrement. For example, the displacement path may follow an unloading path where the displacement direction is basically opposite to that during loading, or may follow a post-ultimate load path where the displacement path is a continuation of that during loading. The direction of displacement is controlled by including it in some manner as a controlling parameter in the analysis, and is called displacement-controlled analysis.

For this study, the load-controlled analysis procedure is the main procedure used to obtain the ultimate load of the structure. The use of the

displacement-controlled procedure was limited to tracing the structure response curves beyond the ultimate load and for comparison with previous analytical methods.

Two methods for load-controlled nonlinear incremental analysis were implemented: the direct Newton-Raphson (N-R) method, and the modified Newton-Raphson method. The displacement-controlled analysis method is implemented in parallel with the modified N-R method. The accelerated modified Newton-Raphson method is used throughout the study for data collection in association with displacement-controlled analysis when needed.

In this appendix, theoretical description and implementation of the three methods is presented.

A.2 DIRECT NEWTON-RAPHSON METHOD

The nonlinear finite element equilibrium problem amounts to finding the solution of the nonlinear equation, (for example, see ref. (5)),

$$f(D) = P^j(D) - R^j(D) = 0,$$

where $P^j(D)$ is the applied load through load increment j (assumed here to be independent of D), $R^j(D)$ the structure resistance at the end of increment j, and D is the (unknown) structure displacement that satisfies the equation.

The direct Newton-Raphson method is a first order Taylor's series expansion of the nonlinear function, f(D), about the converged (known) solution point at the beginning of increment j so that,

$$f(D_o^j + dD_1^j) \approx f(D_o^j) + \left[\frac{\partial f}{\partial D}\right]_o dD_1^j.$$

In general, the derivative is the slope of the curve at point o, and for structural analysis problem it is the structure tangent stiffness matrix at that point, $K_{t,o}^j$; $f(D_o^j + dD_1^j) = P^j - R^j$, the equilibrium function at the end of increment j; and $f(D_o^j) = P_o^j - R_o^j(D_o) = 0$, the equilibrium function at the beginning of the increment, Figure (A-1). The incremental form of the above equation is $\Delta P^j = dP_o^{u,j} \approx K_{t,o}^j \cdot dD_1^j$, where ΔP^j is the applied load for the increment at the beginning of the solution, i.e., for the first iteration,

$$dP_o^{u,j} = \Delta P^j = \Delta f^j \cdot P^{lv} + dP^{r,j-1}, \qquad (A.1)$$

where Δf^j is the load parameter that defines the actual loading forces as a ratio of the applied unit load vector, P^{lv}, and $dP^{r,j-1}$ the residual force vector still unbalanced after convergence at the end of previous increment. The increment index, j, may be omitted in the following discussion for simplicity.

Since Taylor's expansion was truncated, the obtained solution, dD_1, is only an approximation and the process needs to be repeated with the new point (1) as the expansion point and so on until convergence is achieved. For iteration i, the structure resistance at point (i) is calculated, $\Delta R_i = \Delta R(D_o^j, \Delta D_i)$, where $\Delta D_i = dD_1 + \ldots + dD_i = \Delta D_{i-1} + dD_i$, and the new unbalanced force vector at the end of iteration is found, $dP_i^u = \Delta P - \Delta R_i$. The incremental equilibrium equation for iteration **i** may be written as,

$$f(D_1) = \Delta P - \Delta R_i(D_o, \Delta D_i) = 0, \qquad (A.2)$$

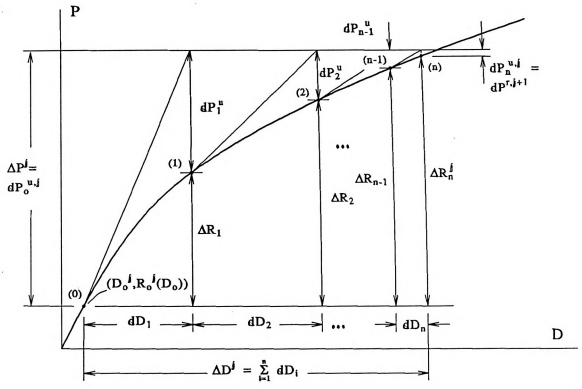

Figure A-1 Direct Newton-Raphson iteration process for solution of nonlinear equations.

and the Newton-Raphson iteration equation is,

$$K_{t,i-1}\, dD_i = dP_{i-1}^{u}. \qquad (A.3)$$

To avoid errors resulting from path-dependency, specially when plastic effects are included, the increment resistance is calculated over the whole increment for every iteration, $\Delta R_i = \Delta R(D_o, \Delta D_i)$, rather than accumulating the resistance increments for individual iterations, ΔR_i = sum ($dR_1(D_o, dD_1)$, ..., $dR_i(D_{i-1}, dD_i)$).

As discussed in chapter 3, if the solution process becomes unstable during iteration, the step size is reduced and the increment is repeated. If it

becomes unstable for the smallest load increment, the analysis is either stopped or switched to displacement-controlled procedure.

A.3 MODIFIED NEWTON-RAPHSON METHOD

In the direct Newton-Raphson method the structure tangent stiffness matrix is evaluated for every iteration. For large number of degrees of freedom, this consumes unproportionately large part of the computation time. The modified Newton-Raphson method avoids this by using the tangent stiffness matrix at the beginning of the increment, $K_{t,o}^{j}$, for all iterations during the increment, Figure (A-2.a), so that,

$$K_{t,o}\ dD_i^{*} = dP_{i-1}^{u}. \tag{A.4}$$

This modification is based on the assumption that $K_{t,o}^{j}$ is a reasonable estimate of the slope of the response curve at point i (i.e., $K_{t,i}^{j}$) for all subsequent iterations. The disadvantage of this assumption is that the convergence rate becomes slower and the expected benefit may be negated by the increase in number of iterations required to obtain convergence. This is specially true when the stiffness significantly changes during the increment, due to new yielding of some member joints for example.

To overcome this drawback, an acceleration procedure reported by M. A. Chrisfield, (9), and based on the secant approach was implemented to accelerate convergence. In this procedure, the initial displacement vector produced by standard modified Newton-Raphson method for a given iteration is replaced by an improved estimate that is a function of the unbalanced force and

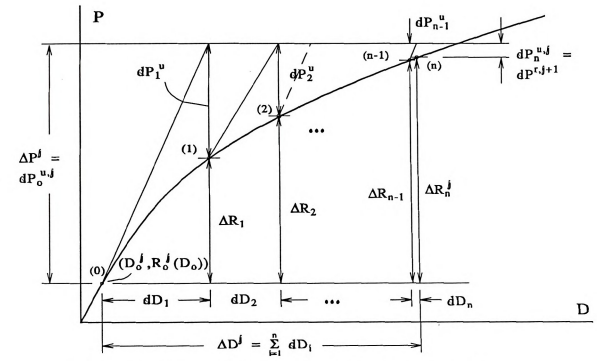

(a) Standard modified Newton-Raphson method.

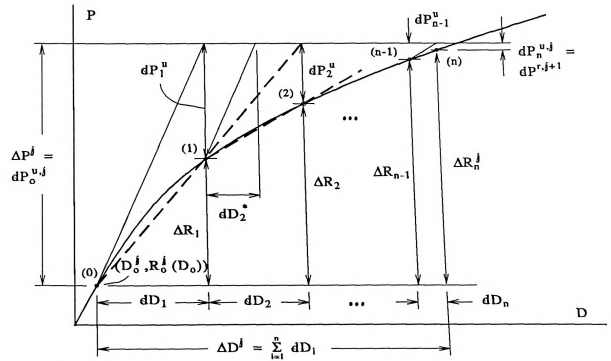

(b) Accelerated modified Newton-Raphson method.

Figure A-2 Modified Newton-Raphson iteration process for solution of nonlinear equations.

displacement vectors of the current iteration and previous one.

In this procedure, Figure (A-2.b), the initial displacement vector, dD_i^*, for iteration i is found using equation (A.4) above, and the improved estimate of the displacement vector, dD_i is calculated,

$$dD_i = f_{1,i}\, dD_{i-1} + f_{2,i}\, dD_i^* \qquad (A.5)$$

where $f_{1,i}$ and $f_{2,i}$ are scalar factors defined as follows,

$$f_{2,i} = -f_{3,i} / f_{4,i},$$
$$f_{1,i} = f_{2,i} (1 - f_{5,i}/f_{4,i}) - 1,$$

where $f_{3,i}$, $f_{4,i}$, and $f_{5,i}$ are the following scalar (inner) products,

$$t_{1,i} = dD_{i-1}^T \cdot dP_{i-2}^u,$$
$$t_{2,i} = dD_{i-1}^T \cdot \delta P_{i-1}^u,$$
$$t_{3,i} = dD_i^{*T} \cdot \delta P_{i-1}^u.$$

where δP_{i-1} is the difference between the unbalanced forces at the beginning of the current and previous iterations, $\delta P_{i-1} = dP_{i-1}^u - dP_{i-2}^u$. The process is started with $f_{2,o} = 1$, $f_{1,o} = 0$, and $dP_o^u = \Delta P$.

Equation (A.5) above can be shown to be a form of secant relationship by multiplying both sides of that equation by the difference between the unbalanced forces, δP_{i-1}, which produces the following equation,

$$dD_i^T \cdot \delta P_{i-1}^u = dD_{i-1}^T \cdot dP_{i-1}^u.$$

For one degree-of-freedom system, this equation is described by the secant line passing between points (0) and (1) in Figure (A-2).

When the change in stiffness during the increment and hence in response is substantial, the acceleration procedure may cause false divergence of the iteration process since it is based on the secant approach. To avoid this instability, an upper limit is imposed on the norm of the accelerated displacement vector so that,

$$\| dD_i \| / \| dD_{i-1} \| \leq \text{maximum ratio} = 5.$$

While slower convergence may occasionally result from this constraint, its stabilizing effect is generally advantageous.

In equation (A.4), the stiffness matrix at the beginning of the increment, $K_{t,o}$, may produce unstable results. In this case it is reformulated with one or both of the nonlinear effects being restricted. For example, when both plastic and geometric nonlinearities are present the stiffness matrix is reformulated using only geometric effects, $K_{eg,o}$. If it is still unstable or when only one effect is present it is reformulated as the elastic-linear stiffness matrix, K_o. If divergence still occurs, it is an indication that ultimate load has been reached and the analysis is either stopped or switched to displacement-controlled analysis.

A.4 DISPLACEMENT-CONTROLLED ANALYSIS

The displacement-controlled analysis procedure used here is based on controlling the displacement increment at a specified degree of freedom of a selected structure node, as described by Batoz and Dhatt, (6). Instead of specifying the direction and magnitude of the load parameter for load-

controlled increment and solving for the corresponding displacement vector, for this procedure the direction and magnitude of the displacement at the specified d.o.f., Γ, is specified and the nonlinear solution is sought for the rest of the displacement vector and the load parameter (its magnitude and direction) that satisfies the specified displacement.

In the following, the basic concept of this procedure is demonstrated by explaining the steps through the first two iterations, Figure (A-3), then the general iterative equations are presented. This procedure is implemented in parallel with the modified Newton-Raphson method; i.e., the structure stiffness matrix is formulated and updated similar to that used for modified N-R method. The initial steps of solution are as follows,

1. The solution begins by formulating the structure stiffness matrix at the beginning of the increment and solving for the displacement vector, D^{lv}, corresponding to the applied unit load vector, P^{lv}.

The structure and solution instability is handled the same way as the modified Newton-Raphson method. For direct Newton-Raphson method, the stiffness would be updated at the beginning of every iteration.

2. The iteration process begins by assuming (or estimating) the displacement vector for the first iteration, dD_1, and the corresponding initial unbalanced force vector, dP_o^u. The corresponding structure resistance and the unbalanced force vectors are calculated, $\Delta R_1 = f(D_o, dD_1)$ and $dP_1^u = dP_o^u - dR_1$, respectively.

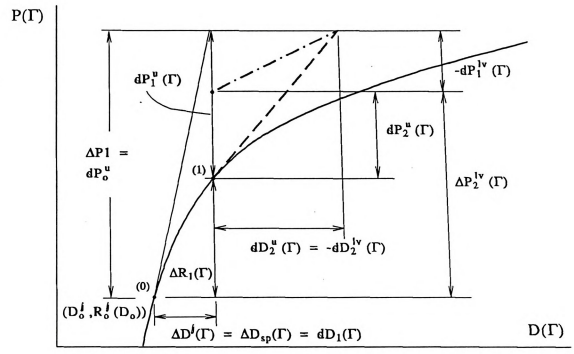

(a) Load-displacement Relation at d.o.f. Γ.

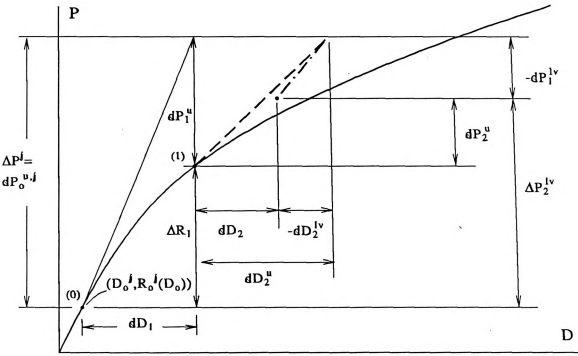

(b) General load-displacement relation for the rest of the structure.

Figure A-3 Displacement-controlled analysis iteration process for solution of nonlinear equations.

Batoz and Dhatt, (6), assume the value of dD_1 to be zero for all entries except for Γ where it is equal to the specified value, $dD_1(\Gamma) = \Delta D_{sp}(\Gamma)$, and the initial iteration load parameter, $\Delta f_1 = df_o = 0$ (i.e., $dP_o^u = dP^{r,j-1}$). An alternative approach used here is to scale the displacement vector, D^{lv}, and the unit load vector, P^{lv}, so that the displacement at Γ is equal to the specified value, $dD_1(\Gamma) = \Delta D_{sp}(\Gamma)$. The corresponding initial load parameter is, $df_o = \Delta D_{sp}(\Gamma)/D^{lv}(\Gamma)$, so that $dP_o^u = df_o \cdot P^{lv} + dP^{r,j-1}$, and $dD_1 = df_o \cdot D^{lv}$. The load parameter and displacement vector at the end of first iteration are, $\Delta f_1 = df_o$, and $\Delta D_1 = dD_1$.

The value of $\Delta D_{sp}(\Gamma)$ is estimated from its value at the end of the load-controlled analysis under the same load vector. The average displacement per unit load vector is calculated at the beginning of displacement-controlled analysis, $D'^{,LCA}(\Gamma) = D^{LCA}(\Gamma)/f^{LCA}$, where $D^{LCA}(\Gamma)$ and f^{LCA} are the total displacement at Γ and total load parameter, respectively, at the end of load-controlled analysis. The value of the specified displacement, $\Delta D_{sp}(\Gamma)$, corresponding to a given value of the load parameter increment, Δf_{init}, (specified in data input, for example) may be obtained, $\Delta D_{sp}(\Gamma) = \Delta f_{init} \cdot D'^{,LCA}(\Gamma)$ (note that $\Delta f_{init} \neq df_o$). The final value of the load parameter after convergence would be different from its initial value. The value of Δf_{init} is adjusted in case of divergence during analysis similar to the load-controlled analysis.

3. For the second iteration, the unbalanced force vector at the beginning of the iteration, dP_1^u, is applied to the structure, and the resulting displacement vector

is calculated, $dD_2^u = (K_{t,o}^j)^{-1} \cdot dP_2^u$, as shown by the dashed line in the figure. This generates additional displacement at Γ, changing its specified value of $\Delta D_{sp}(\Gamma)$.

To keep $\Delta D_{sp}(\Gamma)$ constant, Figure (A-3.a), the change is offset by applying a proportion of the unit load vector, $dP_1^{Iv} = df_1 \cdot P^{Iv}$, that produces a displacement at Γ, $dD_2^{Iv}(\Gamma)$, that is equal in magnitude but with an opposite sign to $dD_2^u(\Gamma)$ so that, $dD_2^{Iv}(\Gamma) = df_1 \cdot D^{Iv}(\Gamma) = -dD_2^u(\Gamma)$. This is shown as the dash-dotted line in the figure. The iterative load parameter, df_1, is calculated from this equation, $df_1 = -dD_2^u(\Gamma)/D^{Iv}(\Gamma)$.

The incremental displacement vector for the iteration is calculated, $dD_2 = dD_2^u + dD_2^{Iv}$. The values of displacements at other degrees of freedom are modified as shown in Figure (A-3.b).

4. The total increment load parameter, $\Delta f_2 = \Delta f_1 + df_1$, and the accumulated increment displacement vector through the second iteration, $\Delta D_2 = \Delta D_1 + dD_2$ are obtained. The structure resistance and unbalanced force vectors at the end of this iteration are evaluated as a function of ΔD_2, and check for convergence is performed.

The general steps of solution for iteration i may be summarized in the following steps,

1. The displacement vector due to the unbalanced forces at the beginning of the iteration, dP_{i-1}^u, is calculated, $dD_i^u = (K_{t,o}^j)^{-1} \cdot dP_{i-1}^u$.

The incremental load parameter for the iteration, df_{i-1}, that keeps the displacement at Γ constant is calculated, and the corresponding displacement due to load vector, dD_i^{lv}, and incremental displacement for the iteration, dD_i, are found,

$$\begin{aligned} df_{i-1} &= -dD_i^{u}(\Gamma) \,/\, D^{lv}(\Gamma), \\ dD_i^{lv} &= df_{i-1} \cdot D^{lv}, \\ dD_i &= dD_i^{u} + dD_i^{lv}. \end{aligned} \tag{A.6}$$

2. The total increment load parameter, Δf_i, the total applied force vector, ΔP_i, and total increment displacement, ΔD_i, for iteration i are calculated,

$$\begin{aligned} \Delta f_i &= \Delta f_{i-1} + df_{i-1}, \\ \Delta P_i &= \Delta P_{i-1} + df_{i-1} \cdot P^{lv}, \\ \Delta D_i &= \Delta D_{i-1} + dD_i. \end{aligned} \tag{A.7}$$

3. The structure resistance, $\Delta R_i = f(D_o, \Delta D_i)$, is calculated, and the unbalanced force vector is obtained, $dP_i^{u} = \Delta P_i - \Delta R_i$. Check for convergence is performed, and the process is repeated until convergence is obtained.

LIST OF REFERENCES

LIST OF REFERENCES

1. Argyris, J. H., B. Boni, U. Hindenlang, and M. Kleiber, "Finite Element Analysis of Two- and Three-Dimensional Elasto-Plastic Frames- The Natural Approach," Computer Methods in Applied Mechanics and Engineering, vol. 35, 1982, pp. 221-248.

2. Austin, Walter J. "In-Plane Bending and Buckling of Arches," Journal of Structural Division, ASCE, vol. 97, ST5, May 1971, pp.1575-1592.

3. Austin, Walter J. and Timothy J. Ross, "Elastic Buckling of arches under symmetrical Loading," Journal of the Structural Division, ASCE, ST5, May 1975, pp. 1085-1095.

4. Bathe, Klaus-Jurgen, and Arthur Cimento, "Some Practical Procedures for the Solution of Nonlinear Finite Element Equations," Computer Methods in Applied Mechanics and Engineering Journal, vol. 22, 1980, pp. 59-85.

5. Bathe, Klaus-Jurgen, "Finite Element Procedures in Engineering Analysis," Prentice-Hall Inc., 1982.

6. Batoz, Jean-Louis, and Gouri Dhatt, "Incremental Displacement Algorithms for Nonlinear Problems," International Journal of Numerical Methods in Engineering, vol. 14, 1979, pp. 1262-1266.

7. Bowles, Joseph E., "Structural Steel Design," McGraw-Hill, Inc., 1980.

8. Chen W. F., and T. Atsuta, "Theory of Beam-Columns," vol. I, McGraw-Hill, Inc., 1977.

9. Crisfield, M. A., "A Faster Modified Newton-Raphson Iteration," Computer Methods in Applied Mechanics and Engineering Journal, vol. 20, 1979, pp. 267-278.

10. Dusseau, Ralph, "Unequal Seismic Support Motions of Steel Deck Arch Bridges," volume II, thesis presented to Michigan State University, at East Lansing, Michigan, in partial fulfillment of the requirements for the degree of Doctor of Philosophy, 1985.

11. Dusseau, Ralph, and Robert Wen, "Seismic Responses of Deck-Type Arch Bridges," Journal of Earthquake Engineering and Structural Dynamics, vol. 18, 1989, pp. 701-715.

12. Harrison, Howard B., "In-Plane Stability of Parabolic Arches," Journal of the Structural Division, ASCE, vol. 108, ST1, January 1982, pp. 195-205.

13. Johnson, Lee W., and R. Dean Riess, "Numerical Analysis," 2nd. Edition, Addison-Wesley Publishing Co., 1982.

14. Komatsu, Sadao, and Tohru Shinke, "Practical Formula for In-Plane Load Carrying Capacity of Arches," Transactions, JSCE, vol. 9, 1977, pp. 92-95.

15. Komatsu, Sadao, and Tatsuro Sakimoto, "Ultimate Load Carrying Capacity of Steel Arches," Journal of the Structural Division, ASCE, vol. 103, No. ST12, December 1977, pp. 2323-2336.

16. Kuranishi, Shigeru, and Le-Wu Lu, "Load Carrying Capacity of Two Hinged Steel Arches," Proceedings of JSCE, No. 204, August 1972, pp. 129-140.

17. Kuranishi, Shigeru, "Allowable Stress for Two-Hinged Steel Arch," Proceedings of JSCE, No. 213, May 1973, pp. 71-75.

18. Kuranishi, Shigeru, "Load Carrying Capacity of Fixed Arches," Proceedings, International Colloquium on Stability of Structures under Static and Dynamic Load, Washington, D.C., March 17-19, 1977, pp. 609-617.

19. Kuranishi, Shigeru, and Tetsuya Yabuki, "Some Numerical Estimations of Ultimate In-Plane Strength of Two-Hinged Steel Arches," Proceedings of JSCE, No. 287, July 1979, pp. 155-158.

20. Kuranishi, Shigeru, Tsuneaki Sato, and Mitsugu Otsuki, "Load Carrying Capacity of Two-Hinged Steel Arch Bridges with Stiffening Deck," Proceedings of JSCE, No. 300, August 1980, pp. 121-130.

21. Kuranishi, Shigeru, and Tetsuya Yabuki, "Effect of Lateral Bracing Rigidities on the Ultimate Strength of Steel Arch Bridges," Proceedings of JSCE, No. 305, January 1981, pp. 47-58 (in Japanese, translated to English).

22. Kuranishi, Shigeru, and Tetsuya Yabuki, "Ultimate Strength Design Criteria for Two-Hinged Steel Arch Structures," Proceedings of JSCE Structural Engineering/Earthquake Engineering, vol. 1, No. 2, October 1984, pp. 225s-237s.

23. Kuranishi, Shigeru, and Tetsuya Yabuki, "Lateral Load Effect on Steel Arch Bridge Design'" Journal os Structural Engineering, ASCE, vol. 110, No. 9, September 1984, pp. 2263-2274.

24. Maeda, Yukio, and Masa Hayashi, "Nonlinear Analysis Method of Bridge Framed-Structures and Practical Calculation Method for Arches," Transactions, JSCE, vol. 12, 1980, pp. 330-338.

25. Medallah, Khaled, "Stability and Nonlinear Response of Deck-Type Arch Bridges," Thesis presented to Michigan State University, at East Lansing, Michigan, in partial fulfillment of the requirements for the degree of Doctor of Philosophy, 1984.

26. Ojalvo, I., and M. Newman, "Buckling of Naturally Curved and Twisted Beams," Journal of Engineering Mechanics Division, ASCE, vol. 94, No. EM5, October 1968, pp. 1067-1087.

27. Ojalvo, M., Edvin Demuts, and Frank Tokarz, "Out-of-Plane Buckling of Curved Members," Journal of Structural Division, ASCE, vol. 95, No. ST10, October 1969, pp. 2305-2316.

28. Orbison, James J., William McGuire, and John F. Abel, "Yield Surface Applications in Nonlinear Steel Frame Analysis," Computer Methods in Applied Mechanics and Engineering, vol. 33, 1982, pp. 557-573.

29. Owen, D., and E. Hinton, "Finite Elements in Plasticity," Pineridge Press Ltd., Swansea, U.K., 1980.

30. Porter, Frank L., and Graham H. Powell, "Static and Dynamic Analysis of Inelastic Frame Structures," Report No. EERC 71-3, Earthquake Engineering Research Center, University of California, Berkeley, California.

31. Sakimoto, Tatsuro, and Yoshio Namita, "Out-of-Plane Buckling of Solid Rib Arches Braced with Transverse Bars," Proceedings of JSCE, No. 121, July 1971.

32. Sakimoto, Tatsuro, and Sadao Komatsu, " Ultimate Strength of Steel Arches under Lateral Loads," Proceedings of JSCE, No. 292, December 1979, pp. 83-94.

33. Sakimoto, Tatsuro, and Sadao Komatsu, "Ultimate Strength of Arches with Bracing Systems," Journal of the Structural Division, ASCE, vol. 108, No. ST5, May 1982, pp. 1064-1076.

34. Sakimoto, Tatsuro, and Sadao Komatsu, "Ultimate Strength Formula for Steel Arches," Journal of Structural Engineering, ASCE, vol. 109, No. 3, March 1983, pp. 613-627.

35. Shinke, Tohru, Hiroshi Zui, and Yoshio Namita, "Analysis of In-Plane Elasto-Plastic Buckling and Load Carrying Capacity of Arches," Transactions of JSCE, vol. 7, 1975, pp. 62-65.

36. Shinke, Tohru, Hiroshi Zui, and Yoshio Namita, "Analysis and Experiments on In-Plane Load Carrying Capacity of Arches," Transactions of JSCE, vol. 9, 1977, pp. 49-52.

37. Shinke, Tohru, Hiroshi Zui, and Tomokazu Nakagawa, "In-Plane Load Carrying Capacity of Two-Hinged Arches with a Stiffening Girder," Transactions, JSCE, vol. 12, 1980, pp. 84-87.

38. Shukla, Shyam, and Morris Ojalvo, "Lateral Buckling of Parabolic Arches with Tilting Loads," Journal of the Structural Division, ASCE, vol. 97, No. ST6, June 1971, pp. 1763-1773.

39. Tokarz, Frank, "Experimental Study of Lateral Buckling of Arches," Journal of the Structural Division, ASCE, vol. 97, No. ST@, February 1971, pp. 545-559.

40. Tokarz, Frank, and Raghbir Sandhu, "Lateral-Torsional Buckling of Parabolic Arches," Journal of the Structural Division, ASCE, vol. 98, No. ST5, May 1972, pp. 1161-1179.

41. Wen, Robert K., and Fereydoon Farhoomand, "Dynamic Analysis of Inelastic Space Frames," Journal of the Engineering Mechanics Division, ASCE, vol. 96, No. EM5, October 1970, pp. 667-686.

42. Wen, Robert K., and Jalil Rahimzadeh, "Nonlinear Elastic Frame Analysis by Finite Element," Journal of Structural Engineering, ASCE, vol. 109, No. 8, August, 1983, pp. 1952-1971.

43. Wen, Robert K., Chung M. Lee, and Abdulaziz Alhamad, "Incremental Resistance and Deformations of Elasto-Plastic Beams," Journal of Structural Engineering, ASCE, vol. 115, No. 5, 1989, pp. 1267-1271.

44. Yabuki, Tetsuya, and Shigeru Kuranishi, "Out-of-Plane Behavior of Circular Arches under Side Loading," Proceedings of JSCE, No. 214, June 1973, pp. 71-82.

45. Yabuki, Tetsuya, Siramulu Vinnakota, and Shigeru Kuranishi, "Lateral Load Effect on Load Carrying Capacity of Steel Arch Bridge Structures," Journal of Structural Engineering, ASCE, vol. 109, No. 10, October 1983, pp. 2434-2449.

46. Yabuki, T., and S. Vinnakota, "Stability of Steel Arch Bridges, A State-of-the Art Report," Solid Mechanics Arch., vol. 9, Issue 2, Noordhoff International Publishers, Leyden, Netherlands, 1984.

47. Yabuki, Tetsuya, Siramulu Vinnakota, and shigeru Kuranishi, "Fixed-End Restraint Effect on Steel Arch Strength," Journal of Structural Engineering, ASCE, vol. 112, No. 4, April 1986, pp. 653-664.

48. Yabuki, Tetsuya, Le-Wu Lu, and shigeru Kuranishi, "An Ultimate Strength Design Aid for Fixed-End Steel Arches Under Vertical Loads," Proceedings of JSCE Structural Engineering/Earthquake Engineering, vol. 4, No. 1, April 1987, pp. 115s-123s.